University of Zurich[UZH]

Objective Classification of Extratropical Cyclones During Their Phase of Maximum Intensification

Luise Fischer
09-720-632
Department of Geography, 22 April 2016
GEO 511: Master Thesis

Supervision

Prof. Dr. Heini Wernli
Dr. Michael Sprenger
Dominik Büeler
Institute of Atmospheric and Climate Science
Universitätstrasse 16, 8092 Zürich
heini.wernli@envz.ethz.ch

Responsible Faculty Member

Prof. Dr. Jan Seibert

Abstract

Despite the fact that extratropical cyclones are driving factors of the weather in the extra tropics, our understanding of their great variability is limited, and attempts made to abstract and categorize extratropical cyclones have so far been largely based on subjective methods. The objective classification method applied and analyzed in this thesis, extends the understanding of extratropical cyclones by offering an insight into different atmospheric flow conditions during the phase of maximum intensification. A principal component analysis and subsequent rotation is applied in a phase space spanned by 29 potentially relevant parameters determined in the vicinity of cyclone events from ERAinterim Re-Analysis data in the winter months from 2000-2011, in order to classify the events. Variability in mid- and low-level baroclinicity as well as upper-level forcing and tropospheric stability emerge as the key elements for the objective classification resulting in 5 cyclone classes. These 5 classes differ strongly in terms of the physical conditions in the troposphere during the cyclone's maximum intensification. The objective classification highlights the relevance of key elements of the atmospheric flow conditions during intensification and largely improves the comparability across case studies.

Contents

Chapter 1

Introduction

1.1 Motivation

Extratropical Cyclones (ETCs), also referred to as mid-latitude cyclones, have a great influence on the weather. Therefore studying ETCs is a core topic in atmospheric science. ETCs show great variability in genesis region, intensification, lifetime, and track. This variability poses a challenge for predictions of day-to-day and extreme weather events, motivating the need for objective classification methods of ETCs.

The intensity of an ETC is determined by its core pressure and the rate at which this core pressure decreases over time. Not all ETCs reach the same intensity, this leads to varying effects on the environment. All ETCs intensify during their life cycle (cf. Sec: 1.2.1), some intensify much stronger and faster than others. Sanders and Gyakum (1980), developed an arbitrary definition which labels ETCs with a core pressure drop of more than 24 hPa in 24 hours as *explosively intensifying*[1]. ETCs experiencing explosive intensification are also referred to as bombs. Note that most ETCs do not undergo explosive intensification, those ETCs which do however, result in extreme events. Preferred areas for explosive intensification show a combination of a baroclinic process with one or more other mechanism(s) (Roebber, 1984). The distance ETCs travel varies greatly with some cases recording a distance of greater than 6000 km (Gulev et al., 2001). Statistical analyses show that ETCs, occurring for example in the Northern Hemisphere, can have a life time of $1 - 10^{+}$ days where 50% of them exist for $1 - 4$ days, as shown by Gulev et al. (2001) in their study of ETCs occurring in the Northern Hemisphere.

Those ETCs, which undergo explosive intensification are responsible for extreme weather events, sometimes leading to low temperatures, damaging levels of wind, precipitation (rain and snow), as well as coastal and inland flooding (some of which are described in the case studies in Chap: 3). Future changes in climate conditions will have a significant impact on the frequency of explosively developing ETCs (Pfahl et al., 2015). A better understanding of the large case-to-case variability in ETC intensification is therefore of great importance for future climate with warmer temperatures.

A number of different physical and dynamic processes influencing the ETCs during their lifecycle are responsible for the diversity in their evolution. Classification is a common tool applied to obtain a better understanding of complex systems with a large number of degrees of freedom. Abstracting the characteristics of complex systems through classification, allows a systematic categorization into distinct classes. Classification schemes have been developed to improve the conceptual understanding of the genesis and development of ETCs as well as the variability therein. These methods are largely based on subjective analysis of a limited number of case studies (cf. Petterssen and Smebye (1971), Shapiro and Keyser (1990), and Devenson et al. (2002)), greatly limiting their applicability.

[1] For further detail see Sec: 4.2.3 and Sanders and Gyakum (1980)

1.2 Background Information

This section provides insight into the definition of ETCs, and the physical conditions of the atmosphere which can lead to their intensification. The section further summarizes subjective classification methods which are widely used to characterize cyclones.

1.2.1 Extratropical Cyclones

ETCs generally occur between 30-60°north (south) on synoptic scales and are characterized by a low pressure system at their centre. They are located by the point of lowest pressure at sea level, which identifies the centre of the cyclone. The pressure at the centre of the cyclone is termed the *Cyclone Core Pressure* (CCP). The point at which an ETCs originates is called its genesis. The CCP of an ETC typically decreases over time (intensification phase) until it reaches its minimum value, after which the CCP increases again (cf. Fig:1.1a). An ETC decays when its CCP has risen back to similar levels as the surrounding environment. Tracing the geographical location while an ETC moves across the earth's surface allows to depict its track. Figure 1.1b shows a hypothetical ETC track, with the point of genesis and decay labelled. Intensification occurs when the CCP decreases. The *phase of maximum intensification* is taken to be the 24 hour period with largest decrease in CCP, normalized to the latitude at which the core of the ETC is located. This phase of maximum intensification is also marked in red in Fig: 1.1a and b.

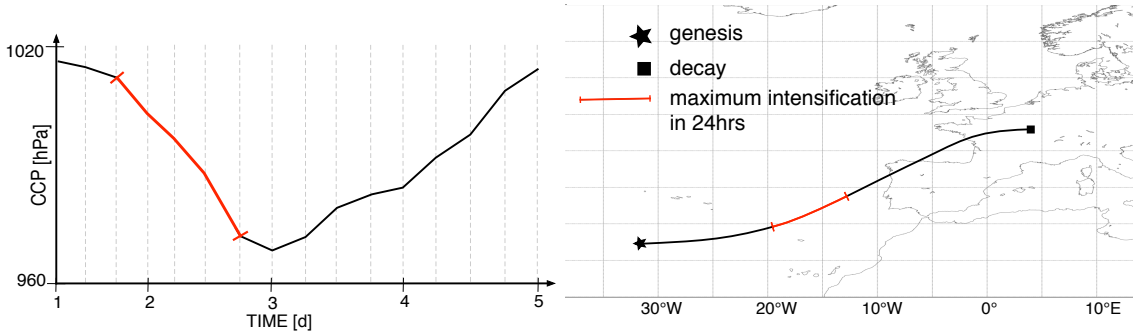

(a) (b)

Figure 1.1: Sketch of hypothetical cyclone track (right) and corresponding CCP (left).

1.2.2 Established classification methods

Two fundamentally different methods have become most prevalent for the classification of cyclones on synoptic scales. One method is based on how the structure and fronts develop during the cyclone's life cycle, this is applied in the Norwegian, and the Shapiro-Keyser cyclone models. The other method, applied in the Petterssen and Smebye model, uses a number of physical factors during the genesis and the intensification phase to distinguish different types of cyclones.
The Norwegian cyclone model suggests that cyclogenesis is induced by instability along the polar-front (studied in Bjerknes and Solberg (1922), Schultz et al. (1998), and Baehr et al. (1999)). In this context the polar-front is seen as a semipermanent discontinuity which creates a border between the cold dry polar air masses and the warm moist subtropic air masses. The initial disturbance at the polar-front leads to cyclonic circulation. The genesis of a cyclone is followed by southward advection of cold polar air masses to the west and northward advection of warm subtropical air masses to the east of the centre of the cyclone (in the Northern Hemisphere). This leads to the development of a warm- and a cold-front. The cold-front moves faster than the warm-front, hence the fronts close to the centre start occluding as the cyclone matures. The fronts occlude further leading to weakening and eventual decay of the cyclone.

Shapiro and Keyser (1990) developed a similar conceptual idea where the genesis is also based on a slightly deformed baroclinic zone. The perturbation is intensified by the deformation field as fronts develop. Different to the polar-front cyclone the warm and cold fronts move at the same pace staying orthogonal to each other until the cold-front weakens and the warm-front curls in around the cyclone centre.
Literature indicates that large-scale flow has an important effect on the development of midlatitude cyclones. Schultz et al. (1998) show that the different spacial extent and evolution of the frontal systems of the two models can be attributed to large-scale diffluence and confluence at upper-levels. In this context cyclones resembling the Norwegian model frequently develop in diffluent background flow which leads to the meridional elongation of the fronts. High-amplitude background diffluence occurs at the end of storm tracks (e.g. above the north east Atlantic in the vicinity of Norway). Lage-scale confluent flow on the other hand typically occurs at the start of storm tracks, such as off the east coast of the north american continent. This kind of large scale flow regime leads to cyclone development as the Shapiro and Keyser model describes it (Schultz et al., 1998).
The cyclone model by Petterssen and Smebye (1971) is made up of two classes (A and B). It was later supplemented with a third class (C) by Devenson et al. (2002) using quasi-geostrophic omega equation diagnostics. Type-A cyclones develop as frontal waves below strong zonal upper-level flow. Temperature advection and strong baroclinicity dominate at the start. Vorticity advection and also potential vorticity (PV)[2] in the mid- and upper-troposphere only play a minor role during the life cycle. The distance between the developing upper-level trough and the cyclone stays relatively constant during the intensification while the baroclinicity decreases. Type-B cyclones develop when an upper-level trough passes over a region with increased warm air advection. Positive PV anomalies in the mid-troposphere are important for their genesis. The baroclinicity increases throughout the intensification while the distance between the upper-level trough and the cyclone decreases over time. According to Petterssen and Smebye (1971) Type-A cyclones occur above the ocean while type-B cyclones occur above land. Later studies, however, show a less specific geographical location for those two types (Schultz et al., 1998). Type-C cyclones are strongly influenced by lower-level diabatic heating. Similar to type-B this type is also greatly driven by upper-level forcing and is associated with less strong baroclinicity. Different to type-B this type of cyclone is not based on an interaction between an upper-level trough and a lower-level baroclinic zone.

1.2.3 Dynamics of intensification

Based on the short summary of established classification methods it is apparent that there are different drivers of cyclogenesis and intensification. Baroclinic instability is essential, hence with stronger baroclinicity the potential for cyclone intensification increases. A baroclinic zone does not automatically lead to baroclinic instability. A trigger is needed to induce baroclinic instability in a baroclinic zone. Hence, not every baroclinic zone is related to cyclone development and intensification. A common trigger for baroclinc instability is the interaction of an upper-level trough, also referred to as an upper-level PV anomaly, with a low-level baroclinic zone (cf. Typ-B cyclone). In addition, diabatic processes in the lower- and mid-troposphere can also lead to cyclone intensification. Diabatic processes lead to the production of positive PV anomalies, which in turn induce a cyclonic wind field (cf. appendix Sec: A).
A baroclinic zone describes a region of strong pressure and temperature gradient in the atmosphere. These zones occur in the extra tropics along the area where polar and subtropic air masses come into contact. Instability means that small-scale perturbations could spontaneously amplify. The difference in pressure and temperature offers potential energy. Hence the source of energy for the growth of disturbances along these zones is derived from the basic-state potential energy in the baroclinic environment.
Baroclinic zones and related baroclinic instability also influence upper-level flow, which is defining for jet velocities (and jet streaks) close to the tropopause. Strong baroclinicity along zones with no curvature lead to high jet velocities. The right (left) entrance and left (right) exit region of a

[2]for details on the concept of potential vorticity please see Sec: A in the appendix

jet velocity maximum, also called jet streak, lead to divergence in the upper-levels and therefore to upward movement of the air which induces/intensifies a cyclonic wind field, in the northern (southern) hemisphere. The vertical air movement in context of cyclone's the position related to the jet core can be explained by the quasi-geostrophic omega equation from Trenberth (1978) (Baehr et al. (1999) and Devenson et al. (2002)).
Upper-level troughs of high PV also lead to divergence in the upper-levels, related updraft, and hence the development/reinforcing of a cyclonic wind field. A trough is an elongated area of relatively dry and cold polar air expanding south (north) into lower latitudes, the updraft is commonly observed in the area of warmer air on the east (west) of a trough in the northern (southern) hemisphere. Troughs occur regularly in the westerly flow in the mid-latitudes.
Latent heat release is a result of condensation, regularly occurring in warm rising air masses. Latent heating leads to production of positive PV below and negative PV above (Danard (1963), Dixon et al. (2003), and Ahmadi-Givi et al. (2004)). As a result the PV above is eroded/decreased and anticyclonic movement is induced. On the contrary, conditions below the latent heating maximum evoke or intensify a cyclonic wind field.

1.3 Aim

The importance of different drivers for cyclone intensification vary greatly from one ETC to another. For example, the interaction of an upper-level trough with low-level baroclinicity plays a large role for some ETCs and is non-existent for others. Quantifying this variability can therefore expand the current understanding of ETCs. Identification of physical parameters which play a particularly large role in explaining the observed variability in cyclone intensification is highly intriguing.
The goal of this thesis is to implement and analyze an objective classification method of ETCs at a specific time point during their life-cycle, namely the point during which the cyclones underwent their maximum intensification. Twenty-nine different physical parameters are calculated aiming to represent different drivers for intensification. A statistical investigation of the 29 physical parameters is conducted to determine which of them play a particularly large role in explaining the observed variability. The newly gained knowledge then serves as a basis for an objective classification of ETCs into different classes.
The method applied for the statistical analysis is closely related to a PhD thesis conducted at the Institute of Atmospheric and Climate Science at ETH. In his work Graf (2014), focused on developing a method to allow an objective classification of cyclones at the time point of their genesis.
Research Questions:
The research questions addressed in this thesis are:
1) Is it possible to distinguish classes during the phase of maximum intensification, when applying the same methods as used for the objective classification of cyclogenesis Graf (2014)?
2) Which parameters are particularly important and therefore have a greater impact on the classification?
3) What are the climatological characteristics of the different classes?
4) Do classes differ with respect to the number of cyclone events with strong/weak intensification?
Hypotheses:
Based on prior research and the analysis conducted in this thesis, the following possible outcomes are hypothesized:
H1 - On Parameters: parameters used for the objective classification are relevant for the largest deepening phase.
H2 - On Classes: it is possible to distinguish an appropriate number of classes in the parameter space, which are reasonable from a physical point of view and significantly different.
H3 - On Intensification: cyclones of the same class intensify based on a similar combination of parameters, but show varying amplitudes of intensification.

Chapter 2

Data & Methods

This chapter aims to give an overview over the key elements of the objective classification method, which is applied and analyzed in this master thesis. First of all, it outlines what kind of data is used to calculate 29 different physical parameters, which serve as a basis for the classification. The characteristics of the different physical parameters are described in the second section. The third section gives an insight into the physical parameter values, i.e. how they are normalized and how one single value for each parameter and cyclone intensification event is determined. The last two sections offer a detailed description of how statistical methods and visualization tools are used to reduce the dimensionality of the data set and to determine a categorization.

2.1 Data

In this project cyclone events are identified with the method described in Wernli and Schwierz (2006). The method uses sea level pressure (SLP) of the Re-Analysis data from the European Centre for Medium-Range Weather Forecasts (ECMWF). Isobars at 0.5 hPa intervals are drawn and local SLP minima are detected on a 1° x 1° latitude/longitutde grid and analyzed further if surrounded by at least one closed isobar. The identified cyclone events are subsequently tracked by applying a tracking-algorithm, based on the positions of the cyclone centers, as described in Wernli and Schwierz (2006). The data set used for analysis is ERAinterim Re-Analysis data, reduced to all cyclone events which occurred in the extra-tropics of the Northern Hemisphere, in the winter months (DJF) over the time period from 2000-2011.
The identification, tracking, and the further selection of the winter months results in a list of 8455 cyclones. The exact geographical location and the corresponding SLP of each cyclone is known at 6 hour intervals along the track. As explained in the introduction, the phase of maximum intensification is the 24 hour period with largest decrease in CCP. To identify the phase of maximum intensification, the CCPs at each 6 hour time point are first normalized to the latitude, i.e., the cyclone's location. The pressure drop is calculated as the difference between the CCP at the start and at the end of each 24 hour section along the track. The phase of maximum intensification thus spans over the 5 time points where this difference in CCP is the maximum. For the classification the mid time point of these 24 hours is used to represent this phase, and will hereafter be referred to as PMI (Point Maximum Intensification).

2.2 Physical Parameters

The objective classification is based on 29 different parameters[1], all of which are summarized in Tab: 2.1. The description of the parameters in this section is according to the work done in the PhD project of Graf (Graf, 2014). For more details on the different parameters see Graf et al. (2016) and Graf (2014).

[1] *precursors* in Graf (2014) and Graf et al. (2016) are here referred to as parameters

The physical parameters can be summarized into seven subgroups concerning the atmospheric conditions in the vicinity of the cyclone at the time point of interest (PMI).

2.2.1 Upper-level flow

The upper-level potential vorticity (PV) PV_{up} is calculated as a pressure-weighted average over all model levels between 600 and 200 hPa. The pressure difference between two levels is multiplied with the PV on the pressure levels, these values are then summed up and divided by the total pressure difference. This parameter indicates if increased values of PV occurred during the intensification. The geopotential height at 500 hPa (Z_{500}) is used to see if an upper-level trough or ridge is present or not; correspondingly the anomaly of the geopotential height relative to a 48-hour running mean (Z_{ANOM}) indicates the influence of short wave troughs. Another parameter aiming to represent the characteristics of the upper-level flow during the intensification is $VELJET$, the wind speed at jet stream level. It is calculated as the vertical mean horizontal wind speed between 500 and 100 hPa.

2.2.2 Vertical motion

The six parameters describing the vertical motion are determined with two complementary methods. Parameters $qg\omega_{bot}$ and $qg\omega_{top}$ are based on the quasi-geostrophic omega equation.

$$\delta_x^2(\sigma\omega) + \delta_y^2(\sigma\omega) + f^2\delta_p^2\omega = -2\nabla_h^2\boldsymbol{Q}, \tag{2.1}$$

where x, y describe the horizontal cartesian coordinates, p the pressure, σ the static stability, f the coriolis parameter, ω the quasi-geostrophic vertical wind, and the Q-Vector ($\boldsymbol{Q}$), which is described e.g. in Holton (1979). The equation is used here to calculate the quasi-geostrophic vertical motion at the 600 hPa pressure level. It is split into low-level forcing from below 650 hPa ($qg\omega_{bot}$), and upper-level forcing from above 500 hPa ($qg\omega_{top}$). The second approach uses the Lagrangian perspective to analyze the vertical motion of the air parcels prior to the PMI. 2-day backward trajectories are started at 850 hPa at the position where the cyclone is located at PMI. The pressure and potential temperature (θ) difference is calculated over 48 hours ($TRAdP_{48}$ and $TRAd\theta_{48}$). These two parameters complement the Eulerian perspective of the quasi-geostrophic forcing with the Lagrangian perspective, as they consider a longer time frame and include the change of θ to determine if diabatic processes are relevant for the vertical motion. To include short-term changes in pressure and potential temperature, the maximum change in 6 hours within the 48h-period is additionally determined ($TRAdP_{MX}$ and $TRAd\theta_{MX}$).

2.2.3 Thermodynamic stability

The static stability of the troposphere is determined by the Brunt-Väisälä frequency $N^2 = \frac{g}{\theta}\frac{\partial\theta}{\partial z}$ where g is the gravity and θ the potential temperature. A vertical average of N^2 is calculated between the surface and the 2-PVU-tropopause height to represent the coupling of upper-level structures and the lower-tropospheric flow (N^2_{TROPO}). Note, using an average to calculate this parameter, does not allow an appropriate representation of wether or not inversions are present. Parameter $\Delta\theta_{SKT700}$ further characterizes the stability of the troposphere. It is calculated as the difference of θ between the surface and the 700 hPa level. This parameter aims to capture the lower tropospheric stability, in particular cold air outbreaks and polar lows (Bracegirdle and Kolstad, 2010). It is only calculated for areas where the surface is below 850 hPa to exclude orographic bias, regions with higher elevation could otherwise be misinterpreted. As a third parameter the mixed-layer $CAPE$ is used to determine the convective potential of the air column in the cyclone centre at PMI. It is defined as:

$$CAPE = \int_{LFC}^{EL} g\left(\frac{T_{parcel} - T_{env}}{T_{env}}\right)dz, \tag{2.2}$$

here, T_{parcel} is the initial temperature of a rising air parcel calculated as the average over the lowest 50 hPa above the surface and T_{env} is the temperature of the environment. LFC stands for the level of free convection at which an air parcel rises moist-adiabatically and EL describes the equilibrium level at which the lifted air parcel's buoyancy becomes negative.

2.2.4 Baroclinicity

The Eady growth rate is commonly used to describe baroclinic instability (Eady, 1949). It is a combination of the vertical stability N and the vertical gradient of the horizontal wind $\boldsymbol{v} = (u, v)$:

$$EADY = 0.31 \cdot \frac{f}{N} \cdot \left| \frac{\partial \boldsymbol{v}}{\partial z} \right| \tag{2.3}$$

The inclusion of the Coriolis parameter f indicates that the theory is only valid in the extra tropics. The Eady growth rate for the lower ($EADY$) and the upper troposphere ($EADY_{up}$) are each determined. The former one is calculated as follows:

$$EADY = 0.31 \cdot \frac{f}{N_{500-850}} \cdot \left[\left(\frac{u_{500} - u_{850}}{Z_{500} - Z_{850}} \right)^2 + \left(\frac{v_{500} - v_{850}}{Z_{500} - Z_{850}} \right)^2 \right]^{1/2} \tag{2.4}$$

Here $N_{500-850}$ is a pressure weighted average of the Brunt-Väisälä frequency N^2 between 500-850 hPa. For the upper troposphere the Eady growth rate is calculated analogously between 300-500 hPa.

2.2.5 Fronts

Fronts enhance the horizontal temperature gradients and thus baroclinicity. Enhanced deformation close to developing fronts can also hinder cyclonic movement (Bishop and Thrope, 1994). Four different parameters aim to represent fronts. Two of them being the equivalent potential temperature at 850 hPa (θ_{e850})[2] and its horizontal gradient ($|\Delta\theta_{e850}|$) which displays the fronts more clearly than $|\theta_{850}|$[3] alone, as it also respects the specific humidity. Environmental deformation can also lead to the development of fronts. The deformation at 850 hPa is therefore represented by DEF. It is calculated from the average wind field ($\bar{u}_{12h}, \bar{v}_{12h}$) as follows:

$$DEF = \sqrt{\left(\frac{\partial \bar{v}_{12h}}{\partial x} \frac{\partial \bar{u}_{12h}}{\partial y} \right)^2 + \left(\frac{\partial \bar{u}_{12h}}{\partial x} \frac{\partial \bar{v}_{12h}}{\partial y} \right)^2} \tag{2.5}$$

Another parameter which is used to represent fronts is $FGEN_{850}$. It is based on Petterssen's frontogenesis function at 850 hPa (Petterssen, 1936) and aims to capture the change of horizontal temperature gradient using the Lagrangian perspective.

2.2.6 Moist dynamics

Four different parameters are included to represent the moist dynamics occurring in the vicinity of the cyclone centre at PMI, the most obvious one being precipitation (RR_{6h}). RR_{6h} is the precipitation which fell at the surface accumulated over the 6 hours prior to the time point of interest (PMI). The integrated water vapor (Q_{int}) is calculated as the vertical integral of specific humidity over the atmospheric column. The low-level PV (PV_{low}) is also categorized into the

[2] θ_e is the temperature an air parcel would have if all of the contained water vapor was condensated at constant pressure and the released latent heat was added to the parcel (diabatic process) which was finally brought to 1000 hPa

[3] Note, the subtropic and polar air masses which interact in the extra-tropics, differ in temperature and moisture, θ however only respects adiabatic (dry) processes, whereas θ_e includes the specific humidity.

topic of moist dynamics as it is often generated diabatically by latent heat release. PV_{low} is calculated as the pressure weighted average of PV between 1000-600 hPa. The time period since the moisture uptake ($UPTTIM$) further complements the parameters already mentioned. Using the Lagrangian perspective it is calculated with 5-day backward trajectories: if the trajectory is within the atmospheric boundary, moisture uptake is assumed.

2.2.7 Surface fluxes and temperature

The sensible and latent heat fluxes are the result of temperature and moisture differences between the surface and the atmosphere. They are governed by diffusion, and turbulence at the surface. The 6-hourly accumulated sensible ($SSHF$) and latent ($SLHF$) heat fluxes capture the thermodynamic preconditioning of the troposphere. Negative fluxes indicate fluxes from the surface to the troposphere. To represent the temperature at the surface the parameters SKT and T_{PERT} are used. The former is the skin temperature and the latter is calculated at higher levels (850 hPa). To complement the baroclinicity and frontogenesis, T_{PERT} comprises the temperature anomalies at 850 hPa. This parameter aims to capture positive (negative) temperature anomalies which can also induce cyclonic (anticyclonic) circulations. In addition, the horizontal temperature advection at 850 hPa is calculated with $\bar{u} \cdot \nabla_H T$, $\bar{u}$ being the horizontal wind vector and $\nabla_H T$ the horizontal temperature gradient. It is represented by the parameter T_{ADV850}.

2.3 Parameter value extraction

The values of the different physical parameters are each calculated at every grid point, globally. Performing a comparison of $>$ 8000 cases requires the field of each physical parameter, a) to be normalized and b) to be represented by one single value for each case.
Normalizing the parameter values of each case is based on the calculation of the deviation of the parameter value from the climatology at every grid point:

$$\frac{A - A_{\text{clim}}}{\text{stdv}[A_i]} = \text{normalized parameter value}\, A_{norm}\,,$$

where A represents any one of the parameters, $A_{clim} = mean[A_i]$ is the climatological mean of the given parameter and i the amount of days used to calculate the mean. The climatological mean is calculated based on a 30-day running mean at every grid point for every individual cyclone intensification case (at the time point of interest). The term stdv$[A_i]$ computes the standard deviation of the physical parameter value over the given 30-day period, at every grid point. A_{norm} are therefore standard deviations from the climatological mean. The result of this normalization are non-dimensional parameter values at each grid point, on a global scale.
The normalization leads to a more clearly defined signal of the parameter fields (cf. Fig: 2.1). To facilitate the analysis of individual cases, the meteorological field is centered around the core of the cyclone at PMI and rotated onto the equator to eliminate distortion due to the varying geographic location of the events. Subsequently the cyclone domain of +-20° in zonal and meridional direction is cut out (approx. 4000 km total side length). Based on this choice of domain of interest, an example of the change in values from the physical parameters to the values of the normalized parameters is displayed in Figure 2.1.
Once a normalized value is calculated for each grid point in the cyclone domain, a single value is extracted for each parameter for every event. Consider the parameter PV_{up} for the case Martin (1999) as an example, the core of the cyclone is exactly in the centre, marked with the grey cross (cf. Fig: 2.1). It is visible that the value of PV_{up} is low at the centre, to the north-west however, a positive anomaly of this parameter can be detected. Using the value at the centre can hence lead to a misrepresentation of the parameter. As a result an area with a radius of 500km from the centre of the field is used to calculate a single value for each parameter. The area is marked as the grey dashed circle in the diagrams of the cyclone domain and is referred to as the CIR (Cyclone Intensification Region) from here onwards.

The single value for each parameter is either calculated as the average above or below the median of the normalized parameter values in the CIR. This technique is applied in order to represent dipolar characteristic of parameters. At the same time it allows parameters with more gradual characteristics within the CIR to be represented, evoking a slight overestimation of their influence on the cyclone intensification. For some parameters an average over the whole area (of the CIR) would result in a reasonable representation, e.g. for the equivalent potential temperature at 850hPa (θ_{e850}), for others, however, this would lead to a smoothing and hence misrepresentation.

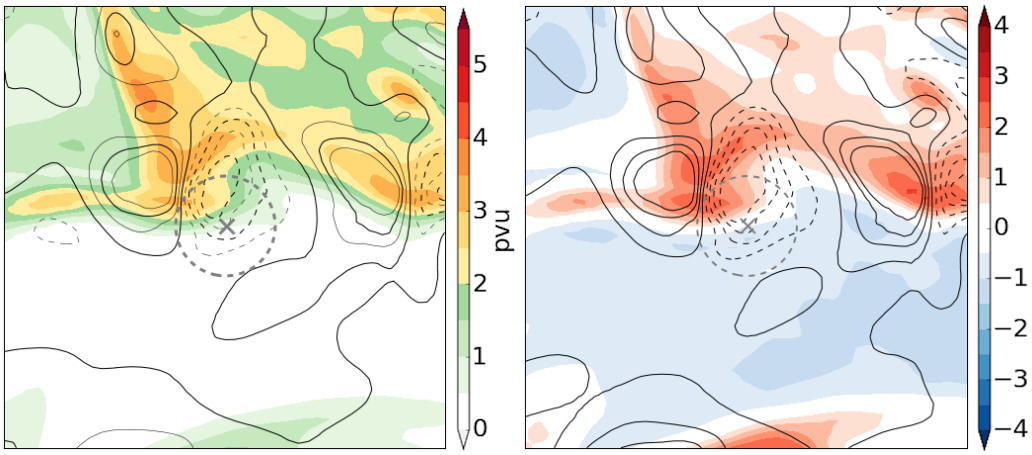

Figure 2.1: PV_{up} and $qg\omega_{top}$ values before (A) and after normalization (A_{norm}) of winter storm Martin (1999): PVU (filled contours) and $qg\omega_{top}$ (black contours) in steps of $2 \cdot 10^{-2}$ Pas^{-1}, full lines mark descent, dashed lines mark ascent. The A values are displayed in the plot on the left, while the plot on the right shows the deviations of the physical values from the climatology A_{norm}. The grey cross marks the position of the centre of the cyclone. The grey dashed line encompasses the CIR (cyclone intensification region) with the cyclone centre at its centre and a radius of 500km.

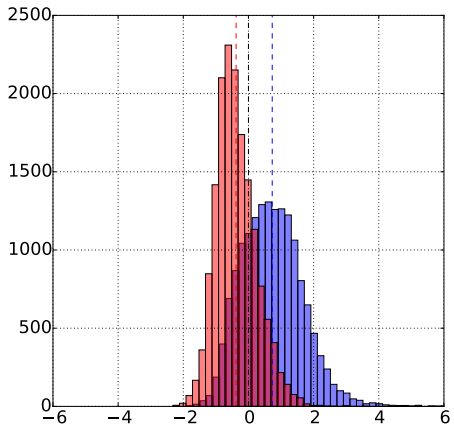

Figure 2.2: Frequency of parameter PV_{up} averaged above (blue) and below (red) the median. Horizontal axis shows the single parameter values, i.e. the average standard deviation from the climatology (0-anomaly) within the CIR, calculated above or below the median, for every case. The vertical axis shows the number of cases with the corresponding parameter value.

The slight bias towards an overestimation of the influence of the parameters on cyclone intensification is visualized by the difference in distributions based on the choice of average displayed in Fig: 2.2. The two distributions in Fig: 2.2 each show the distribution of the extracted parameter values versus the deviation from the climatology of the parameter PV_{up}. The blue bars show the distribution of all the cases if their parameter value is computed as the average above the median and the red bars show the distribution of all cases if their parameter value is computed as the average below the median. The dashed red and blue lines mark the corresponding mean value over all cases. The black dashed line represents the 0-anomaly.
In order to handle the parameters as similar as possible during the parameter value extraction, the majority of the parameters are calculated as the average above the median of the values of all grid points within the CIR. This leads slightly higher values and as mentioned above, to a corresponding overestimation of the importance of the parameter values for cyclone intensification. For some parameters low values indicate a positive forcing for cyclone intensification. Therefore the case-representing-value of these physical parameters is calculated as the average below the median in the CIR. Negative values of the $qg\omega top$ or $qg\omega bot$ forcing for example, indicate rising air masses, i.e. divergence and a decrease in pressure, hence intensification of a cyclone. All parameters and the corresponding abbreviation and signal are listed in Tab: 2.1 for further reference.
In summary, 29 physical parameters have been calculated for each of the 8455 cyclone intensification events in the Northern Hemisphere in the winter months (DJF). The physical parameters are normalized relative to the climatology and chosen to capture dipole as well as monopole structures of the physical parameters within the CIR. If one of the physical parameter values cannot be calculated for a case, the mean is calculated from the parameter value of the other cases to replace it (happens in around 500 cases).

Table 2.1: List of parameters with abbreviation and associated sign. The (+/-) sign means that the average is calculated above/below the median. source: Graf et al. (2016)

Short description of parameter	**Abbrev.**	**Sign**
Upper-level PV (averaged between 600 and 200 hPa)	PV_{up}	+
Geopotential height at 500 hPa	Z_{500}	−
Anom. of geopot. height at 500 hPa (relative to the 2 day running mean)	Z_{ANOM}	−
Wind speed at jetstream level (averaged between 500 and 100 hPa)	$VELJET$	+
Low-level contribution to quasi-geostrophic vertial motion	$qg\omega_{bot}$	−
Upper-level contribution to quasi-geostrophic vertical motion	$qg\omega_{top}$	−
Pressure difference in 48 h backward trajectories	$TRAdP_{48}$	−
Maximum pressure difference in 48 h backward trajectories	$TRAdP_{MX}$	−
Difference of pot. temperature in 48 h backward trajectories	$TRAd\theta_{48}$	+
Maximum change of pot. temperature in 48 h backward trajectories	$TRAd\theta_{MX}$	+
Tropospheric static stability	N^2_{TROPO}	−
Difference of pot. temperature between surface and 700 hPa	$\Delta\theta_{SKT700}$	−
Mixed-layer CAPE	$CAPE$	−
Eady growth rate in the lower troposphere	$EADY$	+
Eady growth rate in the upper troposphere	$EADY_{up}$	+
Equivalent-pot. temperature at 850 hPa	θ_{e850}	+
Horizontal temperature gradient at 850 hPa	$\lvert\Delta\theta_{850}\rvert$	+
Horizontal gradient of equivalent-pot. temperature at 850 hPa	$\lvert\Delta\theta_{e850}\rvert$	+
Environmental deformation at 850 hPa	DEF	+
Petterssen frontogenesis function at 850 hPa	$FGEN_{850}$	+
Surface precipitation in 6 h	RR_{6h}	+
Vertical integrated water vapor	Q_{int}	+
Low-level PV (averaged between 1000 and 600 hPa)	PV_{low}	+
Time period since moisture uptake	$UPTTIM$	+
Horizontal temperature advection at 850 hPa	T_{ADV850}	+
Sensible heat flux at the surface	$SSHF$	+
Latent heat flux at the surface	$SLHF$	+
Skin temperature	SKT	+
Anomaly of the 850 hPa temperature (relative to the 10 day running mean)	T_{PERT}	+

2.4 Principal Component Analysis

The objective classification of the cyclone events during their PMI is based on a principal component analysis (PCA) (cf. Pearson (1901) and Hotelling (1933)). This is a method of multivariate statistics based on the variance within a data set. A PCA can be understood as the orthogonal projection of the data onto a lower dimensional space (Hotelling, 1933). This section first describes the theory of performing a PCA and then explains how a PCA serves to reduce the dimensions of a data set with a large number of correlated variables (here physical parameters).
Note that all parameters are weighted equally in the objective classification independent of the strength of evidence for their contribution to the intensification of cyclones. The parameters were chosen for the objective classification of cyclones at the point of genesis (Graf, 2014). It is therefore possible that some of them are of less importance during the phase of maximum intensification. Some parameters result in similar forcings and describe interconnected physical processes. Statistical correlations between the different parameters, show no significant redundancy in the parameters chosen for the classification (cf. Sec: 4.1.2).
The cyclone intensification events are a cloud of points in a 29-dimensional parameter space with the different physical parameters corresponding to the 29 coordinate axes. This is called the *physical parameter space*. The PCA redefines the coordinate axes such that the greatest variance within

the cloud of points occurs along the first axis pc1 (first principal component). Each succeeding axis (pc2-pc29) is oriented such that the greatest possible variance occurs along it with the constraint that it is orthogonal to all previous principal components. The resulting vectors are uncorrelated principal components, with the first one explaining the greatest variance and all succeeding principal components explaining decreasing amounts of variance in the data set (Hotelling, 1933). The first few pc's capture a large amount of the variance within the data set. For visual clarification see Fig: 2.3.
The principal components are a linear combination of the different physical parameters. Each principal component is thus a 29 dimensional vector in the physical parameter space where the i^{th} element of the vector is called the *coefficient* for the i^{th} physical parameter. The coefficients describe how much each parameter contributes to the principal component. The space defined by vectors pc1-pc29 is called the *principal component space*.

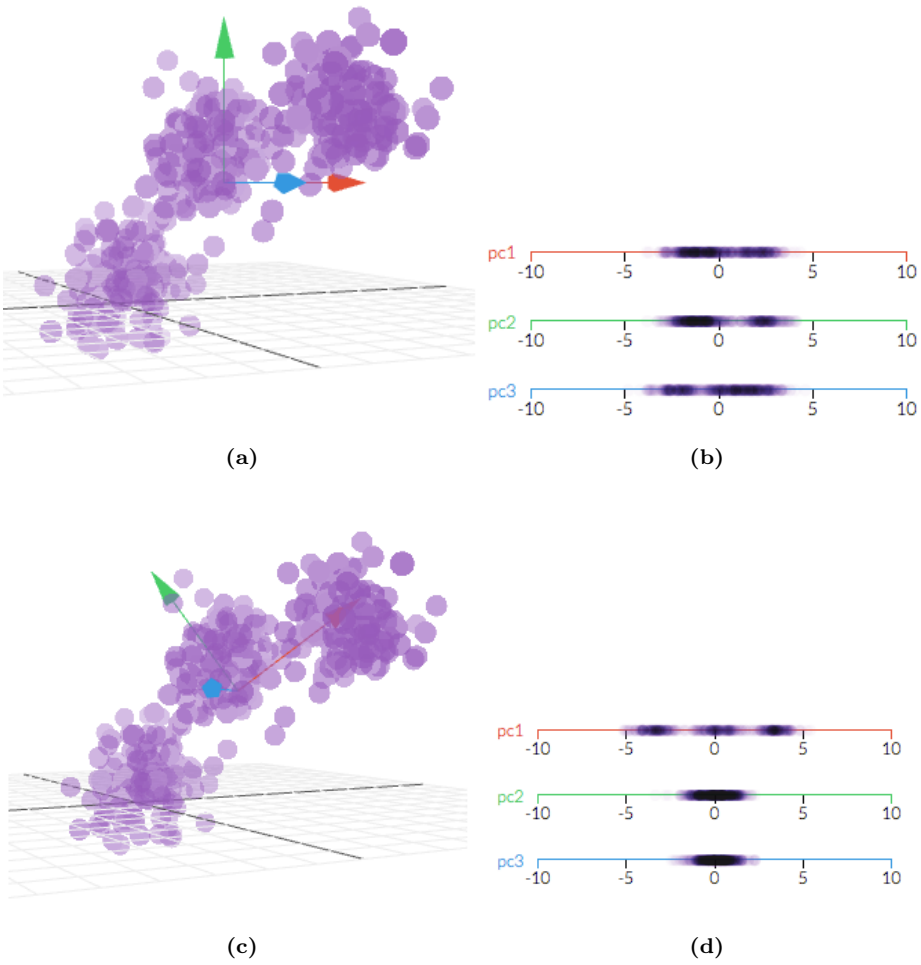

Figure 2.3: Example clound of points in 3D with projection axes: a) red, green, and blue axes are laid into the space at random in orthogonal directions **b)** variance within the cloud of points along the axis directions corresponding to plot a) **c)** red blue and green axes are laid into the space based on a PCA with red = pc1, green = pc2, blue = pc3 **d)** variance within the cloud of points along the axis directions corresponding to plot c). Note, the black and white grid serves purely as visualization aid. source: Powell and Lehe (14.03.2016)

To analyze the cyclone intensification events in terms of the principal components the cloud of points is described in the principal component space. Each event has 29 new values which position it in the principal component space, the i^{th} value is called the *score* for the i^{th} principal component. In summary Fig: 2.3 shows that the cloud of points is unchanged by the principal component analysis, only the description of the points has been altered due to the rotation of the axes.
As mentioned above, the first few pc's capture a large amount of the variance within the data set (cf. Fig: 2.3). When the variance explained by a parameter drops to the same value as the noise in a randomly chosen data set of the same size, that parameter contains very little information(Abdi, 2003). For a data set of 30 parameters the noise level in variance lies at 3%, therefore parameters explaining $\leq 3\%$ can be neglected from the analysis. By neglecting all principal components below a certain explained variance threshold, the dimensions of the data set can be reduced. The threshold should be chosen such that the ratio of retained information to dimensionality reduction is appropriate for the application.

Varimax Rotation
The interpretation of the PCA is facilitated if the coefficient values are either close to 0 or close to 1 (Abdi, 2003). The PCA, as described above, makes no attempt to achieve this. A varimax rotation is an operator that rotates a given set of vectors in order to make the coefficient values close to either 0 or 1, while keeping the vectors orthogonal. The varimax rotation is now mathematically described, and a visualization can be seen in Sec: 4.2, where this method is applied to the actual cyclone intensification data.
The technique used by the varimax algorithm to achieve coefficient values close to either 0 or 1, is to maximize the variance of the coefficients within each principal component. Let $v_p \in \mathbb{R}^n$, $p = 1, \ldots, n$ denote the p^{th} principal component, with n as the number of physical parameters used in the analysis. The i^{th} element of v_p corresponds to the coefficients defined above and is denoted $v_{p,i}$. The following can thus be calculated:

$$\begin{aligned} \mu_p &= \frac{1}{n}\sum_{i=1}^{n} v_{p,i} && \text{mean of coefficients of } v_p, \\ \sigma_p^2 &= \frac{1}{n}\sum_{i=1}^{n} \left(v_{p,i} - \mu_p\right)^2 && \text{variance of coefficients of } v_p. \end{aligned} \tag{2.6}$$

The varimax algorithm can be applied to any selection of the principal components. Consider the choice of the first 4 principal components. The varimax algorithm finds the a new set of axes to replace the principal components $v_1, \ldots, v_4$ that maximizes:

$$\sum_{p=1}^{4} \sigma_p^2 \tag{2.7}$$

such that the new axes remain orthogonal. These new axes are called *components*.
A new *rotated component space* is constructed by taking the 4 new components from the varimax algorithm and combining them with the remaining unrotated principal components (i.e., $v_5, \ldots, v_n$). Similar to the description for the principal component space above, each of the cyclone intensification events has a new set of scores for the 4 rotated axes.
To summarize how these two methods can be used to complement each other. The PCA is used to identify a limited number of directions which explain the majority of the information contained in the data set. The varimax rotation is then applied to the identified directions to make the interpretation of the analysis more reasonable from a physical point of view.
Applying the PCA and varimax rotation as described is done to determine the statistically and physically most reasonable representation of the data. Using the first and second component permits to visualize the best possible 2D-representation of the multi-dimensional data (Jolliffe, 2002). Note, however, the rotation leads to covariance between the rotated axes, this and the user defined selection of principal component axes included in the rotation, introduce subjectivity into the classification method.

2.5 Biplot & classification

Biplot
A biplot allows large data sets to be represented (Gabriel, 1971). It is used to represent data from a multi-dimensional space in only two dimensions.
The biplot comprises several items conveying information (cf. Fig: 2.4). The axes are vectors within the parameter space, here chosen based on a PCA and then rotated by applying a varimax rotation (cf. Sec: 2.4). The points represent the location of each data point projected onto the chosen axes (based on the scores), and the different vectors describe the coefficients of the axes for every one of the parameters included in the original data set. These vectors indicate in which direction the value of a (for this case) physical parameter varies within the data set of points. A short vector indicates that the parameter either only varies very little, or that it varies more in a higher dimension. Vectors which are orthogonal to each other in direction can be considered to be linearly uncorrelated. The correlation coefficient can be estimated by calculating the cosine of the angle between the vectors of the two parameters. Two vectors which point into the same (opposite) direction have a positive (negative) linear correlation (Gabriel, 1971).
The classes are defined within the 2-dimensional space of the biplot, using the first two rotated components, as the axes. The cases in the Bi-Pot are separated into 5 different classes, where class 1 comprises all cases in the lower left quadrant, class 2 all cases located in the lower right quadrant, class 3 all cases in the upper left quadrant, and class 4 all cases which lie in the upper right quadrant. Class 5 is the middle class. It is defined such that it is a circle, with a radius from the origin, which comprises 20% of the total amount of cases.

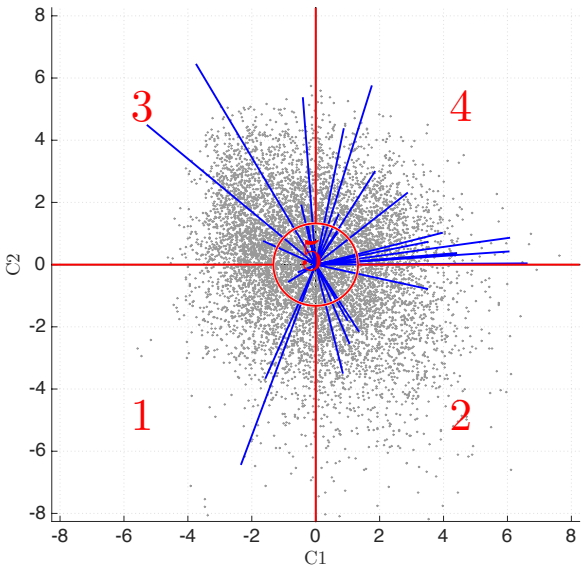

Figure 2.4: Example biplot: With first (second) component from varimax rotation (cf. Sec: 2.4) in horizontal (vertical) direction. The grey points represent the new set of scores of the events in the rotated component space. The blue vectors represent the coefficients for each parameter of C1 and C2. They show in which direction each parameter varies within the events in this projection. The red lines mark the class boarders and the red numbers label them 1-5.

Chapter 3

Case Studies

This section offers a brief insight into 3 extratropical cyclone cases, which underwent explosive deepening over the North Atlantic. They all caused considerable damage in Europe (Fink et al., 2012). Xynthia (February 2010) and Klaus (January 2009) are examples of storms which were greatly influenced by the contribution of diabatic processes, whereas Martin (December 1999) seems to have been driven more by horizontal temperature advection due to strong baroclinicity (Fink et al., 2012).
The 3 winter storm case studies are discussed separately in the following 3 sections. Each case study starts with a brief summary of the impact and highlights some findings from previous studies. A synoptic-scale analysis of the geographical setting then offers an overview over the path of the storm (subplot a)) and the corresponding values of CCP i.e. the SLP at the core of the storm (subplot b)). Subplots for each corresponding case, also show fields of the physical conditions at PMI. They display the instantaneous absolute values of PV at 310K (subplot c)), PV at 850hPa and SLP (subplot d)), VEL and U,V at 350hPa (subplot e)), θ_e at 850hPa and RTOT the 6-hour accumulated precipitation (subplot f)). In a final sub-section for each case study, 9 of the 29 physical parameters which are the basis of the classification (cf. Sec: 2.2 and Tab: 2.1) are discussed. A figure with subplots of the 9 parameters within the 12 hour-period before, and after the PMI, serves to illustrate the analysis. The PMI is the time point the analysis refers to in all other time points within the phase of maximum intensification being PMI±6(h) PMI±12(h), respectively. The development over 24 hours allows a better understanding of the development of the depicted parameters. Note, for this discussion the physical parameter values (A) are used before normalization (A_{norm}) (cf. Sec: 2.3) as it makes the plots easier to interpret.

3.1 Martin

Martin was a winter storm, which occurred in December 1999. This extratropical cyclone followed the storm Lothar and lasted form the 25th of December to the morning of the 1st of January. It was accompanied by strong winds which reached their maximum speed in the evening of the 27th just before landfall (N.N., 2000). This led to a strong storm surge and thus flooding at the Atlantic coast (Ulbrich et al., 2001).
According to previous studies, synoptic scale characteristics which prevailed during the event were high baroclinicity near the track of the core and an airmass with high θ_e south of the track (Ulbrich et al., 2001). The release of latent heat from that airmass contributed to the cyclone growth and intensification (Ulbrich et al., 2001). In addition the storm was associated with a strong polar jet (cf. Fink et al. (2012) and Ulbrich et al. (2001)).

3.1.1 Synoptic-Scale Geographical Setting

The 24h period between 18UTC 26 Dec. 1999 - 18UTC 27 Dec. 1999 marks Martin's phase of maximum intensification. The mid point representing this phase at PMI, 06UTC 27 Dec.. The

subplots in Fig: 3.1 show details of the synoptic-scale setting. The track starts in the west atlantic, the markers (of each morning) indicate that martin started with a slow movement to the east and north-west, and accelerated eastwards after the 26^{th} at 00UTC. Along with the fast propagation to the east, the CCP decreased drastically (1010 to 970 hPa).
The cyclone centre is positioned at 16°W/47°N at PMI. Several pronounced features can be observed concerning the position of the cyclone centre at this time: Martin is positioned east of an upper level trough and PV at low levels show increased values. Zonal wind velocities at upper levels are at a local maximum, representing the jet streak. A band of 6-hour accumulated precipitation (RTOT) lies on top of the distinct gradient of θ_e which stretches east marking the baroclinic zone.

3.1.2 Parameter Values in the Cyclone Domain

Prior to PMI a positive PV_{up} anomaly is visible north west of the cyclone centre (cf. Fig: 3.2). The anomaly gets closer to the centre of the cyclone, and moves into the area within the grey dashed circle, the CIR (cf. Sec: 2.3) at PMI. At PMI+6 values of more than 2 PVU are visible at the centre of Martin (not displayed). The position and strength of the $qg\omega_{top}$-lifting is closely related to the movement of the positive PV_{up} anomaly. $Qg\omega_{top}$-lifting occurs downstream of the anomaly. It leads to increased upper level divergence, contributing to the intensification of the cyclone. The absolute values of PV_{low} are slightly higher close to the centre compared to the surrounding area. The values increase from 1 to 1.5 PVU between PMI-6 to PMI+6 (not displayed), after which the value falls back below 1 PVU. The described positive PV_{up} and PV_{low} anomalies are offset, suggesting a westward tilt. Their interaction contributes to the intensification (cf. Hoskins et al. (1985), Davis and Emanuel (1991), and Huo et al. (1999)). The PV_{up} and PV_{low} anomalies then come to overlap each other creating a column like structure of positive PV starting at PMI+6 (not displayed), which leads to erosion of the positive PV_{low} anomaly. Throughout the phase of maximum intensification the centre of the cyclone is positioned on a significant gradient of θ_{e850}. The gradient starts to weaken at PMI. The values of EADY highlight areas of baroclinic instability. A continuous band of high EADY values stretches across the subplot of PMI-12 with the cyclone centre positioned on it. At PMI the band shows a kink at the cyclone centre and separates into two strands, marking the position of the cold and warm front of Martin at PMI+12. SLP shows a strong gradient south of the cyclone centre, forming an omega-shaped structure open to the north throughout the 24h period. At PMI+6 (not displayed) a closed contour of 985 hPa is visible around the centre. Prior to PMI the cyclone centre is positioned south of, at PMI it is situated exactly on, and after PMI the centre is positioned north of the maximum wind speeds of VELJET. Hence, Martin passes underneath the jet, which contributes to its intensification (cf. Uccellini and Johnson (1979) and Gilet et al. (2009)). Positive and negative T_{ADV850} is less pronounced before PMI and reaches its maximum values and extent within CIR at PMI+6 (not displayed). This leads to suggest that the winds accompanying the cyclone, slowly erode/decrease the gradient of θ_{e850}. RR_{6h} shows high values at the centre of the cyclone and within the CIR at all time steps. Additionally, a strand of precipitation can also be observed upstream of the CIR lying on the gradient of θ_{e850} up until PMI.
The start of the phase of maximum intensification is dominated by baroclinicity. The available energy is drawn from the gradient of θ_{e850} and converted into kinetic energy fed to the cyclonic circulation of Martin. As a result the T_{ADV850} increases at PMI. At this point the centre of Martin is located right under the jet, and then moves north ending in its left exit region which is known to to be dominated by vertical upward movement (cf. Uccellini and Johnson (1979) and Gilet et al. (2009)). Being in the left exit region of the jet thus further intensifies the cyclone.

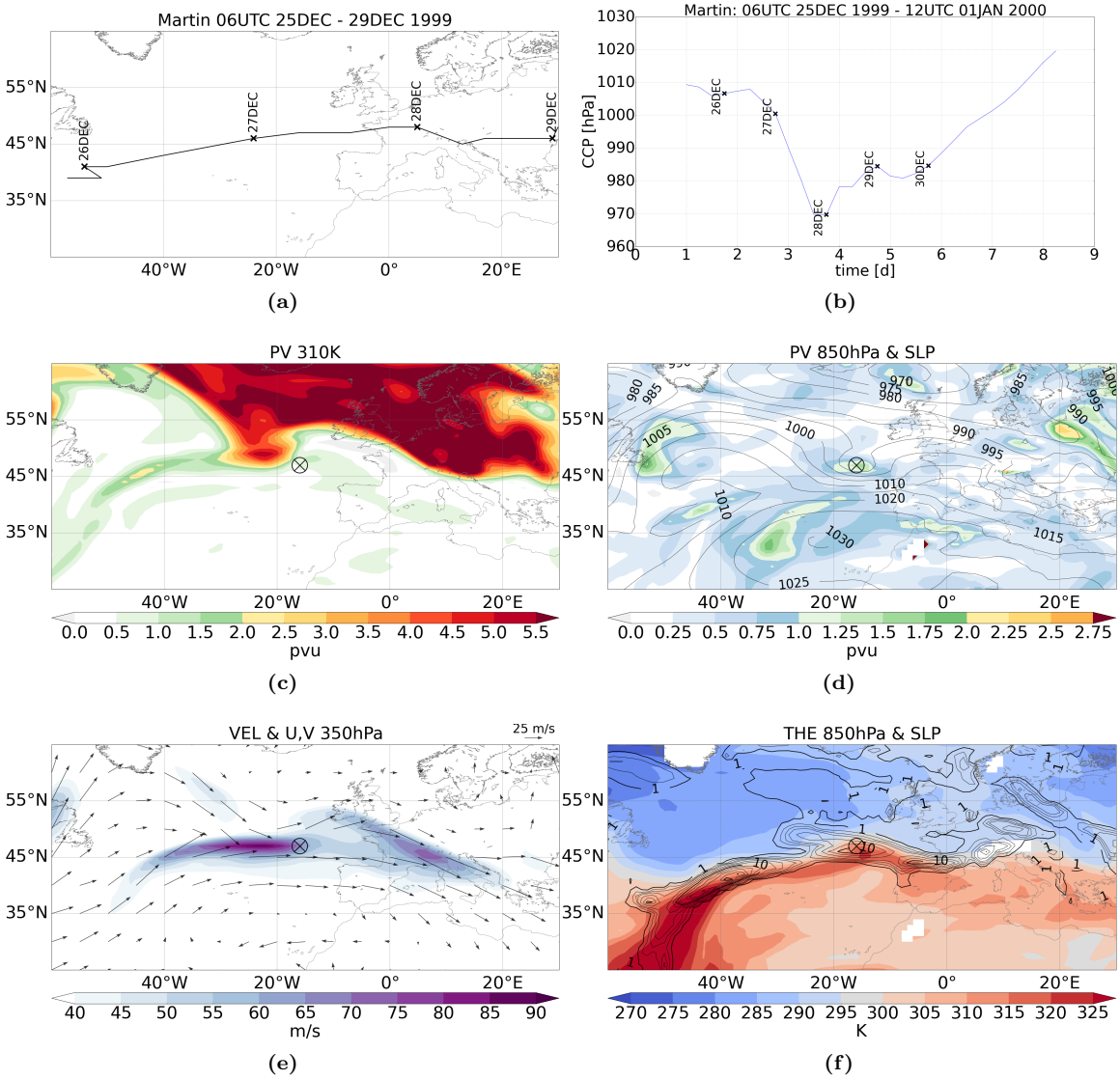

Figure 3.1: Overview at point of maximum intensification Martin, 27 Dec. 1999 06 UTC, incl. track and CCP. Synoptic situation of the case depicts absolute values of a selection of physical terms which are considered as relevant for the genesis and intensification of cyclones. The black circle with the cross solely marks the position of the cyclone (point of CCP) at the corresponding time point. **a)** overview over the path **b)** corresponding values of CCP **c)** potential vorticity PV at 310 K in PVU (filled contours); **d)** potential vorticity PV at 850 hPa in PVU (filled contours) and sea level pressure (black contours); **e)** wind velocity VEL in m/s (filled contours) and wind direction U,V (black arrows), all at 350 hPa; **f)** potential equivalent temperature θ_e at 850 hPa (filled contours) and 6-hour accumulated precipitation RTOT (black contours) in steps of 1 (up to 4mm), steps of 2 (up to 20), and steps of 5 mm/6h for all subsequent amounts.

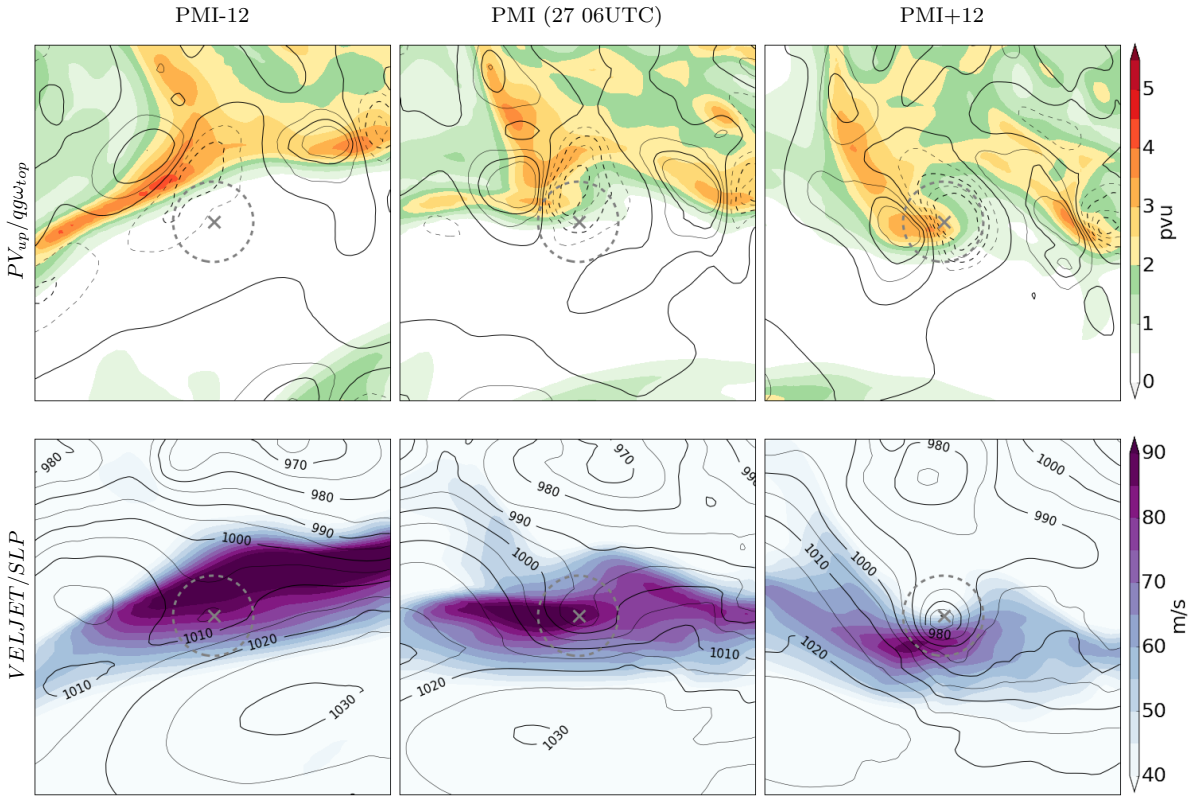

Figure 3.2: Martin 00 UTC 27 Dec. 1999 - 12 UTC 27 Dec. 1999, 12h time steps. Sub figures display the synoptic situation of the case in the cyclone domain, an area of +-20° around the position of the cyclone at the corresponding time point. It depicts values of a selection of physical parameters which are considered relevant for the genesis and intensification of cyclones. The grey cross marks the position of the centre of the cyclone. The grey dashed line encompasses the CIR (cyclone intensification region) with the cyclone centre at its centre and a radius of 500km. row1: PV_{up} in PVU (filled contours) and $qg\omega_{top}$ (black contours) in steps of $2 \cdot 10^{-2}$ Pas^{-1}, full lines mark descent, dashed lines mark ascent; row2: VELJET in m/s (filled contours) and SLP (black contours) in steps of $5hPa$.

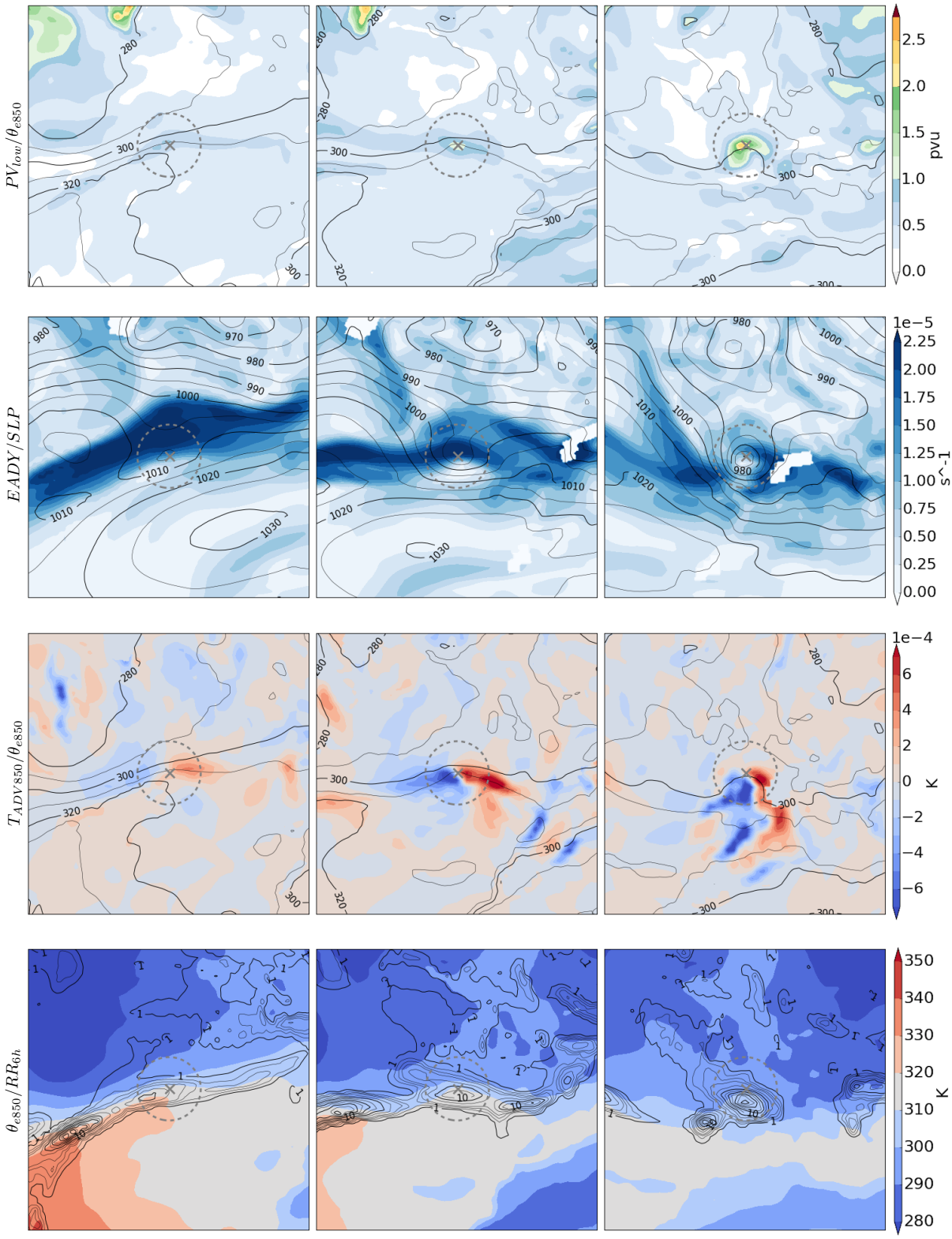

Figure 3.2: (continued) Martin Dec 1999 27 00 UTC - 27 12 UTC, 12h time steps row3: PV_{low} in PVU (filled contours) and θ_{e850} (black contours) in steps of $10K$; row4: EADY in $10^{-5}s^{-1}$ (filled contours) and SLP (black contours) in steps of $5hPa$; row5: T_{ADV850} in K (filled contours) and θ_{e850} (black contours) in steps of $10K$; row6: θ_{e850} in K (filled contours) and RR_{6h} in $mm/6h$.

3.2 Klaus

Winter storm Klaus occurred in January 2009. It started in the mid-atlantic at 06 UTC 23 Jan. 2009. Klaus moved east into the bay of Biscay and continued south-east after landfall in France. It dissipated over the Adriatic sea 42 hours later (00 UTC 25 Jan. 2009) (cf. Fig: 3.3). In previous studies Klaus was identified and tracked for longer (earlier start/later end date) which can be attributed to the difference in identification-, and tracking-tool used, as well as the resolution of the analyzed data.
The impact of this extratropical cyclone was primarily characterized by strong winds and heavy precipitation (Liberato et al., 2011). Its intensification was closely connected to its position relative to the jet stream and the gradient of θ (Liberato et al., 2013). Even though Klaus was in a similar synoptic situation concerning the jet strengths and θ of southern air masses, it showed larger contributions from diabatic processes to its intensification, than Martin (1999) (Fink et al., 2012). The storm was embedded in an event of "tropical moisture exports" (TME)[1] over the north atlantic. Hence, latent heat release within the imported moist air likely contributed to the intensification as an additional source of energy (Knippertz and Wernli, 2010).

3.2.1 Synoptic-Scale Geographical Setting

The CCP dropped drastically from (already low) 995 hPa to less than 970 hPa within the first 18 hours along the track, depicted in Fig: 3.3 and described in the previous section. After another 6 hours of very low CCP, the pressure at the core of the cyclone started to increase again. Based on the identification-, and tracking-tool used (Wernli and Schwierz, 2006), the 24 hour period between Jan 2009 23 06UTC - 24 06UTC 2009 marks the whole phase of Klaus' maximum intensification, where PMI is at 18 UTC 23 Jan. 2009.
At PMI the cyclone centre is positioned above the North Atlantic south west of the Iberian Peninsula, at 13°W/46°N. A number of pronounced features can be observed concerning the position of the cyclone centre at PMI: Klaus lies south east of an upper level trough and a band of positive PV anomaly stretches from the trough's tip south east almost reaching the centre of the cyclone. Further downstream a second, more prominent trough can be observed. The upper level wind velocities (VEL) south of the cyclone centre show a local maximum of up to 60-65 m/s. The wind direction at 350 hPa follows the gradient between the high and low PV values at 310 K, tracing the shape of the two troughs. Low level PV (at 850 hPa) has a local maximum with values over $2pvu$ close to the centre of Klaus. South of the centre more positive PV-anomalies can be seen positioned on the cold front. The baroclinic zone stretches south west across the North Atlantic. RTOT (precipitation) occurs in an oval shaped area with values over 10 mm accumulated precipitation at the centre of Klaus.

3.2.2 Parameter Values in the Cyclone Domain

PV_{up} shows values above 2 pvu in the positive PV anomaly west of the centre of Klaus before PMI. The anomaly then curls around it and into the CIR on its west and south side. $Qg\omega_{top}$-lifting is prevalent over the 24 hours of maximum intensification. In addition it is relatively stationary above the centre, offset slightly to the north west. After PMI the $qg\omega_{top}$-lifting moves across and past the centre of Klaus. The location of the lifting is related to the position of the centre of Klaus in relation to the jet axis. At PMI-12 the cyclone centre is positioned at the maximum wind speeds of the jet (VELJET). In consecutive time steps it moves north of the maximum wind speeds of VELJET. Klaus passes underneath the jet between PMI-12 and PMI after which it is positioned in the left exit region. The upward motion of air in that location relative to the jet contributes to its intensification (cf. Uccellini and Johnson (1979) and Gilet et al. (2009)). The absolute values of PV_{low} show higher values within the CIR compared to the surrounding with a maximum of over $2PVU$ just west of the centre at PMI. This contributes to the intensification of the cyclone.

[1] "[...]TMEs are usually both spatially and temporally coherent airstreams that can (but do not necessarily) contribute to heavy precipitation events in the extratropics." (Knippertz and Wernli, 2010)

During the 24h of maximum intensification, Klaus is positioned in a baroclinic zone. At PMI the gradient of θ_{e850} close to the centre of the cyclone is slightly stronger than in the rest of the domain. The signal of EADY shows a connected band-like area of high values at PMI-12. This band decays over the following time steps developing a new strand along the western boarder of the positive PV_{up}-anomaly which crosses the centre of Klaus. SLP shows a strong gradient south west of the cyclone's centre in all subplots. The closed SLP contour surrounding the centre of the cyclone at PMI shows values of only 875hPa. Positive and negative temperature advection (T_{ADV850}) is prevalent throughout the phase of maximum intensification. It is strongest at PMI-6 (not displayed) and weakest at PMI+12. The persisting temperature advection indicates strong winds and leads to a reduction in baroclinicity. The 6-hour accumulated precipitation shows a local maximum within the CIR and exactly at the cyclone centre. This positioning correlates with the higher values of PV_{low} at the same location. Hence, the positive PV anomaly in the lower troposphere (PV_{low}) is largely induced by diabatic processes.

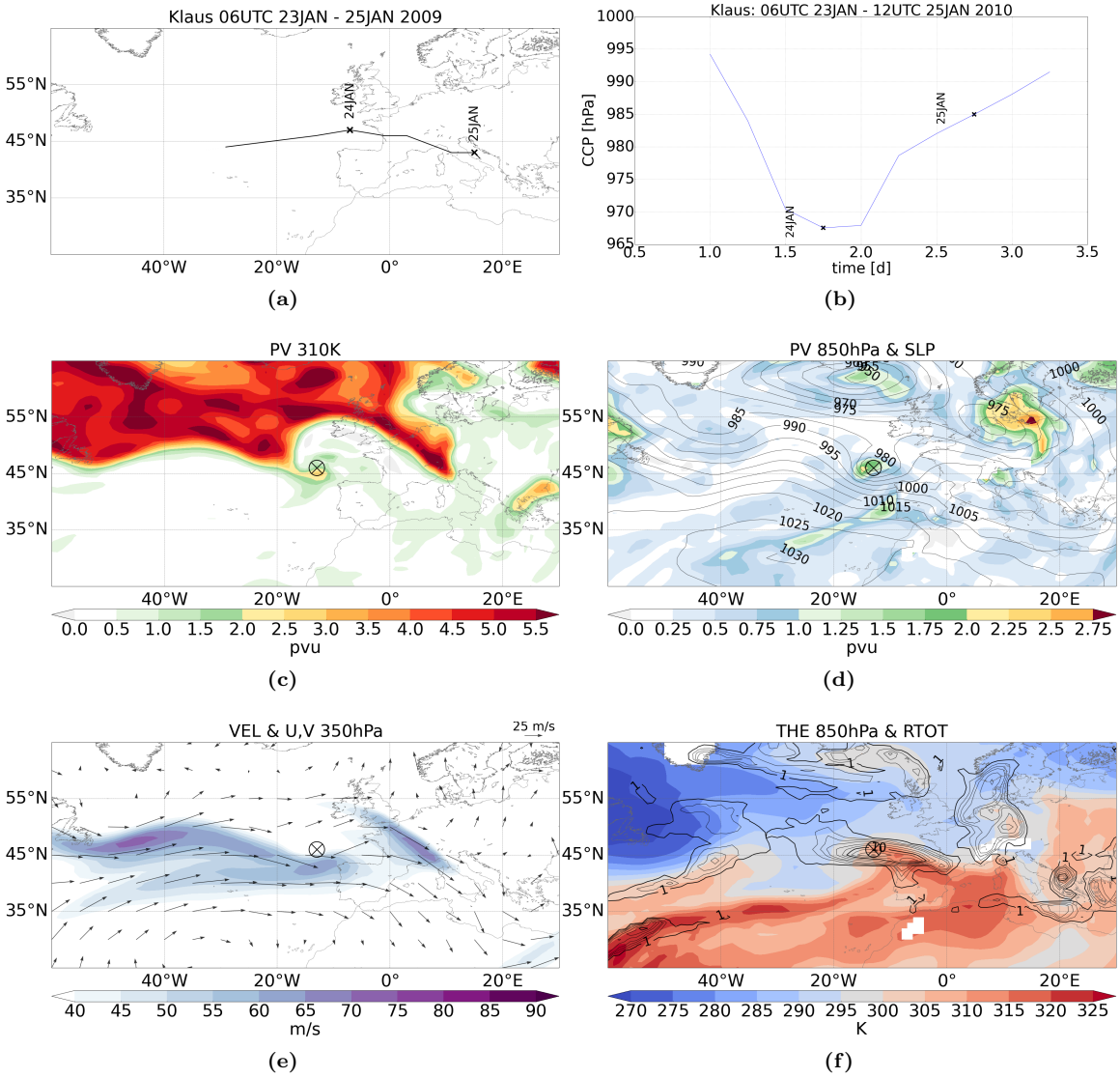

Figure 3.3: Overview at point of maximum intensification Klaus 23 Jan 2009 18UTC, incl. track and CCP. For a description cf. Fig: 3.1.

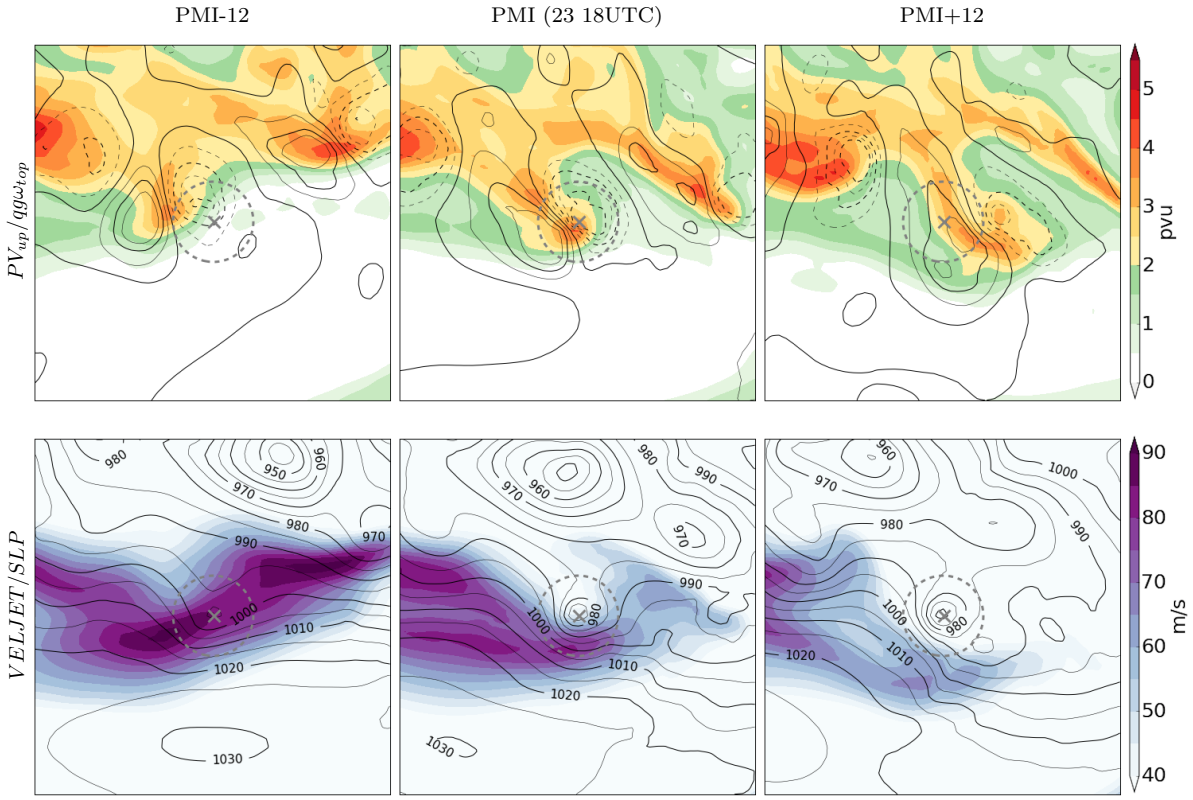

Figure 3.4: Klaus Jan 2009 23 06 UTC - 24 06 UTC, 12h time steps. For a description cf. Fig: 3.2.

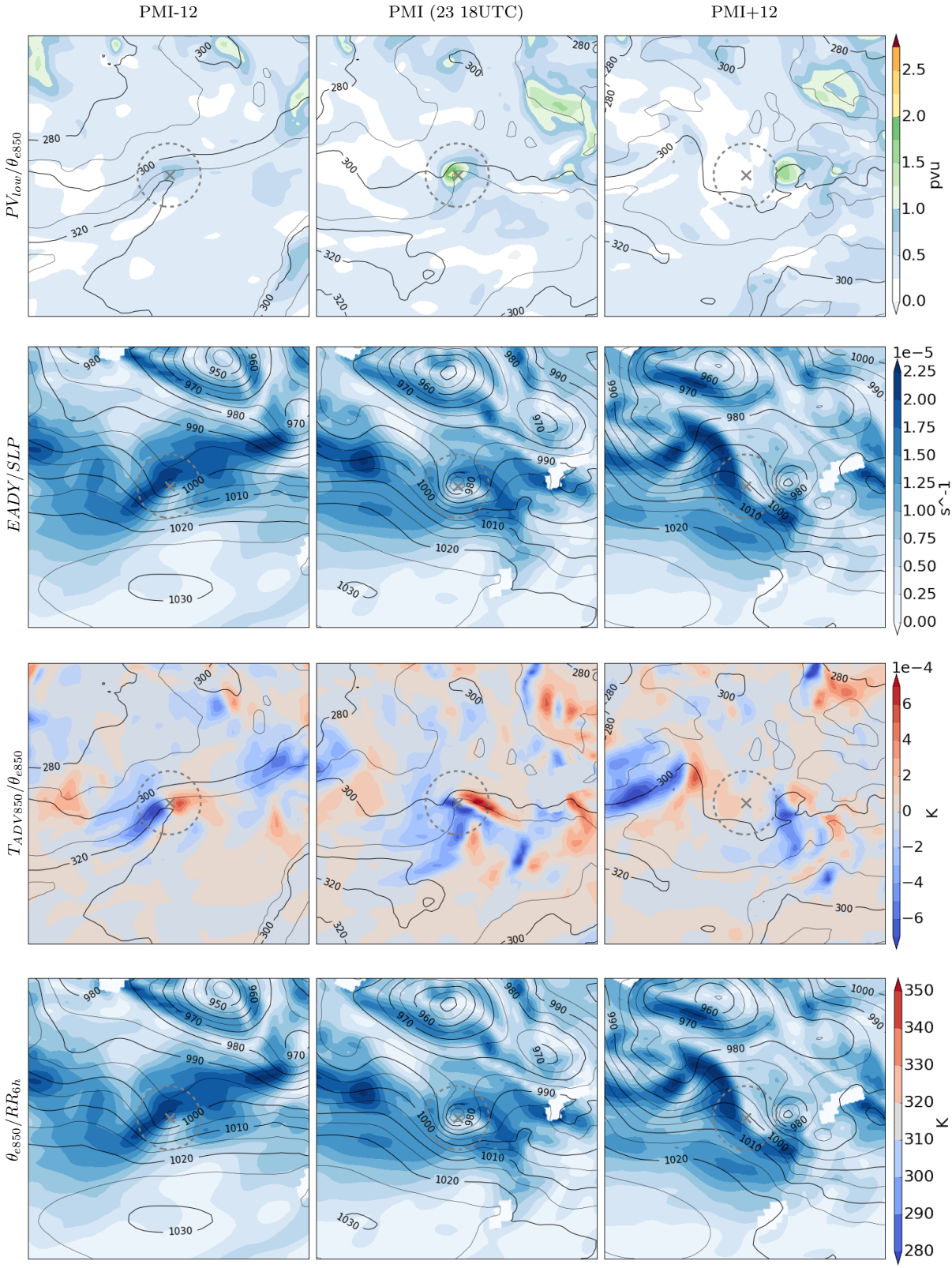

Figure 3.4: (continued) Klaus Jan 2009 23 06 UTC - 24 06 UTC, 12h time steps. For a description cf. Fig: 3.2.

3.3 Xynthia

The winter storm called Xynthia occurred in February 2010. The event caused 64 reported casualties and an estimated total of EUR 3.6 billion in economic losses. The coinciding storm surge, high tides, and high wind speeds lead to destructive flooding along costal areas. (Liberato et al., 2013)
Different to Martin and Klaus, jet-induced upper-level divergence did not contribute to the intensification of Xynthia (Fink et al., 2012). According to Ludwig et al. (2014) a split jet stream structure did however play a role for the genesis of the storm. Xynthia developed far in the south above the North Atlantic in a Region with high sea surface temperatures (SST) (Ludwig et al., 2014). It crossed the canaries and parts of Europe accompanied by strong winds (Liberato et al., 2013). This storm stands out due to its south-west north-east track into the european continent. Important for the phase of maximum intensification, were diabatic processes fueled by high SST resulting in warm moist air masses (Ludwig et al., 2014).

3.3.1 Synoptic-Scale Geographical Setting

The track shows that Xynthia moved south east after its genesis and then started a fast propagation north east from 06UTC 26 FEB. The CCP started decreasing before the 26 (00UTC) and kept dropping up until the 28th 00UTC when it reached its lowest point. Interestingly the cyclone did not slow upon landfall early on the 28th (cf. Fig: 3.5 subplot a)).
On 26 February 2011 at 18 UTC (PMI) the cyclone centre is positioned far south above the Atlantic Ocean off the West African coast, at 26°W/29°N. Based on subplots c) to f) a number of pronounced features can be observed concerning the position of the cyclone centre at PMI: Xynthia is positioned in a largely zonal baroclinic zone above the ocean, located in an area dominated by warm and moist air masses. In addition the centre is at the south-west end of an elongated positive PV-anomaly at 850 hPa. This positive PV-anomaly coincides with the centre of a larger area experiencing precipitation. A local maximum of almost 20 mm of accumulated precipitation over the preceding 6 hours is depicted surrounding the centre of Xynthia. A trough of positive PV at 310 K is located north west of the centre and the wind velocities at 350 hPa barely show values above 40 m/s close to the cyclone. The values of PV at 310 K and VEL in the vicinity of the cyclone centre lead to suspect that PV at upper-levels and the jet velocity play only a minor role in the phase of maximum intensification of Xynthia.

3.3.2 Parameter Values in the Cyclone Domain

In contrast to the values of potential vorticity at 310 K (cf. Fig: 3.5c), PV_{up} shows values above 2 pvu close to the centre and within the CIR. A positive PV_{up} anomaly lies north west of the centre at PMI-12. At PMI the tip of the north-west oriented band of PV_{up} reaches the centre of the cyclone. $Qg\omega_{top}$-lifting occurs ahead of the positive PV_{up} in all time steps, changing from being positioned north-east of the centre to lying exactly on it (PMI+6, not shown). The maximum wind speeds of VELJET in the subplots are low at the centre and within the CIR during the phase of maximum intensification of Xynthia. This supports the initial conclusion of limited influence of this parameter on the intensification of the cyclone. The values of VELJET are however higher down- and upstream of the CIR. The position of the cyclone, in relation to the exits and entrances of the two VELJET maxima, does not allow a clear interpretation concerning its contribution to the intensification. The absolute values of PV_{low} show higher values within the CIR compared to the surrounding with the maximum not exceeding 2 pvu in all time steps. The shape of PV_{low} at PMI is similar to the shape of the positive PV anomaly at 850 hPa (cf. Fig: 3.5d). High values of PV occur throughout the lower troposphere (up to 600 hPa). Hence, PV_{low} largely contributes to the intensification of Xynthia. Up to PMI the gradient of θ_{e850} close to the centre of the cyclone is slightly stronger than in the rest of the domain. The strength of the baroclinic zone is transferred into kinetic energy and thus decreases over time. EADY shows increased values north of the CIR tracing the gradient of θ_{e850} (310 K contour). At PMI and the following time steps

high values of EADY move into the CIR and intensify still molding to the gradient of θ_{e850}. This can lead to increased instability in the troposphere. The gradient of SLP with closed contours at the cyclone's centre increases over time, documenting the intensification of Xynthia. Positive and negative temperature advection (T_{ADV850}) barely occurs until after PMI. This also suggests that the strength of the baroclinicity decreases over time. The 6-hour accumulated precipitation (RR_{6h}) shows a strong local maximum within the CIR and at the cyclone centre during all time steps of the phase of maximum intensification. The positioning and also the shape correlates with the higher values of PV_{low} at the same location. This indicates diabatic PV-production contributing to the intensification.

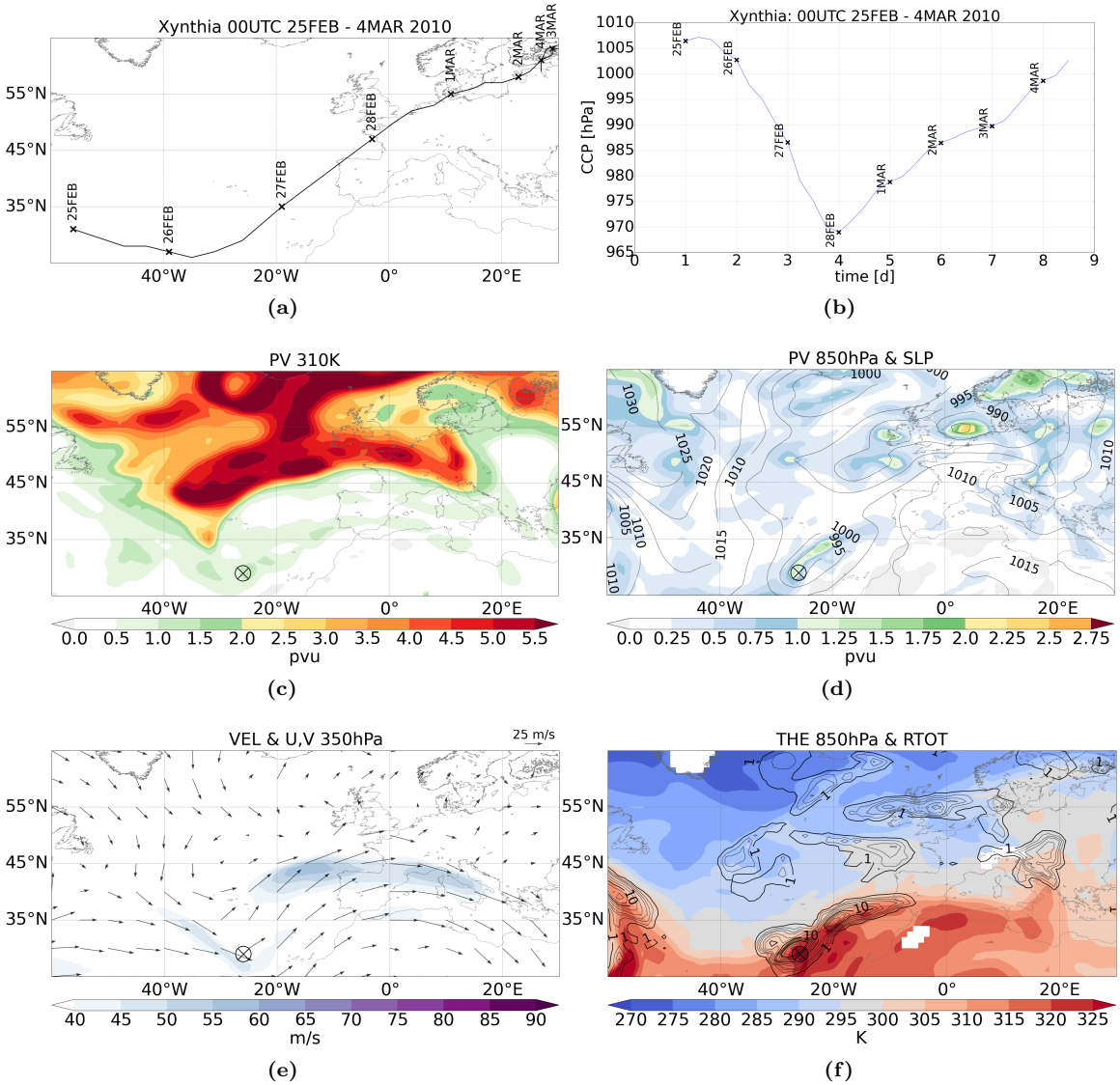

Figure 3.5: Overview at point of maximum intensification Xynthia 26 February 2010 18UTC, incl. track and CCP. For a description cf. Fig: 3.1.

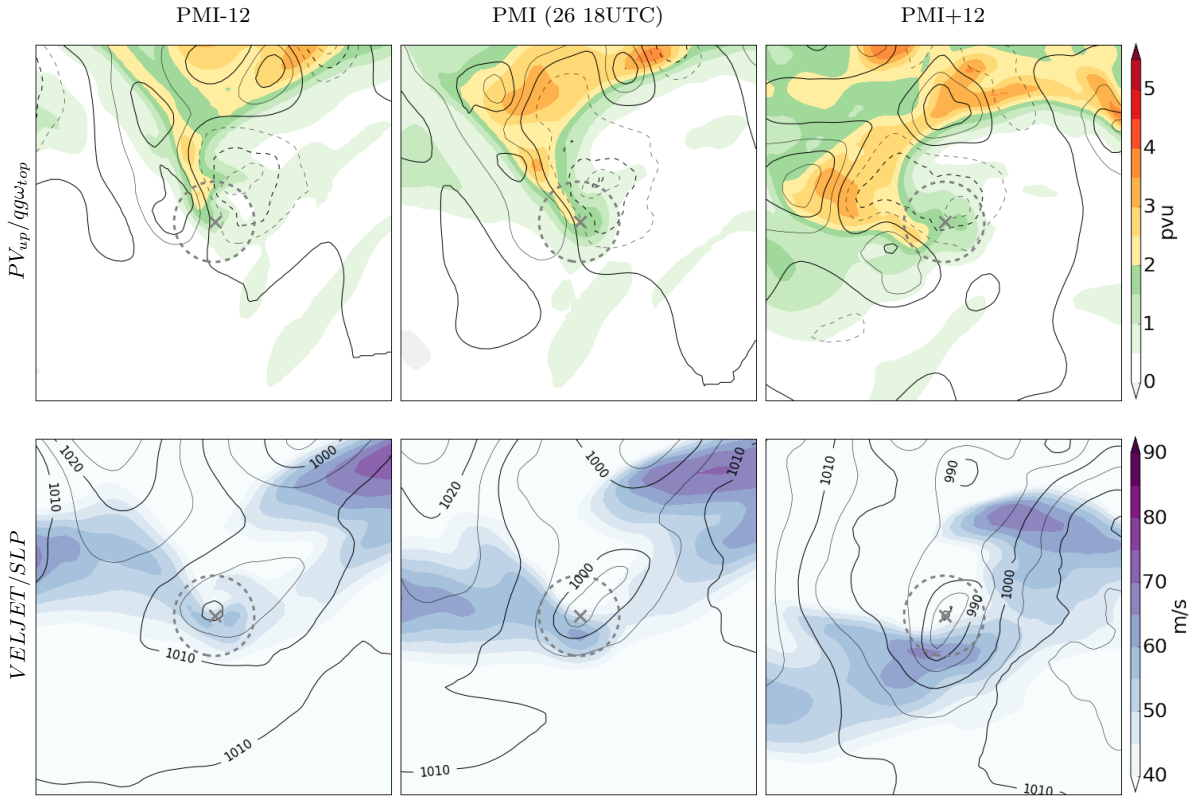

Figure 3.6: Xynthia Feb 2010 26 06 UTC - 27 06 UTC, 12h time steps. For a description cf. Fig: 3.2.

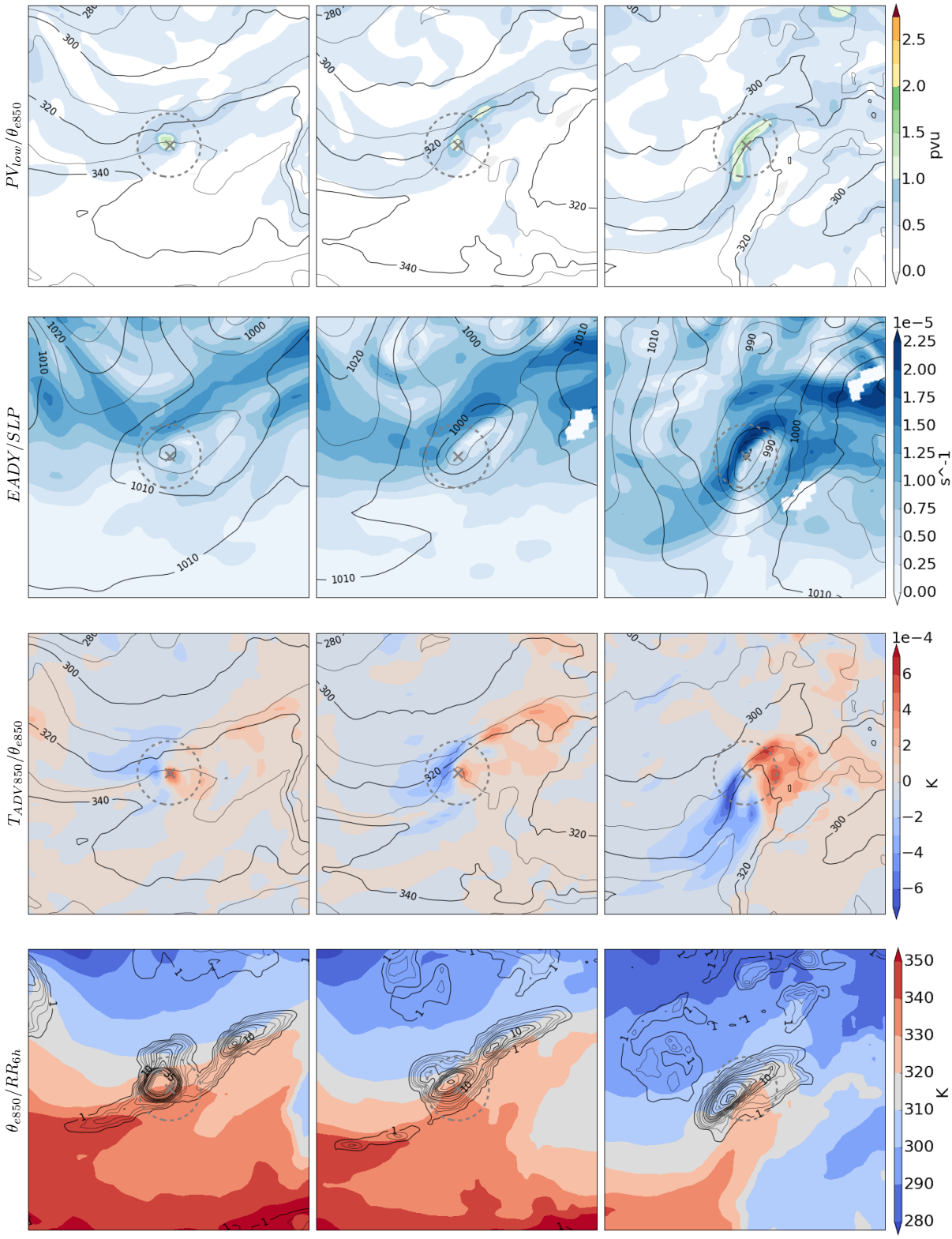

Figure 3.6: (continued) Xynthia Feb 2010 26 06 UTC - 27 06 UTC, 12h time steps. For a description cf. Fig: 3.2.

Chapter 4

Objective Classification

The aim of this chapter is to give an in depth explanation of the final steps for the objective classification, of the ($\sim$ 8000) cyclone intensification events, based on the 29 single physical parameter values (cf. Sec: 2.3). The chapter begins with the discussion of frequency distributions and linear correlations of the parameter values across the different cases. It then provides insight into the biplot created from the PCA and the subsequent varimax rotation (cf. Sec: 2.4), which precedes the determination of the class borders.

4.1 Uni-variate statistics

4.1.1 Distribution of parameter values

The histograms in Fig: 4.1 and Fig: 4.2 show the distributions of the extracted parameter values, computed as the deviation from the climatology (cf. Sec: 2.3), for each parameter separately. This section describes the characteristics of the frequency distributions in two separate groups: first, the distributions for those parameter values computed as an average below the median, and second, the distributions for those parameter values computed as an average above, the median. Separating the parameter distributions into those two groups facilitates making general statements in the visual analysis of the histograms. The two groups are discussed separately purely for convenience of explanation, and all parameters have equal importance for the subsequent analysis.

Parameters for which the parameter value is calculated below the median show a distribution with the median lying on the left of the 0-anomaly (cf. Fig: 4.1). The distributions of $qg\omega_{top}$ and $qg\omega_{bot}$ both lie almost fully below the 0-anomaly. The parameters $TRAdP_{MX}$ and $TRAdP_{48}$ show the second least amount of cases with parameter values above the 0-anomaly. The rest of the parameters show slightly more cases with positive parameter values. The distribution of the parameter of $TRAdP_{MX}$ and $TRAdP_{48}$ are characteristically slim (range of 4 standard deviations) and tall. The distribution of $qg\omega_{top}$ and $qg\omega_{bot}$ on the contrary are wider and contain cases with anomaly-values of less than -4 (range of 6 standard deviations). The widths of the other distributions lie between these two extremes.

Parameters for which the parameter value is calculated above the median show a tendency to lie mainly on the right of the 0-anomaly (cf. Fig: 4.2). For the parameters $FGEN_{850}$, T_{ADV850}, $TRAd\theta_{48}$ and $CAPE$, very few of the cases show values below the 0-anomaly. The values of the parameters DEF, $|\Delta\theta_{e850}|$, $SLHF$, $TRAd\theta_{MX}$, RR_{6h}, PV_{low}, and $UPPTIM$ are also above zero for many cases. The rest of the parameters show more values below zero in a greater number of cases. The distributions of $SSHF$, and $TRAd\theta_{MX}$ are particularly slim (4 standard deviations) and show high numbers (>1250) of cases at their peak. Distributions of RR_{6h}, PV_{low}, $FGEN_{850}$, and DEF on the other hand show a greater range of > 6 standard deviations. The distribution of the parameter $VELJET$ has the shape of a normal distribution with the centre lying almost at zero. The average above the mean for the jet velocities varies from < -2 to > 2 standard deviations.

Irrespective of whether the parameter values are calculated as averages above or below the median, the width of each distribution allows a preliminary interpretation. Parameters with a narrow distribution, and therefore high numbers of cases within a small range of standard deviations, can be considered as requirements for the physical condition at PMI. Hence, independent of the location of the mean value (if left, right, or on the 0-anomaly), a slim distribution, indicates that the parameter in question does not vary strongly from case to case. The mean of the parameter marks the average value "required" to occur during PMI. Parameters with a large range of standard deviations vary a lot from case to case, which could allow a value-dependent separation of the different cases into classes. This leads to suspect that parameters with a broader distribution are likely to play a bigger role in the PCA.

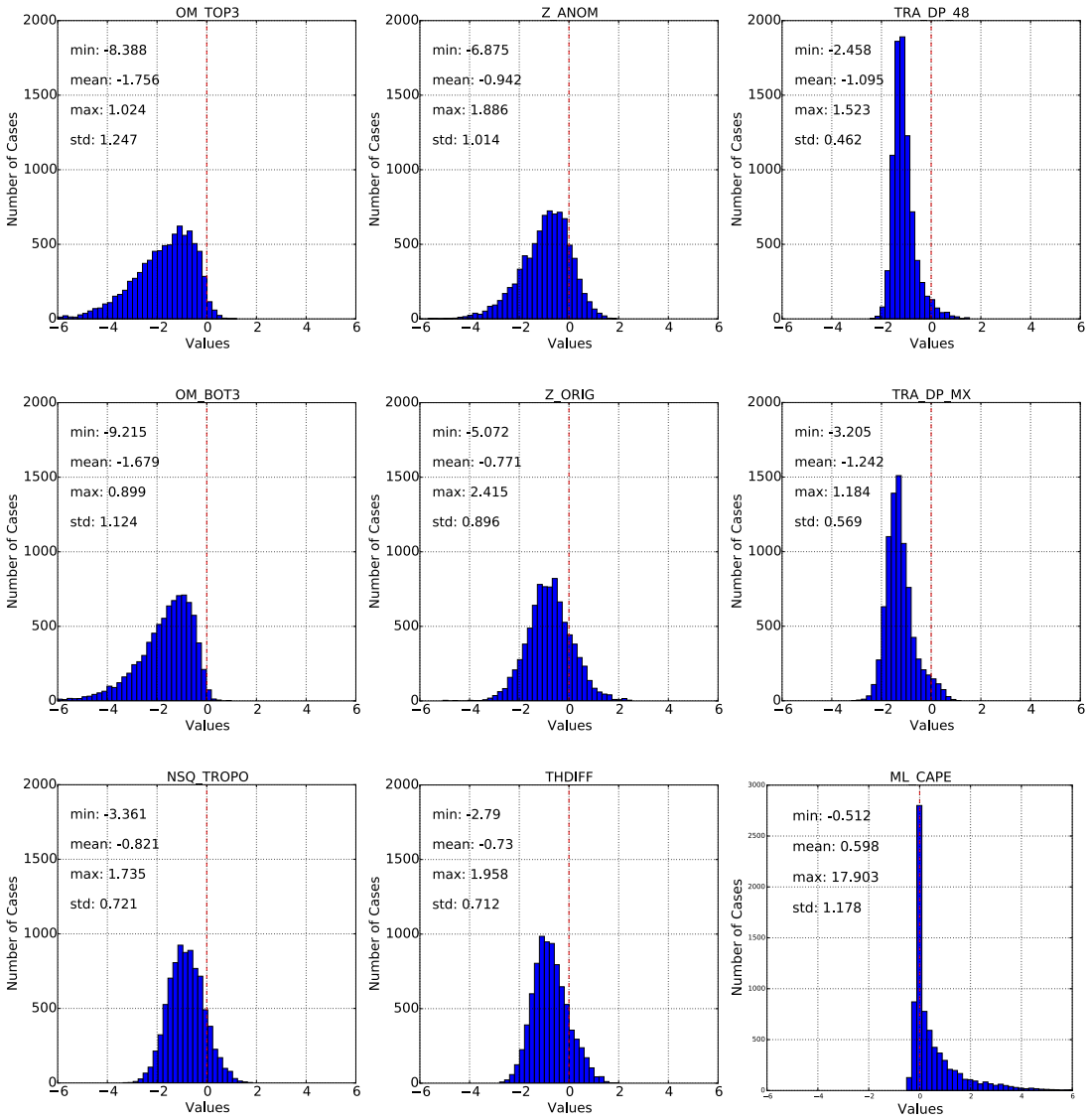

Figure 4.1: Frequency distribution: Parameter values which are calculated as average below the median. The horizontal axis shows the single parameter values. , i.e. the average standard deviation from the climatology (0-anomaly) within the CIR, calculated below the median, for every case. The vertical axis shows the number of cases with the corresponding parameter value. The $CAPE$ parameter has a differently scaled vertical axis. The titles of the subplots corespond to the different parameters: OM_TOP3 = $qg\omega top$, Z_ANOM = Z_{ANOM}, TRA_DP_48 = $TRAdP_{48}$, OM_BOT3 = $qg\omega bot$, Z_ORIG = Z_{500}, TRA_DP_MX = $TRAdP_{MX}$, NSQ_TOROPO = N^2_{TROPO}, THDIFF = $\Delta\theta_{SKT700}$, ML_CAPE = $CAPE$.

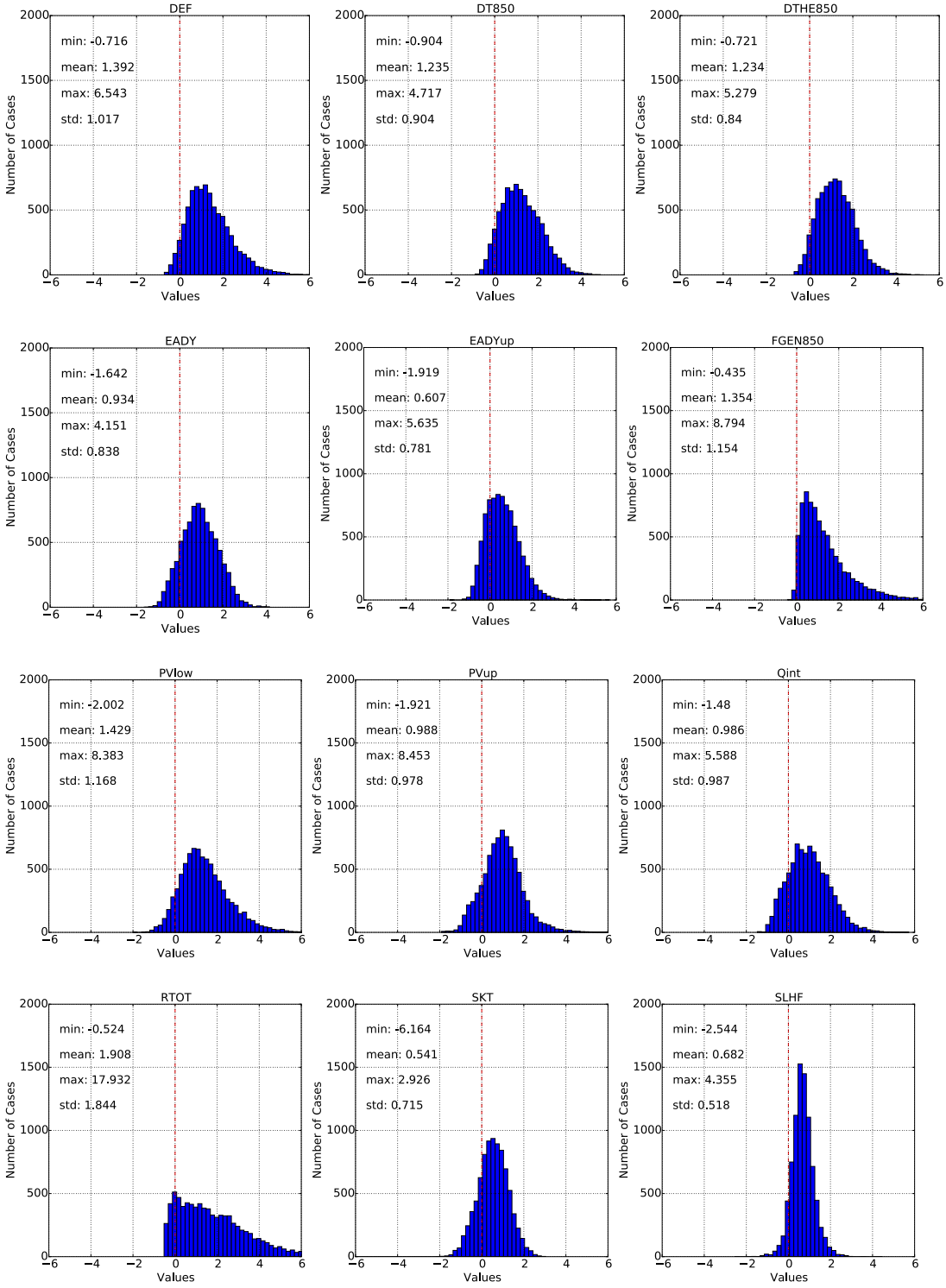

Figure 4.2: Frequency distribution: Parameter values which are calculated as average above the median. For a description cf. Fig: 4.1, but here for parameters where the value is calculated as average above the median. The titles of the subplots corespond to the different parameters: DEF = DEF, DT850 = $|\Delta\theta_{850}|$, DTHE850 = $|\Delta\theta_{e850}|$, EADY = $EADY$, EADYup = $EADY_{up}$, FGEN850 = $FGEN_{850}$, PVlow = PV_{low}, PVup = PV_{up}, Qint = Q_{int}, RTOT = RR_{6h}, SKT = SKT, SLHF = $SLHF$, SSHF = $SSHF$, T_PERT = T_{PERT}, TADV850 = T_{ADV850}, TRAD_DTH_48 = $TRAd\theta_{48}$, TRAD_DTH_MX = $TRAd\theta_{MX}$, UPPTIM = $UPPTIM$, VELJET = $VELJET$.

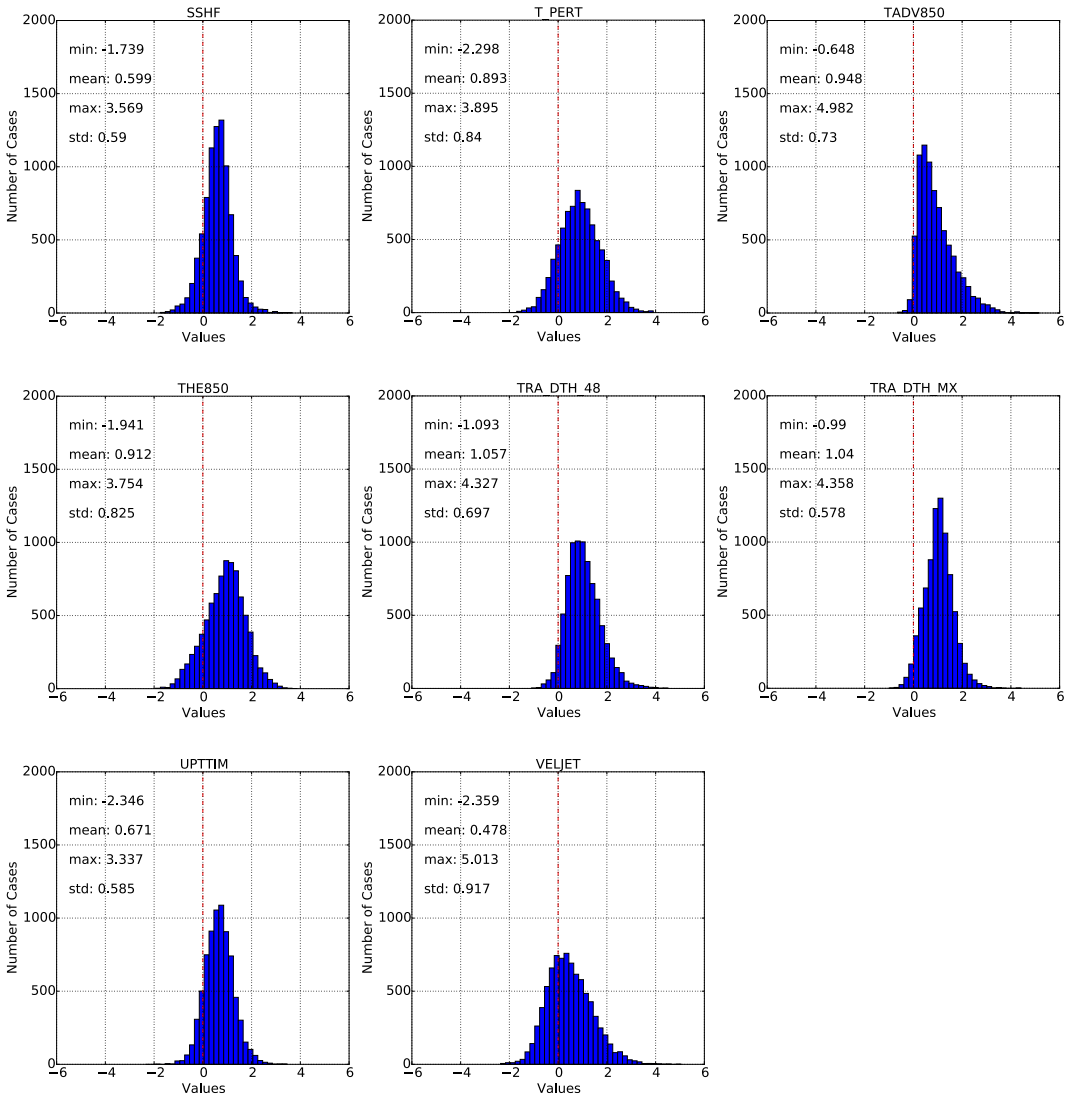

Figure 4.2: (continued) Frequency distribution: Parameter values which are calculated as average above the median.

4.1.2 Correlations between parameters

The PCA combines the distributions of the different parameters and their correlation with each other in a 29-dimensional space and then finds axes based on the variance (cf. Sec: 2.4). To break down the multi-dimensional parameter space (cf. Sec: 2.4), this section uses a simple 2-dimensional perspective to discuss how the different parameter values correlate with each other.
To determine whether a linear correlation exists between the different parameters, the coefficient of determination R^2 was calculated for every possible combination of a pair of 2 parameters. The majority of the parameter combinations have an R^2 value < 0.3. None of the parameters have an R^2 value > 0.76. Table 4.1 contains the combinations which have the 8 highest R^2 values. Two sets of scatter plots of the 8 different parameter pairs listed in Tab: 4.1, are displayed in Fig:4.3 (for more scatter plots see App: C).

Table 4.1: 8 highest R^2 values of correlations between the different parameters

parameter combination		R^2
$\|\Delta\theta_{850}\|$	and $\|\Delta\theta_{e850}\|$	0.753
Q_{int}	and θ_{e850}	0.690
$TRAd\theta_{48}$	and $TRAd\theta_{MX}$	0.682
$TRAdP_{48}$	and $TRAdP_{MX}$	0.614
$FGEN_{850}$	and $\|\Delta\theta_{850}\|$	0.585
PV_{up}	and Z_{500}	0.538
$qg\omega_{bot}$	and $qg\omega_{top}$	0.533
$SLHF$	and $SSHF$	0.529

The highest correlation occurs with the parameter pair of $|\Delta\theta_{850}|$ and $|\Delta\theta_{e850}|$. This is not surprising as the only difference between the two parameters is that $|\Delta\theta_{e850}|$ not only considers the gradient in potential temperature θ at 850 hPa, but also the specific humidity in its calculation (cf. Sec: 2.2). The moisture in the atmosphere is also the player which connects the pair with the second highest R^2 value (Q_{int} and θ_{e850}). The specific humidity is used to calculate the integrated water vapor Q_{int}, which explains the R^2 value > 0.6. The two following pairs of parameters capturing the change of pressure and θ along 48-hour-trajectories are also very closely connected. One (e.g. $TRAdP_{MX}$) is calculated from the maximum change of the other (e.g. $TRAdP_{48}$) parameter (cf. Sec: 2.2). The parameter $|\Delta\theta_{850}|$ is used in the frontogenesis function to calculate $FGEN_{850}$ (cf. Sec: 2.2), hence the R^2 value > 0.58.
The parameter pairs discussed so far, all have R^2 close to 0.6 and lager. In addition, the reason for their connection can be deduced directly from their mathematical dependence. The next 3 pairs of parameters in the table cannot be connected by they way they were calculated. Further, they have R^2 values close to 0.5. In contrast to the prior parameter pairs described, the connection through the nature of the physical condition they are intended to capture cannot be demonstrated by a simple mathematical dependence.
The slight correlation of PV_{up} and Z_{500} indicates that increased PV in the upper troposphere within the CIR is related to a trough at upper levels which is captured by the anomaly of the geopotential height at 500 hPa. This relation between the two parameters is well established (Hoskins et al., 1985). Parameters $qg\omega_{bot}$ and $qg\omega_{top}$ both capture the instantaneous vertical motion at 600 hPa. They only differ in locating the energy input to the vertical motion at the pressure level into forcing from below and above 600 hPa. The parameters $qg\omega_{bot}$ and $qg\omega_{top}$ are therefore closely connected. The thermodynamic preconditioning of the troposphere is represented by the latent and sensible heat fluxes ($SLHF$ and $SSHF$). The two parameters are closely related as they are both the result of the temperature differences between the surface and the atmosphere.
In contrast to the 8 parameter pairs with R^2 values > 0.5, 272 of the possible pairs have R^2 values < 0.1. Hence, for 67% percent of the possible parameter combinations, the variation in one parameter explains less than 10% of the variation in the second parameter. For half (47%) of the

possible parameter combinations the R^2 values are even smaller, lying < 0.05. In addition, the 18 parameter pairs listed in Tab: 4.2, have R^2 values of zero. To visualize the difference in correlation compared to the parameter pairs with R^2 values > 0.5, Fig: 4.4 shows an example scatter plot of one of the 18 pairs with R^2 values of zero.
To summarize, the linear correlations of 8 of the parameter pairs, shown in Tab: 4.1, can be explained by the mathematical dependence and the fact that some parameters capture similar physical phenomena. The R^2 values also show the degree of redundancy within the 29 chosen physical parameters. In context of the variance of one parameter explaining the variance in a second parameter, a value of < 0.5 can be considered as a bad fit, as it means that less than 50% of the variation of one variable could be explained by the variation of the second variable (this is the case for 98% of the parameter pairs). Despite the fact that some of the parameters (2%) have mathematical dependence and more than one parameter aims to capture one specific physical phenomena, the majority of the parameters (67%) are mostly uncorrelated. Hence, the redundancy in the selected 29 physical parameters is limited.

Table 4.2: 18 parameter pairs with R^2 values of zero

Q_{int}	and $CAPE$	$VELJET$	and θ_{e850}
$FGEN_{850}$	and PV_{up}	$VELJET$	and DEF
$FGEN_{850}$	and SKT	N^2_{TROPO}	and Q_{int}
$UPTTIM$	and $EADY_{up}$	$TRAdP_{48}$	and $EADY_{up}$
$UPTTIM$	and SKT	$TRAdP_{48}$	and $EADY$
$TRAd\theta_{48}$	and Q_{int}	$qg\omega_{bot}$	and SKT
$TRAd\theta_{48}$	and θ_{e850}	$qg\omega_{bot}$	$SLHF$
$TRAd\theta_{MX}$	and SKT	$TRAd\theta_{MX}$	and $VELJET$
$VELJET$	and Q_{int}	Z_{ANOM}	and $SSHF$

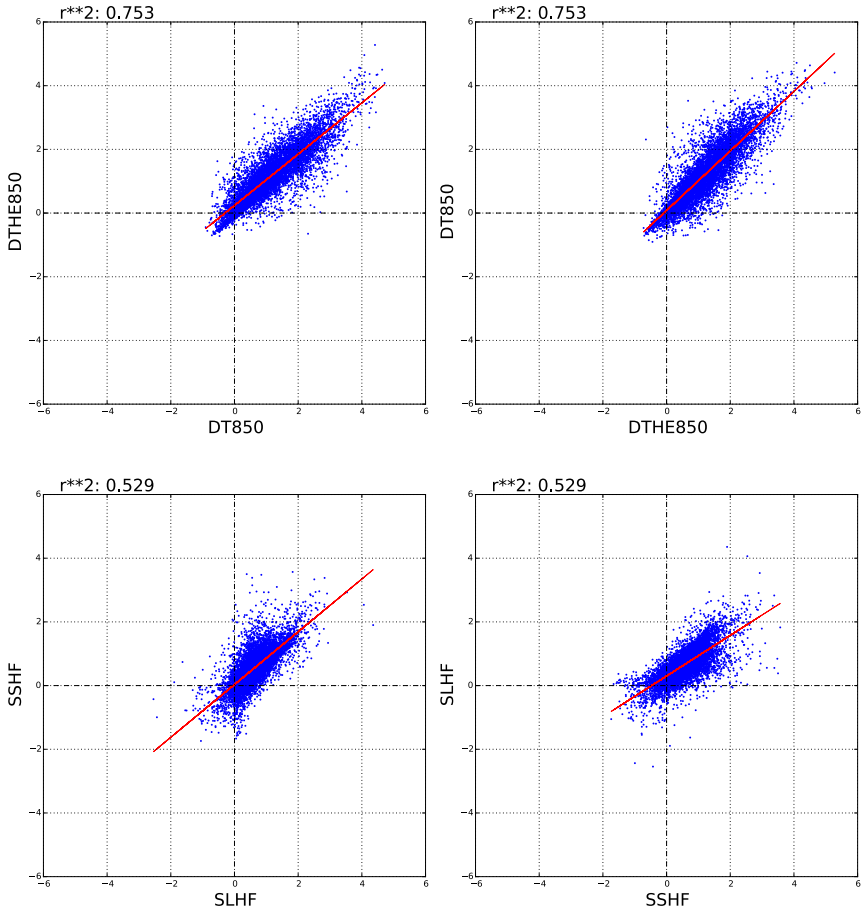

Figure 4.3: Linear correlation: parameter pairs with the highest and the lowest R^2 values from Tab: 4.1

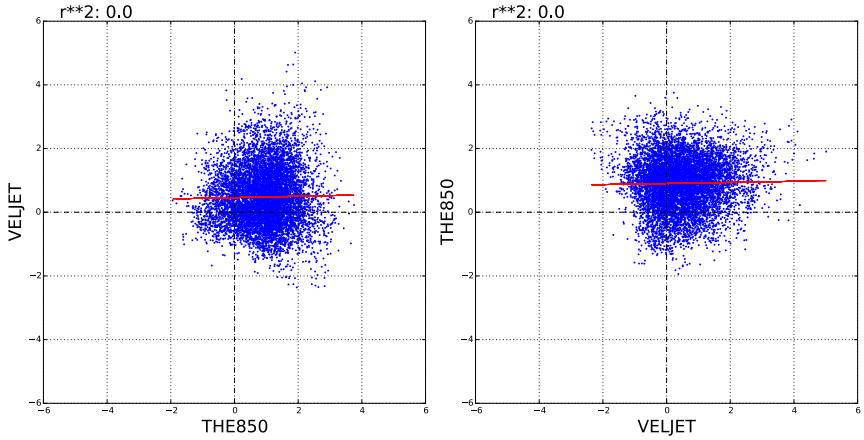

Figure 4.4: Linear correlation: example parameter pair with R^2 value of zero from Tab: 4.2

4.2 Classification based on PCA

This section illustrates the application of a PCA and subsequent varimax rotation (cf. Sec: 2) on the point cloud of all cases in the 29-dimensional parameter space. A step-by-step description offers insight into the application and the basis for the final determination of the classes.

4.2.1 PCA of parameters

The principal components resulting from the PCA show decreasing amounts of explained variance from pc1-pc29 (cf. Fig: 4.5). The first two principal components explain 48.21% of the variance within the data set, together with the 3^{rd} and 4^{th} principal component they comprise 64.97% of the information contained in the data (cf. Tab: 4.4). As noted in Chap: 2 principal components are uncorrelated. Table 4.3 shows the covariance matrix of the first 4 principal components. The principal components show no covariance between each other. The diagonal contains the covariance of each of the 4 principal components with itself, it represents the explained variance along each of the 4 principal components.

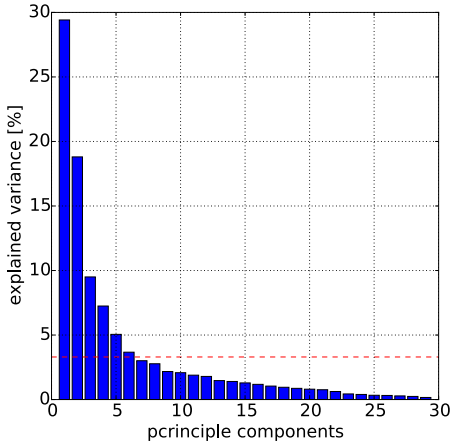

Figure 4.5: Explained variance by each of the principal components, pc1-29.

Table 4.3: Covariance matrix of the first 4 principal components

	pc1	**pc2**	**pc3**	**pc4**
pc1	5.9685	-0.0000	-0.0000	-0.0000
pc2	-0.0000	3.8154	-0.0000	0.0000
pc3	-0.0000	-0.0000	1.9282	-0.0000
pc4	-0.0000	0.0000	-0.0000	1.4709

Table 4.4: Explained variance for the first 4 principal components [%]

prin. comp.	**expl. var. [%]**
pc1	29.42
pc2	18.80
pc3	9.50
pc4	7.25
pc1−pc4	64.97

The biplot in Fig: 4.6, in which the data is projected onto the 2 first principal components, represents almost 50% of the information which is contained in the whole data set. The labeled vectors show in which direction the values of the different parameters vary within the cyclone intensification events. The physical interpretation of the biplot is a challenge due to the great amount of medium length vectors for many of the parameters, and their orientation in many different directions. The parameters of which the vectors are neither short nor long inhibit a clear definition of variation in parameter values. If the parameters each vary along either of the two main axis, a clear split of the 2-dimensional space can be deduced. This facilitates defining classes based on objective indicators for specific physical conditions in the atmosphere during the phase of maximum intensification of extratropical cyclones, which are reasonable from a physical point of view. In Fig: 4.6, however, the vectors of the different physical parameters point into a large range of different directions. Hence, unlike in the work of Graf (2014), an objective and physically reasonable choice of class borders within this 2-dimensional projection purely based on the PCA, is not feasable. In contrast to Graf's (2014) work, this choice does not lead to classes with physically reasonable characteristics. As a result a varimax rotation is applied to determine a 2-dimensional space, based on which reasonable classes can be defined.

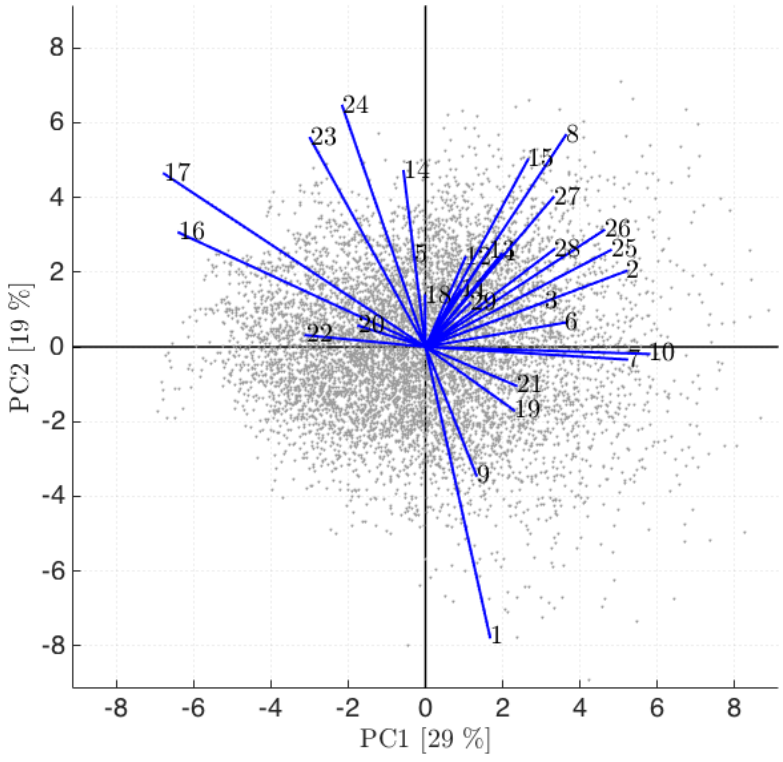

#	parameter
1	PV_{up}
2	PV_{low}
3	$EADY$
4	$EADY_{up}$
5	N^2_{TROPO}
6	$FGEN_{850}$
7	DEF
8	Q_{int}
9	$CAPE$
10	RR_{6h}
11	SKT
12	$SLHF$
13	$SSHF$
14	$\Delta\theta_{SKT700}$
15	T_{PERT}
16	$qg\omega_{bot}$
17	$qg\omega_{top}$
18	$UPTTIM$
19	$TRAd\theta_{48}$
20	$TRAdP_{48}$
21	$TRAd\theta_{MX}$
22	$TRAdP_{MX}$
23	Z_{ANOM}
24	Z_{500}
25	$\lvert\Delta\theta_{850}\rvert$
26	$\lvert\Delta\theta_{e850}\rvert$
27	θ_{e850}
28	T_{ADV850}
29	$VELJET$

Figure 4.6: Biplot based on PCA: With first (second) principal component from PCA (cf. Sec: 2.4) in horizontal (vertical) direction including the explained variance along the axes. The grey points represent the scores of the events in the principal component space. The blue vectors represent the coefficients for each parameter of PC1 and PC2. They show in which direction each parameter varies within the events in this projection.

4.2.2 Varimax rotation

As explained in Chap: 2 a varimax rotation is an operator which achieves the coefficient values to be close to either 0 or 1, while keeping the vectors orthogonal (resulting in either short or long parameter vectors in this case). The varimax algorithm can be applied to any selection of the principal components. As a result, the axes which are rotated have covariance.
The explained variance and the physical reason are the two key aspects to be considered in the choice of the number of principal components to be selected for rotation. It is reasonable to neglect principal components which explain small amounts of the variance within the data set, when looking at the output from a PCA, as they contain very little information (cf. Sec: 2 and Abdi (2003)). Hence, considering the decrease of variance explained by the principal components (cf. Fig: 4.5), rotating any more than the first few principal components does not increase the retained information significantly. In addition, all selected principal components are treated as equal in the rotation. Hence, an increasing amount of principal components in the selection may lead to decreasing explained variance along the new components after rotation. Performing rotations with increasing amounts of selected principal components, and viewing the biplots, helps to understand which projection is most reasonable form a physical point of view. The orientation and length of the parameter vectors visualized in a biplot allows the trends of the forcings for cyclone intensification to be assessed.
The subplots in Fig: 4.7 show how the direction and length of the parameter vectors change, depending on the selection of principal components on which the varimax rotation is applied. An abstract interpretation of what is displayed in Fig: 4.7 can be summarized as follows. Selecting only the 1^{st} principal component (pc1) for the rotation leads to no change at all. Applying the varimax operator on the first two principal components (pc1-pc2) results in a slight counter-clockwise rotation of the new components (cx.1 and cx.2). Including the 3^{rd} principal component (pc3) in the selection of rotated axes shows a change in length and in direction of the parameter vectors. Increasing the number of selected principal components which are rotated, by the 4^{th} principal component (pc4) further bundles the parameter vectors even more around the two new component axes (c4.1 and c4.2).

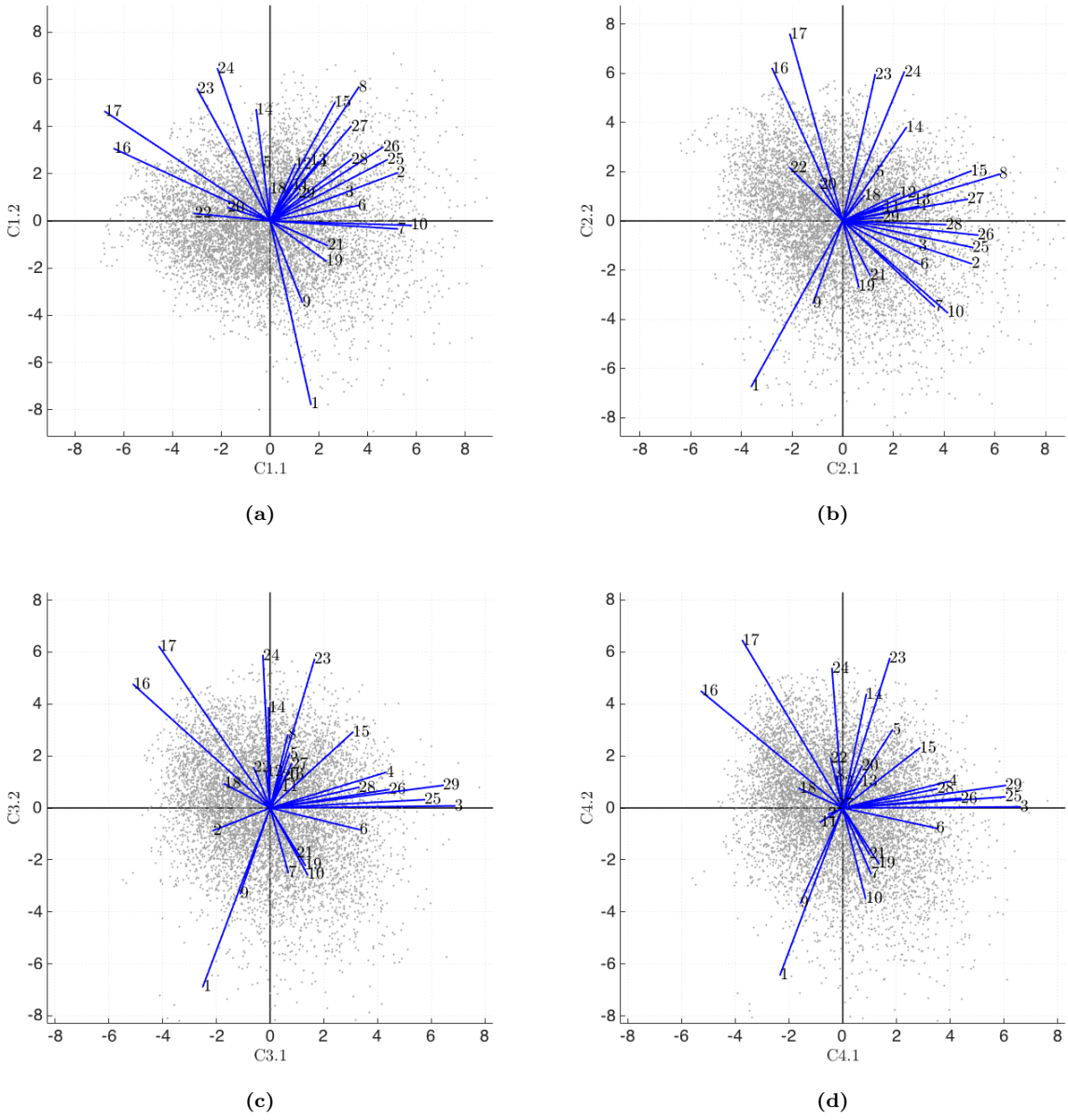

(a) **(b)** **(c)** **(d)**

Figure 4.7: Varimax rotation applied on: a) the 1^{st} principal component ($pc1$), **b)** the 1^{st} and 2^{nd} principal components ($pc1-pc2$), **c)** the 1^{st} to 3^{rd} principal components ($pc1-pc3$), **d)** the 1^{st} to 4^{th} principal components ($pc1-pc4$). With first (second) new component from the varimax rotation (cf. Sec: 2.4) in horizontal (vertical) direction, here labeled as cx.1 and cx.2, where x represents the number of principal components selected for the varimax rotation. The numbers labeling the blue vectors correspond to the 29 different parameters, see Fig: 4.6 for details.

The objective of the varimax rotation is best achieved after applying it to the first 4 principal components from the PCA. This is illustrated by visualizing the first 2 new components (C1 and C2), which combine the greatest explained variance (cf. Tab: 4.7), in a biplot (cf. Fig: 4.7d). First, the amount of medium length parameter vectors has decreased significantly, while more vectors are either short or long indicating small or large variation of values in the chosen 2 dimensions. Second, apart from the parameters indicating vertical motion ($qg\omega_{bot}$ and $qg\omega_{top}$), the parameters, which vary strongly, each vary in the direction of either of the two main axis. Hence, a clear split of the 2-dimensional space can be performed. This allows classes to be defined based on objective indicators for specific physical conditions in the atmosphere during the phase of maximum intensification of ETCs.

Table 4.5: Covariance matrix of the first 4 rotated components

	c1	**c2**	**c3**	**c4**
c1	3.5222	-0.8881	1.0510	1.3408
c2	-0.8881	4.3201	-0.6506	-0.1357
c3	1.0510	-0.6506	2.4890	1.0953
c4	1.3408	-0.1357	1.0953	2.8516

Table 4.6: Correlation coefficients (R^2) for the first 4 rotated components

	c1	**c2**	**c3**	**c4**
c1	1.0000	0.0518	0.1260	0.1790
c2	0.0518	1.0000	0.0394	0.0015
c3	0.1260	0.0394	1.0000	0.1690
c4	0.1790	0.0015	0.1690	1.0000

Table 4.7: Explained vatriance for the first 4 rotated components [%]

rot. comp.	**expl. var.** [%]
c1	17.36
c2	21.29
c3	12.27
c4	14.05
c1−c4	64.97

Together the new 4 rotated components still explain 65% of the variance within the data set (cf. Tab: 4.7). As a result of the rotation, the 4 new rotated components have non-zero covariance, as shown in Tab: 4.5. As can be seen in Tab: 4.6, the strongest correlation occurs between the 1^{st} and the 4^{th} rotated component. With an R^2 value of 0.18 this correlation is however very small. The first two new components which are used as the axes of the biplot explain 38.65% of the variance within the data set. From the original biplot with the principal components from the PCA as axes this is a decrease of 10% explained variance when choosing this new rotated perspective. A 10% decrease in explained variance can be regarded as acceptable, because it has to be seen with regard to the more physically meaningful definition of the axes.
Figure 4.8 shows the biplot with the first and second new component after applying the varimax operator on the first 4 principal components (cf. Fig: 4.7d), in greater detail. From this figure it is possible to determine the physical characteristics of the 1^{st} and 2^{nd} new component. The 1^{st} new component lies within the bundle of long vectors (strong variation of values) of the parameters

$|\Delta\theta_{850}|$, $|\Delta\theta_{e850}|$, $EADY$, $EADY_{up}$, and $VELJET$ which are all indicators for a baroclinic environment. The 2^{nd} new component is oriented in direction along which the parameters Z_{ANOM}, Z_{500}, $\Delta\theta_{SKT700}$, $CAPE$, and PV_{up}, vary. These parameters can be summarized to play a key role in tropospheric instability and the upper-level forcing of cyclone intensification. The two long parameter vectors of $qg\omega_{bot}$, $qg\omega_{top}$ are positioned at an angle of approximately 45° to both new component axes (c1 and c2). The orientation of these two parameters demonstrates that tropospheric instability and upper-level forcing, as well as low- to mid-level baroclinicity, have an equally great impact on vertical motion in the mid-troposphere (600 hPa), if both forcings (low- to mid-level baroclinicity and tropospheric instability & upper-level forcing) are high, the vertical motion increases. The $qg\omega_{bot}$ is oriented closer to the 1^{st} new component, hence it correlates slightly more with low- to mid-level baroclinicity. In contrast, the $qg\omega_{top}$ is oriented closer to the 2^{nd} new component, and therefore correlates slightly more with tropospheric instability and upper-level forcing.

Baroclinicity as well as upper level forcing, from upper level flow, occurring troughs/ridges, and anomalies in upper level PV are well established drivers of cyclone intensification (cf. Sec: 1.2.3). Hence, from a physical point of view the application of the varimax rotation on the first 4 principal components results in a reasonable 2-dimensional perspective of the multidimensional space.

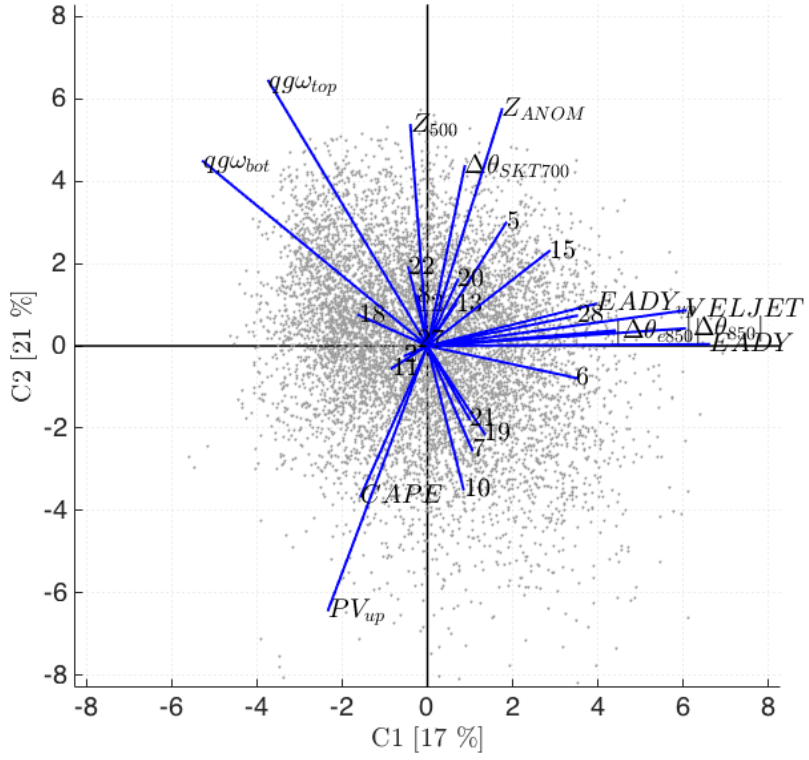

#	parameter
2	PV_{low}
5	N^2_{TROPO}
6	$FGEN_{850}$
7	DEF
8	Q_{int}
10	RR_{6h}
11	SKT
12	$SLHF$
13	$SSHF$
15	T_{PERT}
18	$UPTTIM$
19	$TRAd\theta_{48}$
20	$TRAdP_{48}$
21	$TRAd\theta_{MX}$
22	$TRAdP_{MX}$
27	θ_{e850}
28	T_{ADV850}

Figure 4.8: Biplot based on varimax rotation: With first (second) new component from varimax rotation (cf. Sec: 2.4) in horizontal (vertical) direction including the explained variance along the axes. The grey points represent the scores of the events in the rotated component space. The blue vectors represent the coefficients for each parameter of C1 and C2. They show in which direction each parameter varies within the events in this projection.

4.2.3 Classes

The classes are determined as described in Sec: 2.5 (cf. Fig: 4.9). The lower left quadrant is defined as class 1, the lower right quadrant as class 2, the upper left quadrant as class 3, the upper right quadrant as class 4. Class 5 is defined as a circle centred a the origin with the radius chosen such that 20% of the cases lie within the class. Table 4.8 comprises statistical details of the 5 different classes. Most cases are in class 3 (25.43%) closely followed by class 2 (22.11%), class 1 contains the least amount of cases (15.59%).

Table 4.8: The distribution of cases in each class

Class	Num. Cases	% Cases
1	1318	15.5866
2	1870	22.1145
3	2150	25.4257
4	1427	16.8756
5	1691	19.9976

It is possible to include information about the intensity of each of the cases in the biplot. As mentioned in Sec: 1.1, the intensification of cyclones can be determined by the Bergeron value[1]. The Bergeron value is based on how much the core pressure of a cyclone decreases over time. If a cyclone has a Bergeron value of 1 or more it can be labeled as an explosively intensifying cyclone or a bomb (Sanders and Gyakum, 1980). Here the maximum Bergeron value of each ETC case is determined based on a 24 hour running window, which iterates in 6 hour time steps along the cyclone's life time. PMI lies at the centre of the 24 hours, i.e., it is the mid point of the time period over which the maximum Bergeron value is computed.
Figure 4.10 conveys the same information as Fig: 4.9 with the difference that the cases are each colored based on the maximum Bergeron value which occurred during the corresponding cyclone's phase of maximum intensification. Figure 4.10 also shows the frequency distribution of the maximum Bergeron values along each component axes. For Fig: 4.10 the cases have been summarized in 3 groups of increasing Bergeron values, with a different color to distinguish each group. Most cases have low (< 0.5), some have high ($> 0.5 < 1.5$) and few have very high (> 1.5) Bergeron values. All 3 groups are normally distributed along the vertical axis, with their peaks around 0. This leads to suggest, that variation in mode and degree of the upper-level forcing and tropospheric instability at PMI, does not correlate with the intensity of cyclones. Along the horizontal axis however, cases with low, high and very high Bergeron values are distributed differently depending on their intensity. Cases in each of the 3 groups of Bergeron values are, in themselves, normally distributed. Cases with low Bergeron values have the peak of their frequency distribution on the left of 0. The normal frequency distribution of cases with high Bergeron values lies slightly to the right, and that of cases with very high Bergeron values lies clearly further right of 0. Hence, a trend of increasing Bergeron values (i.e. cyclone intensification) can be observed from left to right along the horizontal component axis. This further highlights the relevance of baroclinicity for cyclone intensification.
It is important to extend on the topic of maximum cyclone intensification and the intensity of the cyclones at PMI. Note that the Bergeron value is based on the change of CCP over 24 hours, while the intensity of a cyclone at PMI (the mid time point of those 24 hours) is represented by the instantaneous values of sea level pressure. The composites in Fig: 4.11 show the average condition of sea level pressure in the 5 classes (the values are calculated as explained in Chap: 5). It can be seen that on average, the cases in class 2 have the highest, and the cases in class 3 have the lowest CCPs at PMI. This indicates that instantaneous tropospheric instability and upper-level forcing, as well as low- to mid-level baroclinicity in combination, have an influence on the sea level pressure

[1] value of 1 Bergeron = (24 hPa day^{-1}) x ($sin\phi/sin60°$), where ϕ is the latitude of the cyclone center (Sanders and Gyakum, 1980)

of the cyclones at PMI. Note the method for defining PMI, means that the instantaneous sea level pressure does not show the lowest CCP which occurs in the cyclones life time. For some cases the sea level pressure at PMI can be close to its absolute minimum, while for other cases it decreases greatly after PMI.
Summarizing, the horizontal axis represents the variation in mid- to low-level baroclinicity, this implies that cases in classes 1 and 3 are located in different extents of baroclinic environments at PMI than cases in classes 2 and 4. The vertical axis is related to upper-level forcing and tropospheric instability. This indicates cases in classes 1 and 2 differ in type and/or degree, of upper-level forcing and tropospheric instability, from cases in classes 3 and 4. The strength of the baroclinic environment at PMI further plays a key role for the intensification of cyclones (cf. gradient of maximum Bergeron values). The strong gradient of cyclone intensification along the horizontal axis C1 (based on the maximum Bergeron values), is not mirrored in the intensities at PMI (based on average sea level pressure). The absolute average intensity of ETC at PMI of each class gives no clear indication, for the speed of intensification of the cases in the class. It is further important not to mistake the sea level pressure at PMI with the maximum intensity the cyclones reach, as the pressure decrease post PMI varies from case to case.

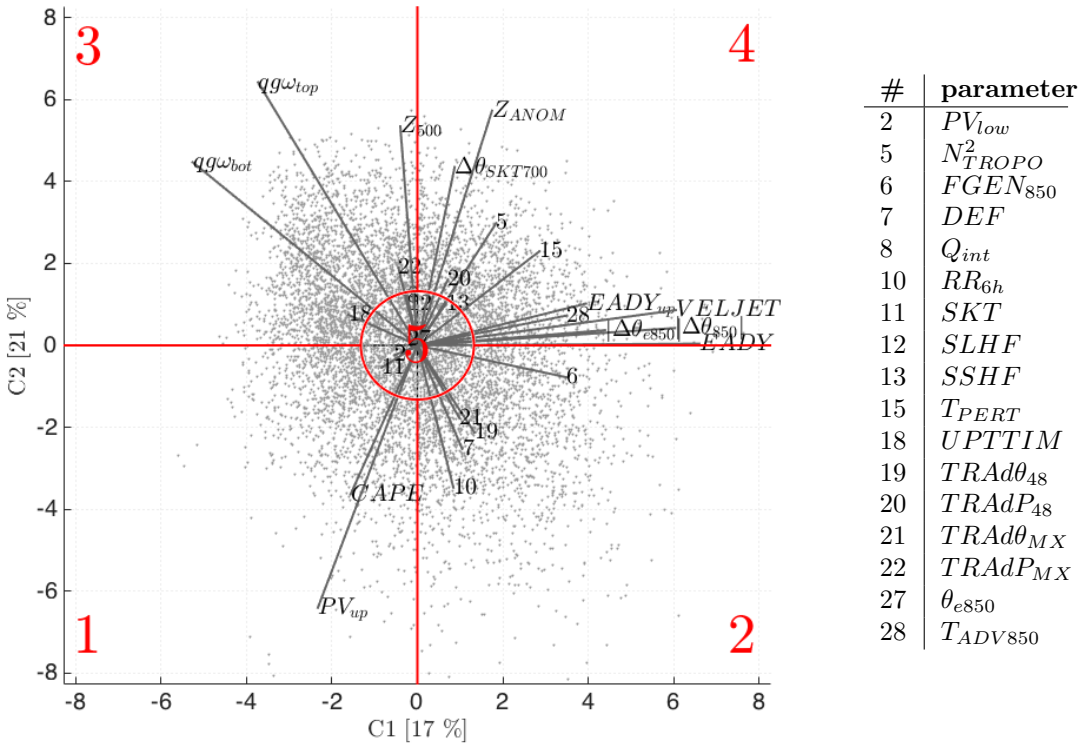

#	parameter
2	PV_{low}
5	N^2_{TROPO}
6	$FGEN_{850}$
7	DEF
8	Q_{int}
10	RR_{6h}
11	SKT
12	$SLHF$
13	$SSHF$
15	T_{PERT}
18	$UPTTIM$
19	$TRAd\theta_{48}$
20	$TRAdP_{48}$
21	$TRAd\theta_{MX}$
22	$TRAdP_{MX}$
27	θ_{e850}
28	T_{ADV850}

Figure 4.9: Biplot based on varimax rotation: As in Fig: 4.8, but the red lines mark the class borders and the red numbers label them 1-5.

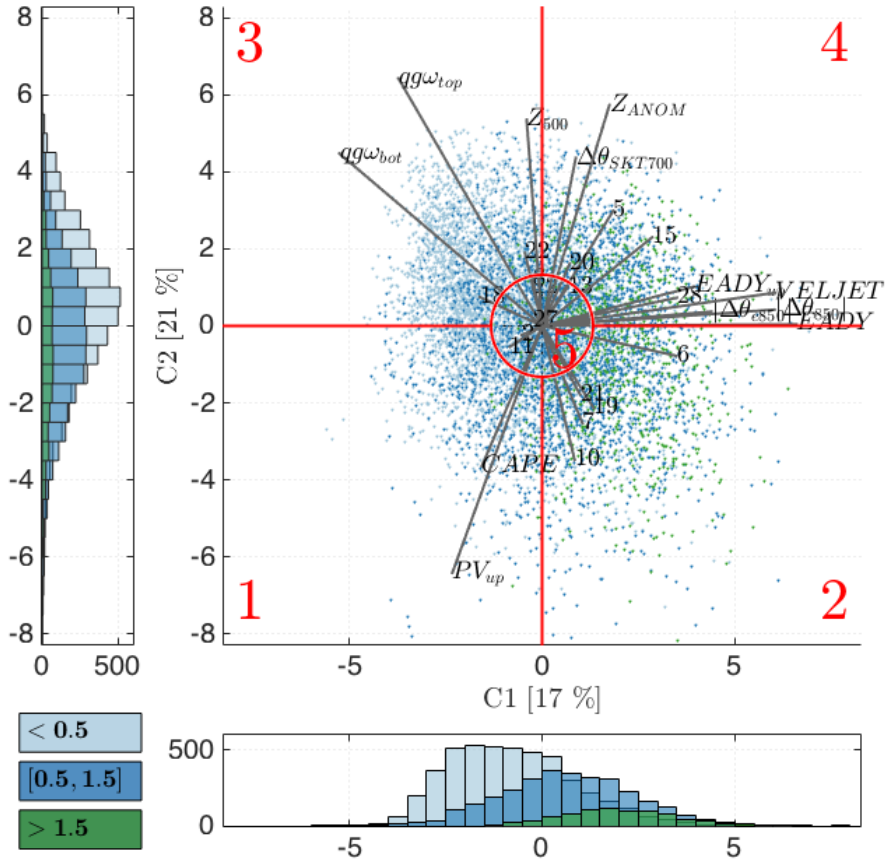

#	parameter
2	PV_{low}
5	N^2_{TROPO}
6	$FGEN_{850}$
7	DEF
8	Q_{int}
10	RR_{6h}
11	SKT
12	$SLHF$
13	$SSHF$
15	T_{PERT}
18	$UPTTIM$
19	$TRAd\theta_{48}$
20	$TRAdP_{48}$
21	$TRAd\theta_{MX}$
22	$TRAdP_{MX}$
27	θ_{e850}
28	T_{ADV850}

Figure 4.10: Biplot based on varimax rotation: As in Fig: 4.9 but the colors of the points correspond to the maximum Bergeron value of each case. The histograms at the left and bottom show the distributions of the points by color.

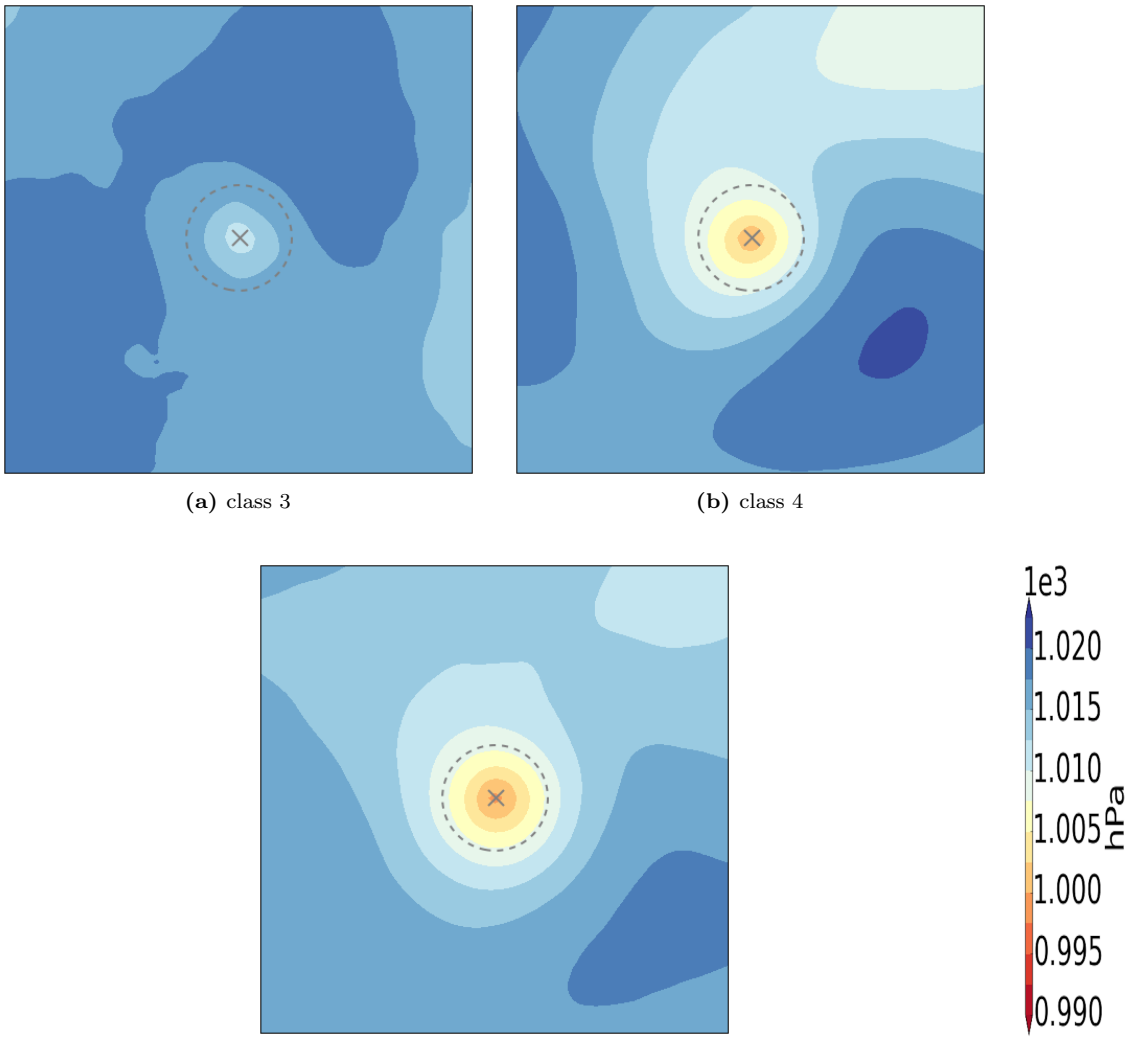

(a) class 3 **(b)** class 4

(c) class 5

(d) class 1 **(e)** class 2

Figure 4.11: *SLP*

Chapter 5

Characterization of Classes

The biplot of Chap: 4 and the classes determined within it are the basis of this chapter, it is therefore repeated in Fig: 5.1. The 5 different classes are characterized based on composites of a selection of 8 parameters. Those parameters that vary strongly along the horizontal and vertical axis of the biplot are used for the characterization of the classes. For completeness, composites of all parameters are shown individually in separate figures in App: D.
In order to determine the physical characteristics of the classes, spatial averages are calculated for every parameter, of all cases in each class, at every grid point surrounding the PMI. The meteorological field is centered around the core of the cyclone at PMI and the convergence of the meridians towards the poles are taken into account in the calculation of the composites. Subsequently the cyclone domain of $\pm 20°$ in zonal and meridional direction is cut out (approx. 4000 km total side length).
The values in the composite figures show averages of the physical parameter values A, not the normalized values A_{norm} (cf. Sec: 2.3). This facilitates the interpretation of the composite figures and hence the understanding of the physical condition of the atmosphere at PMI for the 5 different classes. Note, the following description is based on a limited amount of parameters, of the total set of 29 parameters used for the classification. Furthermore it is based on the composites, hence it refers to the average conditions over all cases in a specific class. The composites of the classes $(1-4)$ are oriented based on their location in the biplot, while the composites for class 5 are shown separately.
This chapter is divided into 2 sections. First, the physical characteristics of class 5 are described based on figure 5.2. Second, an overview of the composites of classes 1 to 4 is given by discussing figures 5.3, 5.4, 5.5, and 5.6, allowing a comparison between those classes. Both sections close with a summary of the key distinctions of the discussed classes.
One page is intentionally left blank to make it easier to simultaneously read the text and view the respective diagram in booklet format.

This page is intentionally left blank.

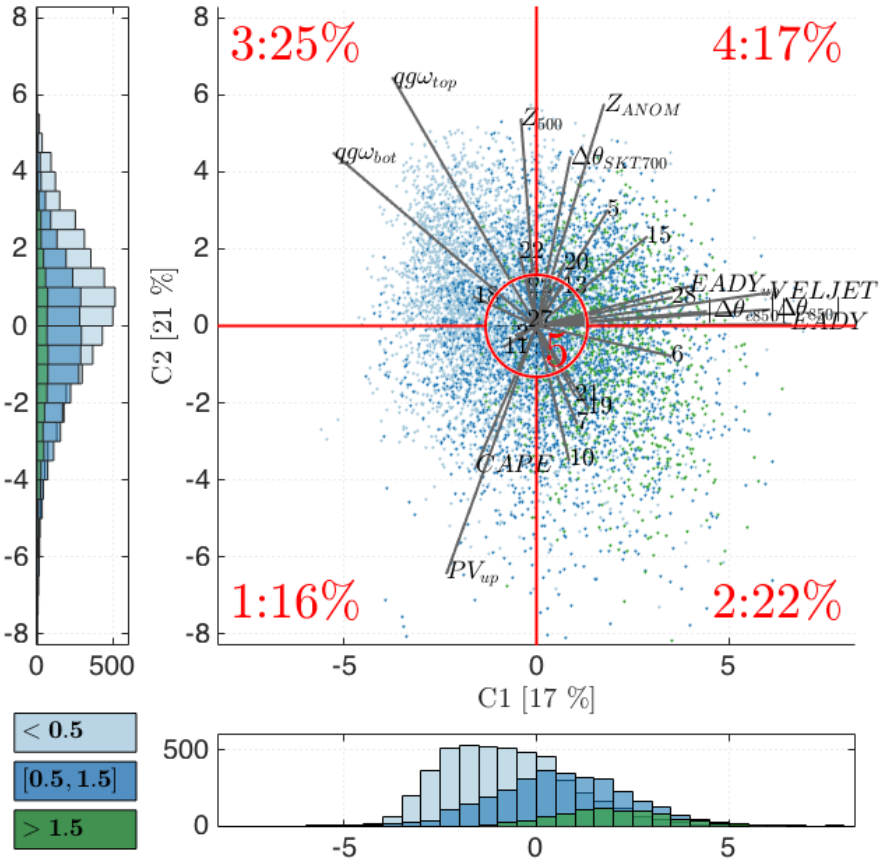

Figure 5.1: Biplot based on varimax rotation: As in Fig: 4.10 but the numbers in percentage behind the class number state the proportion of caseses in the class.

5.1 Characterizing Class 5

Lying in the centre of the biplot this class shows average characteristics from the 4 surrounding classes. Therefore it differs a little bit from the other 4 classes, but shows no major difference to any of them. The patterns in the composites of this class do not show any of the lowest or highest values. Class 5 can hence be considered as a class with average characteristics of cyclones at PMI.
The subplots in Fig: 5.2 show the composites of the 8 parameters computed for class 5. A north-south gradient of PV_{up} depicts the increase of the Coriolis parameter towards the pole in Fig: 5.2a. This gradient is perturbed close to the middle of the cyclone domain. The cyclone centre is hence located downstream (right) of a trough-like positive upper-level PV anomaly, and upstream (left) of a PV ridge. The CIR encompasses the gradient of PV, largely lying ahead of the highest values of PV_{up}. The PV trough is positioned in a north-south orientation and shows indications for cut-off building (cf. region with highest PV_{up} values, dark blue spot). The values of $qg\omega_{top}$ are low within most of the CIR, with a local minimum exactly above the cyclone centre. This represents the vertical lifting expected to be induced by the positive upper-level PV anomaly. The vertical motion leads to a decrease in pressure and thus to cyclone intensification. A very small area of low positive values of $qg\omega_{top}$ are visible upstream (left) the PV anomaly, representing related weak downward vertical movement.
The wind velocities of $VELJET$ have their maximum ($> 42.5\ m/s$) in a small area south-west of the CIR, representing a jet-streak. Low wind velocities ($< 30\ m/s$) clearly reflect the shape of the gradient of PV_{up}. Hence, a wind gradient can be observed within the CIR. The cyclone centre is located in the left exit region of the jet streak (cf. Fig: 5.2b). Thus, it can be suspected that on average, the jet and the ageostrophic circulation associated with it, e.g., upward vertical motion in the left exit, play a part in the intensification of ECTs. The parameter $|\Delta\theta_{e850}|$ shows that the gradient of θ_e at 850 hPa is highest in the CIR, close to the cyclone centre, just north-west of it (cf. Fig: 5.2b). The strength of the gradient indicates that cyclones are positioned in a low-level baroclinic zone. This leads to suggest an interaction of the upper-level trough with the lower-level baroclinic zone, relieving baroclinic instability.
The baroclinic instability is represented by the Eady growth rate $EADY$, which is based on the vertical stability and the vertical gradient of horizontal wind (cf. Fig: 5.2c). The highest values of $EADY$ occur north of the cyclone centre. Note, the $EADY$ parameter is calculated as an average value between 850 and 500 hPa and the cyclone centre is determined at sea level. Hence a tilt in the cyclone core with height explains the offset of the area shown to have the highest baroclinic instability and the location of the cyclone centre. Values of $qg\omega_{bot}$ are low within the cyclone domain with a local minimum north-east of the cyclone centre. Additionally to $qg\omega_{top}$ which represents the upper-level forcing (between 600 and 500 hPa) on vertical updraft at 600 hPa, low-level forcing $qg\omega_{bot}$ (between 650 and 600 hPa) also plays a role for ETCs in this class. Note the values and steps are the same in $qg\omega_{top}$ and $qg\omega_{bot}$, hence $qg\omega_{bot}$ indicates a weaker low-level forcing on the updraft, compared to the upper-level forcing. Both $qg\omega_{top}$ and $qg\omega_{bot}$ represent vertical updraft related to the left exit region of the jet, at 600 hPa.
The convective potential of the air ($CAPE$) within the cyclone domain is displayed in Fig: 5.2d. The north-south gradient of $CAPE$ reflects the climatological background gradient in temperature and moisture. A tongue of high values of $CAPE$ extends northward into the centre of the cyclone domain, a region with lower values. The result is a strong gradient of $CAPE$ in the CIR, and varying values of $CAPE$ in the CIR. High absolute values of $CAPE$ occur close to the centre of the cyclone, in the warm sector. This indicates high convective potential, which emphasizes the instability in the environment in the CIR. Furthermore, RR_{6h} shows values of $1 - 5\ mm$ of 6-hour accumulated precipitation within the CIR. Together with high values of $CAPE$ and $|\Delta\theta_{e850}|$ extending northward into the CIR, the precipitation could be partially attributed to convective activity in a baroclinic zone.
In summary the intensification of ETCs in **class 5** is related to upper-level forcing by an upper-level PV trough and a medium-strength jet-streak. Occurring at a moderate level throughout the troposphere, vertical updraft at 600 hPa is related to upper- and lower-level forcing ($qg\omega_{top}$ and $qg\omega_{bot}$), with grater values in the upper-levels. Furthermore, baroclinic instability and the

convective potential, is high close to the centre of the cyclone.
Based on the borders drawn in the biplot, class 5 contains 20% of all ETCs events which aver contained in the data set. The ETCs in this class show varying Bergeron values (cf. Fig: 5.1), some of them experience very slow pressure drops resulting in small Bergeron values while others experience explosive intensification. The composite of sea level pressure displayed in Fig: 4.11 shows that the sea level pressure of the ETCs in class 5 is "average" at PMI, compared to the 4 surrounding classes, indicating medium intensity.

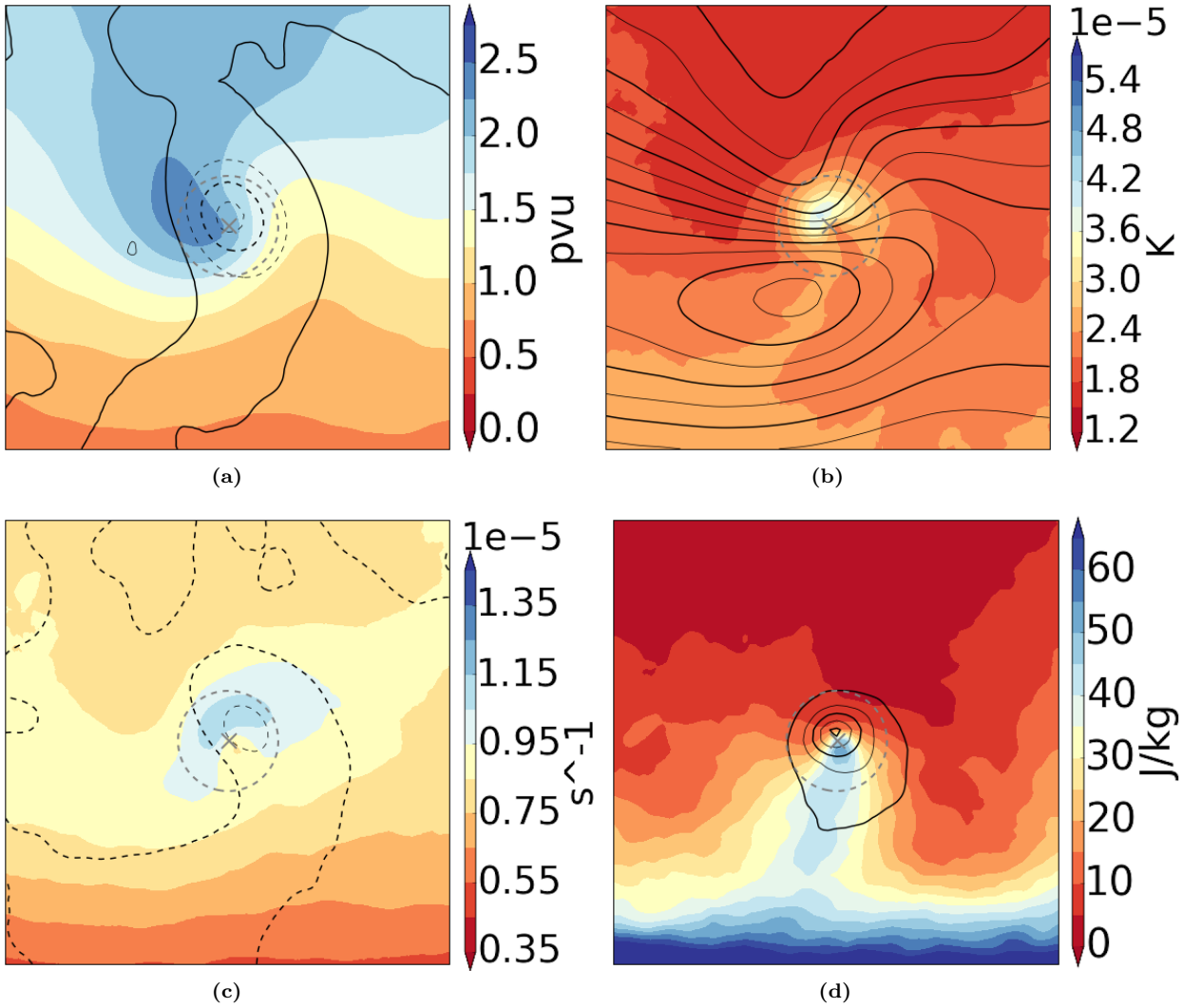

Figure 5.2: Composites of Class 5: a) PV_{up} (filled contours) and $qg\omega_{top}$ (black contours) **b)** $|\Delta\theta_{e850}|$ (filled contours) and $VELJET$ (black contours) **c)** $EADY$ (filled contours) and $qg\omega_{bot}$ (black contours) **d)** $CAPE$ (filled contours) and RR_{6h} (black contours). The color range of the composites is qualitatively similar for all the different parameters, where red indicates low values and blue indicates high values. For details on the units, and steps in the black contours, see the composites in appendix D.

5.2 Characterizing Classes 1 to 4

5.2.1 PV_{up} and $qg\omega top$

Composites of PV_{up} and $qg\omega top$ for classes 1 to 4 are displayed in Fig: 5.3. **Class 3** shows the expected north-south gradient of upper-level PV (PV_{up}) the perturbation at the centre is however much weaker than the trough observed in class 5. In addition, $qg\omega top$ does not show a pattern indicating localized vertical motion close to the cyclone centre or CIR, or any where else in the cyclone domain. Hence, upper-level forcing is weak in the events grouped into this class.
The composites of **class 4** show a wave-like structure with a strong gradient of PV_{up} within the CIR, which looks like an upper-level trough in its early phase. The values of $qg\omega top$ have a local minimum in the north-west sector of the CIR, ahead of the positive PV_{up} anomaly. This indicates updraft and cyclone intensification. Corresponding descending air masses are visible upstream (left) of the wave structure in PV_{up}.
For **class 1** the composites display a different picture: the PV_{up} anomaly has cutoff-like characteristics with closed contours of high positive values of PV at the centre, which are not connected by equally high values to the underlying north-south gradient in PV_{up}. The cyclone centre is located slightly north of the highest PV values. The CIR greatly overlaps with the cutoff structure encompassing the high PV values. The vertical upward motion represented by negative $qg\omega top$ values is stronger than in class 4. The corresponding vertical downward motion upstream (left) of the PV-cutoff is also more intense.
The composites of **class 2** show a developed upper-level trough (PV_{up}) with high PV values and a very strong gradient of PV on its east side. The CIR is located exactly on the gradient also encompassing much of the highest PV values. In addition, the values of $qg\omega top$ vary strongly within the cyclone domain. Very low values, indicating very strong updraft, are located ahead of the southwest tip of the trough, with the minimum lying exactly at the location of the cyclone centre. The region experiencing the corresponding downdraft lies upstream of the trough. The $qg\omega top$ has the highest and lowest values in this class. Strong upper-level forcing and vertical movement plays a major role in class 2.

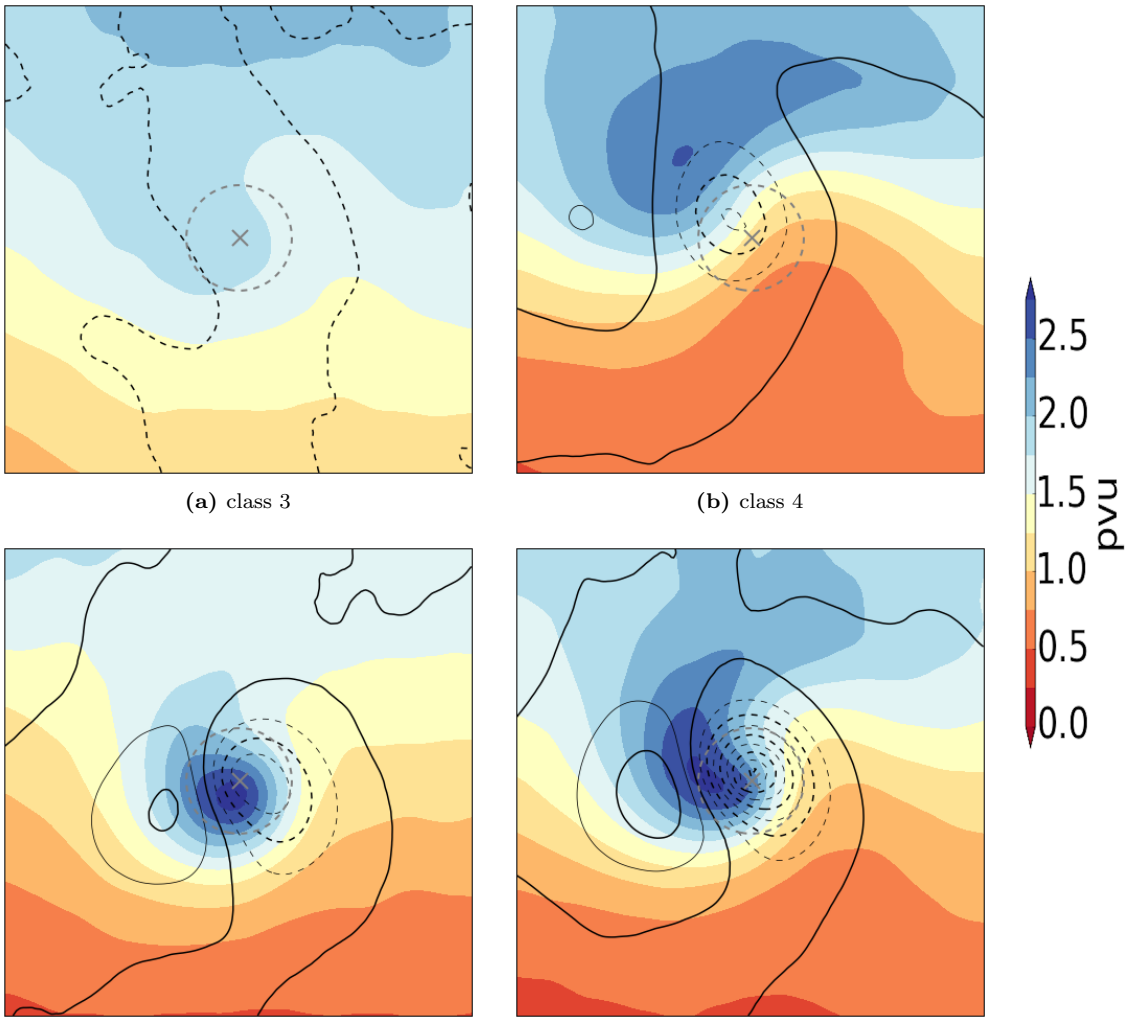

(a) class 3 **(b)** class 4

(c) class 1 **(d)** class 2

Figure 5.3: Composites of classes 1 to 4: PV_{up} (filled contours) and $qg\omega_{top}$ (black contours). Same as for Fig: 5.2a, but here shown for classes 1-4. PV_{up} in PVU (filled contours) and $qg\omega_{top}$ (black contours) in steps of $2 \cdot 10^{-2}$ Pas^{-1} (range 0.01 and -0.02), full lines mark positive values (descent), dashed lines mark negative values (ascent).

5.2.2 $|\Delta\theta_{e850}|$ and $VELJET$

In the composites of **class 3** weak north-south gradients of both, $|\Delta\theta_{e850}|$ and $VELJET$ can be observed. This indicates a weak baroclinicity throughout the whole troposphere.
The composites of **class 1** also display low values of $|\Delta\theta_{e850}|$ and $VELJET$ within the CIR. The $|\Delta\theta_{e850}|$ shows a curled up structure (counter clockwise) of medium values around the cyclone centre, indicating curled up bent-back fronts. A small area with high wind velocities is located south of the cyclone centre and the CIR. The distance to the small jet streak and its non-bent structure lead to suggest that the cyclone location relative to the jet streak and the associated ageostrophic circulation has a small impact on the vertical motion within the CIR.
In **class 4** the cyclone centre at sea level is located below a long jet streak. The jet streak is oriented zonally with a northward bend starting at the longitude along which the cyclone centre is positioned. Most of the CIR also encompasses high wind velocities. The location of the updraft discussed when analyzing $qg\omega top$ correlates with the gradient in wind velocity ($VELJET$) and PV_{up} north-west of the cyclone centre. A broad strand of medium high values of $|\Delta\theta_{e850}|$ starts in the south-west corner of the cyclone domain, it thinnens and extends its tip into the CIR. North-west, close to the cyclone centre is where the values of $|\Delta\theta_{e850}|$ reach the highest values. The cyclone centre is thus positioned at the tip of a large baroclinic zone (likely a cold front) and just south of the strongest low-level baroclinicity.
In **class 2** a similar strand (compared to class 4) of medium to high values of $|\Delta\theta_{e850}|$ extends into the CIR with the highest values positioned on the north-west side of the cyclone centre. The strand is slimmer, starts further east, and has higher values compared to the strand observed in class 4. High values of $VELJET$ are located south-west of the cyclone centre. This positions the cyclone in the left exit region of the jet streak, which is a region known to be related to strong updraft and cyclone intensification.
The differentiation between the values of these two sets of composites between class 1 and class 3 versus class 2 and class 4 clearly reflects the orientation of the variation of the two parameters (parameter vectors $|\Delta\theta_{e850}|$ and $VELJET$) along the horizontal axes in the biplot.

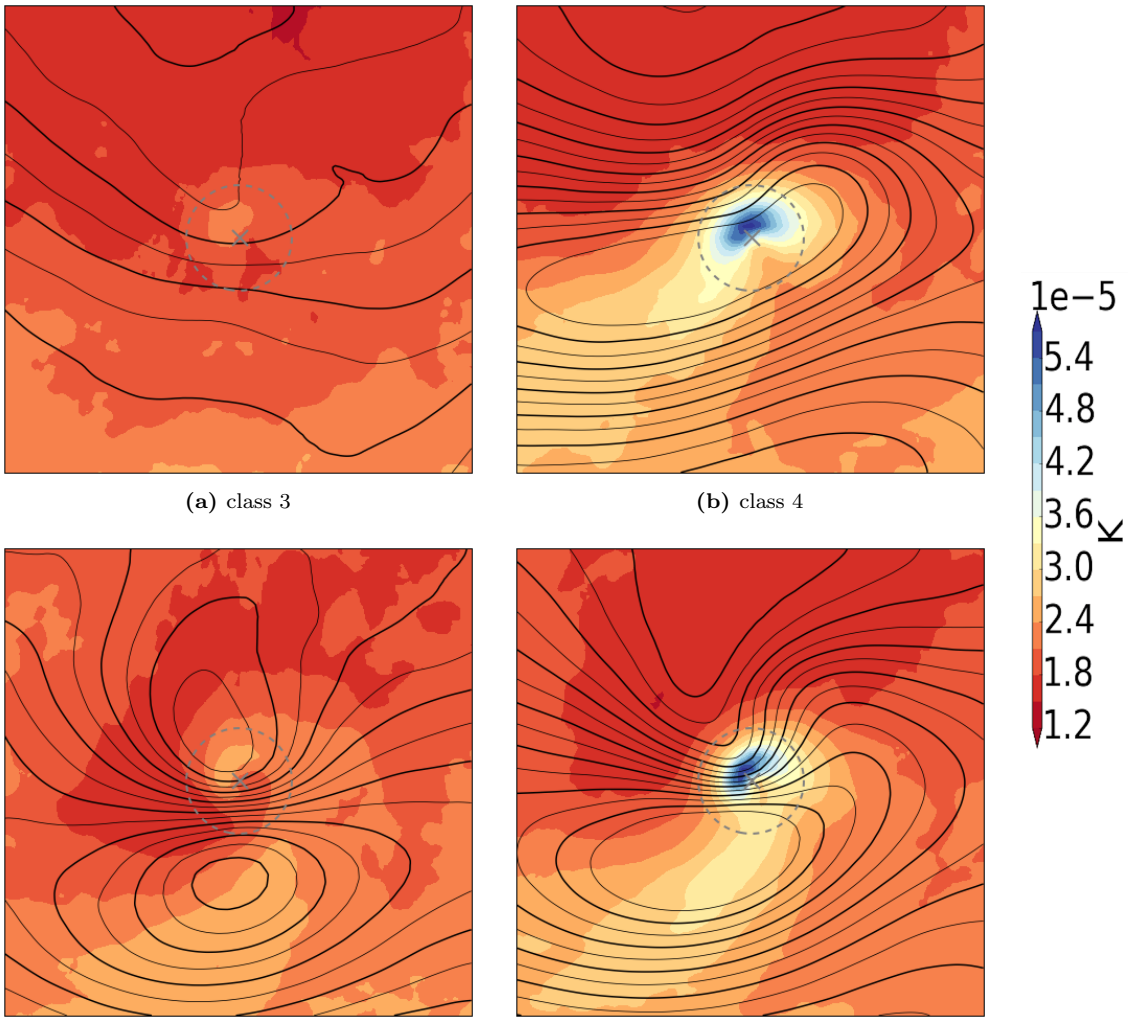

(a) class 3 **(b)** class 4

(c) class 1 **(d)** class 2

Figure 5.4: Composites of classes 1 to 4: $|\Delta\theta_{e850}|$ (filled contours) and $VELJET$ (black contours). Same as for Fig: 5.2b, but here shown for classes 1-4. $|\Delta\theta_{e850}|$ in K (filled contours) and $VELJET$ (black contours) in steps of $2.5m/s$ (range 10 to $50m/s$).

5.2.3 $EADY$ and $qg\omega_{bot}$

The baroclinic zones which were indicated by the $|\Delta\theta_{e850}|$ are represented even better by the Eady growth rate (cf. $EADY$). The low-level baroclinicity shown by $EADY$ is complemented by the vertical motion $qg\omega_{bot}$ with forcing from lower-levels. Similar to those in Fig: 5.4, the composites of the parameters $EADY$ and $qg\omega_{bot}$ in Fig: 5.5 have lower values in classes 1 and 3 than in classes 2 and 4, which is again comparable to the information deduced from the biplot.
In **class 3** medium values of $EADY$, and slightly negative values of $qg\omega_{bot}$, occur throughout the whole cyclone domain.
A north-south gradient of $EADY$ is visible in **class 1** with a distinct area of low values in the CIR and a local minimum at the cyclone centre. The Eady growth rate is small in both, class 1 and class 3. The values of $qg\omega_{bot}$ show a more (compared to class 3) distinct pattern of low values north-east of the cyclone centre but no area with downward motion of air within the cyclone domain (cf. Fig: 5.5a).
In **class 4** the area of high values of $EADY$ is the largest of all classes. The high values are bent around the north side of the cyclone centre extending south on its east and its west side almost extending to the whole of the CIR. This area marks the strongest baroclinicity in the cyclone domain, highlighting the average orientation of the tips of the warm and the cold front. Similar to class 1, but slightly stronger, the $qg\omega_{bot}$ shows a pattern of low values north-east of the cyclone centre but no area with downward motion of air within the cyclone domain (cf. Fig: 5.5b).
In **class 2** the area of high values of $EADY$ is not much smaller than in class 4, the highest values expand over a smaller region (cf. Fig: 5.5c). It is also bent around the cyclone centre. Again the shape of the area with strong baroclinicity indicates the average orientation of the fronts of the ETC cases in this class. In this class the fronts seem to lie closer together than in class 4. The $qg\omega_{bot}$ has the strongest values (negative and positive) in this class. Thus vertical motion in the mid-troposphere (at 600 hPa) is most pronounced in this class.
The vertical motion represented by $qg\omega_{top}$ (cf. Fig: 5.3) and $qg\omega_{bot}$ (cf. Fig: 5.5) varies strongly in a 45° angle to the horizontal and vertical axes of the biplot (cf. Fig: 5.1). This shows that vertical motion in the mid-troposphere is dependent on upper-level forcing and tropospheric instability equally as much as on baroclinicity in the lower- and mid-troposphere. Both forcings have to be high to yield strong vertical movement at the 600 hPa level. The $qg\omega_{top}$ is slightly closer related to variation in the upper-level forcing and tropospheric instability, while $qg\omega_{bot}$ varies stronger along with variation in low- and mid-level baroclinicity.

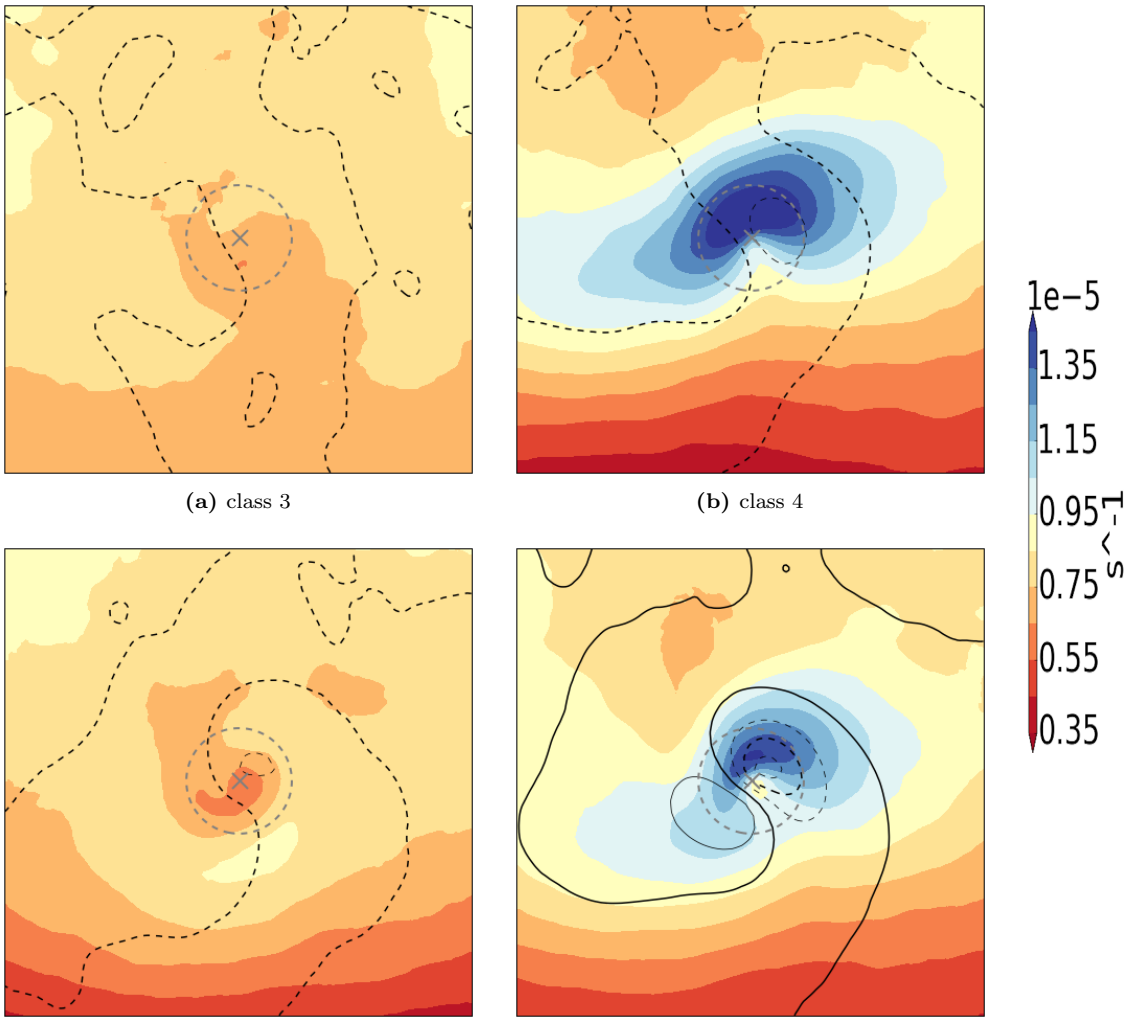

(a) class 3 **(b)** class 4

(c) class 1 **(d)** class 2

Figure 5.5: Composites of classes 1 to 4: *EADY* (filled contours) and $qg\omega_{bot}$ (black contours). Same as for Fig: 5.2c, but here shown for classes 1-4. PV_{bot} in PVU (filled contours) and $qg\omega_{top}$ (black contours) in steps of $2 \cdot 10^{-2}$ Pas^{-1} (range 0.1 and -0.2 Pas^{-1}), full lines mark descent, dashed lines mark ascent.

5.2.4 $CAPE$ and RR_{6h}

The patterns of RR_{6h} are focussed to the CIR, showing their maximum at the centre of the cyclone. Classes 1, 2, and 4 show higher maximum values and over a larger area than class 3. Over all the shape of the RR_{6h} values shows increased accumulated precipitation in the warm sector decreasing into slightly varying directions. The orientation of the accumulated precipitation indicates that in class 1 greater amounts of precipitation occurs along the bent back warm front (SE-NW). In class 4 the area of the RR_{6h} values mirror the extend of the cold front (SW-NE), and in class 2 they expand along the cold front and into much of the warm sector (SW-N/NE) with very high values inside CIR.
The values of RR_{6h} are higher within the CIR in classes 2 and 4 than in the other two classes. This does not correlate with the orientation of the parameter vector in the biplot, where a variation of RR_{6h} more along the vertical (not the horizontal) axis is visible (cf. 5.1). A reason for this contrasting variation in the value of RR_{6h} could be traced back to the fact that the biplot is based on the single parameter values calculated from A_{norm}, while the composites show the average values of A at every grid point.
In **class 3** very little precipitation occurs, the $CAPE$ values are low, and only a weak gradient of $CAPE$ is present in the CIR. As described above, the orientation of the area experiencing precipitation differs from class to class. The area and the orientation of RR_{6h} correlates strongly with the second composite displayed in Fig: 5.6 ($CAPE$), for **classes 1** and **2**. High convective potential ($CAPE$) within the CIR indicates that the accumulated precipitation is at least partially convective in class 1. In **class 4** the shape and orientation of the two composites also coincides, the values of $CAPE$ are however lower than in classes 1 and 2.
Note, that here two composites of parameters with different temporal extent are compared. $CAPE$ shows the instantaneous convective potential at PMI, while RR_{6h} captures the average precipitation accumulated in the 6 hours leading up to PMI. The exact location of the values of RR_{6h} can also be influenced by the conditions prior to PMI, which are not discussed in this interpretation of the classes.

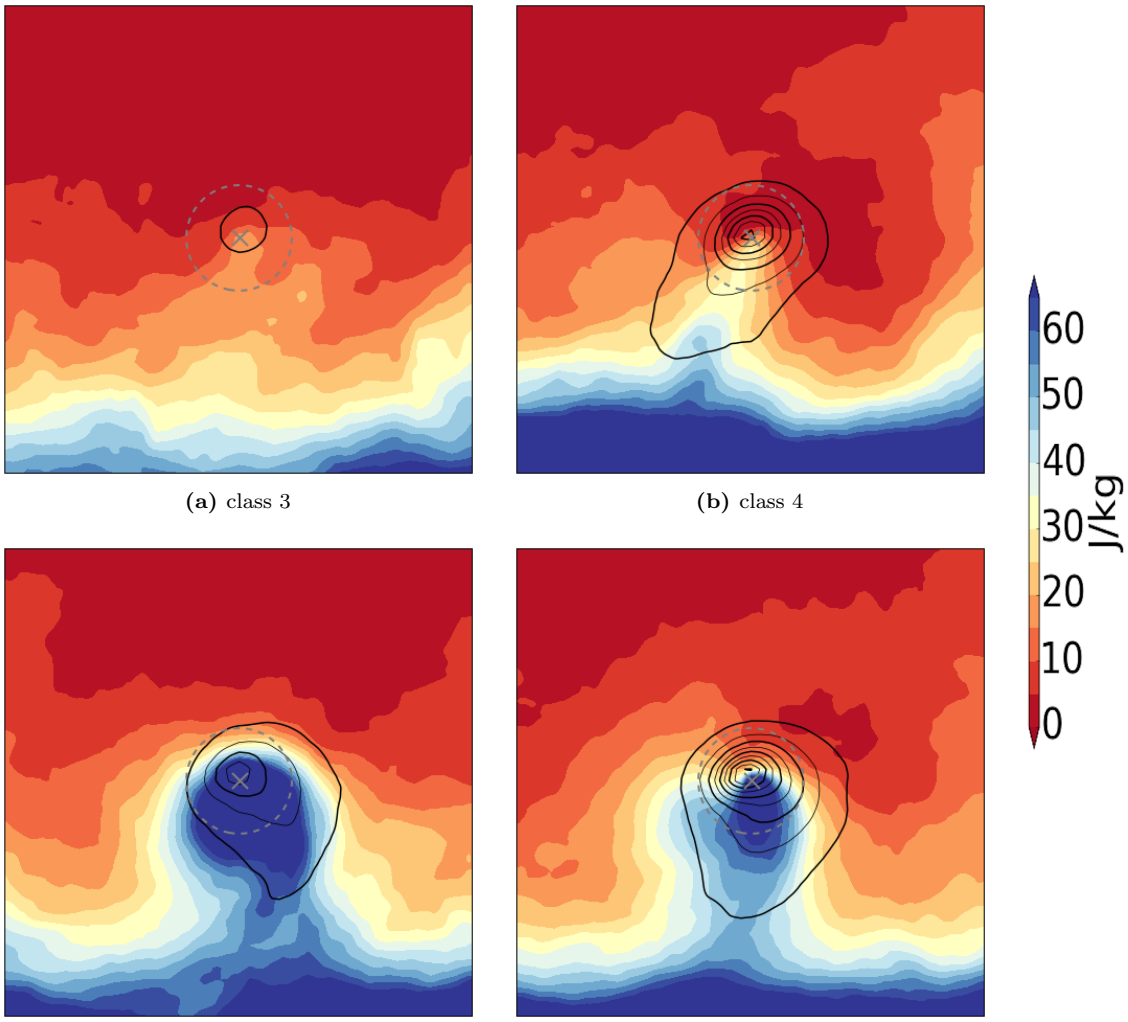

(a) class 3 **(b)** class 4

(c) class 1 **(d)** class 2

Figure 5.6: Composites of classes 1 to 4: $CAPE$ (filled contours) and RR_{6h} (black contours). Same as for Fig: 5.2d, but here shown for classes 1-4. $CAPE$ in J/kg (filled contours) and RR_{6h} (black contours) in steps of $1mm/6h$ (range 1 to $10mm/6h$).

5.2.5 Synthesis

To summarize, **class 1** cyclones are related to an upper-level PV cutoff with a short meridional jet streak south of the cyclone centre and the CIR. Vertical movement is at a medium level at 600 hPa (cf. $qg\omega_{top}$ and $qg\omega_{bot}$). They are further located in a zone of weak baroclinicity and high convective potential. The indication of curled up bent-back fronts mentioned in Sec: 5.2.2 are more enhanced in the composites of Q_{int} and $FGEN_{850}$ in the appendix D. The parameter T_{ADV850} shows where warm and cold air advection takes place, respectively (cf. App: D). It further highlights the shape of the curled up fronts as that is where the strongest temperature advection occurs. Class 1 cyclones also show high values of accumulated precipitation RR_{6h} correlating with the almost circular shape of high $CAPE$. This indicates that the precipitation within the CIR below the upper-level PV cutoff is at least partially driven by convection.

The cyclones in class 1 are ETCs which stand out due to their relation to upper-level PV cutoffs. This class contains the least amount of cases (16%) compared to the other classes. Based on the instantaneous values of sea level pressure, the events in this class have the second highest intensity at PMI (after class 2), closely followed by class 4 cyclones. The Bergeron values marked in the biplot however show that a much smaller amount of the ETCs in this class experience explosive intensification during their life time (compared to class 4).

Class 2 cyclones are related to an upper-level trough, with a strong PV gradient within the CIR. In combination with their positioning in the left exit region of a jet streak, strong updraft occurs in the CIR. The strongest vertical movement (upward and downward) occurs in the cyclone domain of the cyclones in this class. In addition they lie in an area of very strong baroclinicity, indicating elongated frontal systems. Temperature advection is high in the region of the fronts (cf. T_{ADV850} in App: D). The convective potential is high, hence the stability of the troposphere is low. Moderate values of precipitation occur along the cold front and in much of the warm sector in the 6 hours prior to PMI.

The composite of sea level pressure of class 2 shows the most intense low pressure in the CIR, indicating that the ETCs in this class are more intense at PMI, compared to the other classes. In addition to this, class 2 also contains the largest amount of cyclone events with high Bergeron values. This means that not only are the cyclones in this class (22%) most intense at PMI, they also experience the greatest intensification during their life time.

The cyclones in **class 3** stand out with low values and weak gradients of the parameters, which were discussed in this chapter. The upper-level PV in the CIR lies between 1.5 and 2 pvu, showing no gradient but being at the tip of a small large-scale diversion of higher values of PV_{up} southwards. The cyclones in this class are also not related to a jet streak anywhere in the cyclone domain indicating no baroclinicity in the mid-troposphere. The gradients of θ_{e850} and the convective potential ($CAPE$) are very weak. Baroclinicity at low-levels is represented by medium values of $EADY$. As upper-level flow and lower-level baroclinicity are weak, the accompanying vertical motion is equally as feeble.

For class 3 it is interesting to add that the composites of parameters SKT, and $SSHF$ show that the CIR of these cyclones is located in regions with negative surface temperatures (-3 to $-13C$, cf. App: D). This class has the lowest surface temperatures of all 5 classes. In addition parameters $TRAdP_{48}$ and $TRAd\theta_{48}$ and their 6 hour maxima ($TRAdP_{MX}$ and $TRAd\theta_{MX}$) show that the air parcels in the CIR of the cyclone events in this class experienced a significant amount in pressure drop and close to no change in θ during the hours prior to PMI.

Over all the cyclones in class 3 are ETCs which do not stand out to be intense, or undergoing strong intensification. At PMI the cyclones in class 3 are the weakest (cf. Fig: 4.11), the colors of the cases in the biplot (cf. Fig: 5.1) indicate the largest number of low Bergeron values. It can be concluded that this class contains the quarter (25%) of all ETC which are result in very few intense events.

Cyclones in **class 4** are related to an upper-level wave in PV which possibly develops into a trough in the subsequent time steps. The gradient of PV_{up} is strong within the CIR. The centre of the cyclone and most of the CIR is located underneath a jet streak which leads to medium impact of upper-level forcing on vertical updraft. Compared to class 1, the cyclones in class 4 are influenced

more by low-level baroclinicity. In classes 1 and 4 medium strength updraft is present at the 600 hPa level, it is weaker than in class 2 and stronger than in class 3. In class 1 the forcing from above ($qg\omega_{top}$), and in class 4 the forcing from below ($qg\omega_{bot}$) 600 hPa is stronger than in the other class. In both classes the values of $qg\omega_{top}$ and $qg\omega_{bot}$ add up to medium strength vertical motion in the mid-troposphere. The baroclinicity is strongest, and covers the largest area within the cyclone domain in this class 4, compared to all other 4 classes. The convective potential is however not so high and the amount of precipitation ranks second after class 2. It occurs along the cold front with a maximum at the cyclone centre.
Class 4 stands out based on the strongest low-level baroclinicity of all classes. It contains a similar amount of ETC events (17%) as class 1, and shows the second greatest number of ETC with high Bergeron values.

Chapter 6

Discussion & Conclusion

In this chapter, the classification is analyzed based on the hypotheses which were stated in the introduction. Furthermore, methodological artifacts which have an influence on the objective classification method are discussed. The chapter closes with a short summary of the key results and an outlook on possible extensions in future studies.

6.1 Discussion

6.1.1 Reflection on hypotheses

H1 - On Parameters: parameters used for the objective classification are relevant for the largest deepening phase.
At PMI the mean of the distribution of the parameter values differ from the climatology (0-anomaly, cf. Chap: 4). This shows that on average, at PMI the parameters have values which are higher or lower than those which are expected to occur at the same geographical location based on climatological conditions. The deviation of the parameter values from the climatology leads to suggest that the parameters are relevant at PMI, thus also for the largest deepening phase of ETCs.
The preliminary interpretation, indicating a difference in importance of the parameters for the PCA based on the width of the distribution in Chap: 4 could be adjusted. The preliminary interpretation being: "Parameters with a narrow distribution, and therefore high numbers of cases within a small range of standard deviations, can be considered as requirements for the physical condition at PMI. Parameters with a large range of standard deviations vary a lot from case to case, which could allow a value-dependent separation of the different cases into classes. This leads to suspect that parameters with a broader distribution are likely to play a bigger role in the PCA". However, these parameter value distributions are only 1-dimensional. Hence, they do not provide insight into the inherent multidimensionality of the problem. Based on the data analyzed, the following adjusted interpretation holds true: All of the parameters which show great variety in parameter values in the biplot of the rotated PCA show a broad frequency distribution in 1-dimension.

H2 - On Classes: it is possible to distinguish an appropriate number of classes in the parameter space, which are reasonable from a physical point of view and significantly different.
Using a total number of 5 different classes can be considered as appropriate, as it is possible to distinguish 5 classes which are physically different. Three of the classes (class 1, 2, 4) show clear characteristics, which differ strongly from each other by at least one key feature. Another one of the 5 classes has diffuse and weak values (class 3) of most of the parameters, also highlighting a very different tropospheric condition. The 5^{th} class (class 5) comprises averages of the different characteristics of the first 4 classes. Thus, the first 4 classes have different physical characteristics of reasonable significance, while the 5^{th} class differs based on the combination of the characteristics of the other classes.

From a physical point of view the characterization of the 5 different classes is reasonable. They represent combinations of phenomena and forcings, which are well established as important drivers for cyclone development and intensification. The split of the classes along the horizontal and vertical axis can be justified by the fact that it confirms the importance of baroclinicity (horizontal), and the tropospheric instability and upper-level forcing (vertical), represented by the parameter vectors which vary predominantly in one of the two directions (horizontal: $EADY$, $|\Delta\theta_{850}|$, $VELJET$, $|\Delta\theta_{e850}|$, $EADY_{up}$; vertical: PV_{up}, Z_{ANOM}, Z_{500}, $CAPE$, $\Delta\theta_{SKT700}$; for a short description of these parameters cf. Tab: 2.1).

H3 - On Intensification: cyclones of the same class intensify based on a similar combination of parameters, but show varying amplitudes of intensification.
All cases grouped into one class experienced similar tropospheric conditions. Hence, cyclones of the same class intensified based on a similar combination of parameters. The distribution of the Bergeron values across the classes shows a clear pattern, this can be observed in the biplot (cf. Sec: 4.2.3). Most ETCs with low Bergeron values clearly lie in classes 1 and 3, while ETCs with higher values, also those exceeding 1 Bergeron, are comprised in classes 2 and 4. The increase of Bergeron values along the horizontal axis, i.e., with increasing baroclinicity, is much stronger than the correlation of the Bergeron values with tropospheric instability and upper-level forcing.
If the classes were to be ranked according to the maximum Bergeron value during their life cycle, class 3 would clearly comprise ETCs which mostly did not intensify much (< 0.5 Bergeron) and class 2 would clearly comprise the highest number of ETCs which experienced explosive intensification (> 1.5 Bergeron). Classes 1 and 4 would be less clear to rank, where class 4 comprises slightly more cyclones with medium to high values (> 0.5 Bergeron) than class 1. The cases with the 55 highest Bergeron values (> 2.6 Bergeron) are similarly distributed in classes 2 and 4. The 15 cases with the largest intensification (> 2.9 Bergeron) are spread unevenly over classes 2 and 4, with 2/3 of them being located in class 2. Cases in classes 1 and 3 do not contain any cases with very high Bergeron values (> 2.6 Bergeron) and class 5 only contains 2 cases. It is thus highly unlikely for ETCs with tropospheric characteristics which compare to those of classes (1, 3, or 5), to experience very strong explosive intensification (> 2.6 Bergeron).

6.1.2 Subjectivity in the objective method

The influence of two aspects bias the implementation and analysis of the objective classification method of ETCs, at the point during which the ETCs underwent their maximum intensification: One being the choices made to define the parameters and their calculation, and the second being the choice and method to rotate the axes of the biplot.
The parameters chosen to best capture the physical conditions of the atmosphere during PMI introduce subjectivity. The large number of 29 different parameters is defined to reduce this subjectivity. The method used to compute the parameter values (A) and their normalization (A_{norm}) at every grid point is based on subjective but well educated choices, respecting established theory (cf. Sec: 2.3). The definition of a 500 km radius as the CIR to calculate the single parameter value, is arbitrary. This value is further biased by the choice of computing it as an average above or below the median (cf. Sec: 2.3 and Chap: 4), introducing a slight overestimation of the parameter on the intensification.
The second methodological aspect of this objective classification, which is not free of all subjectivity, concerns the varimax rotation performed prior to the classification. If class borders were laid into the biplot of the unrotated PCA, the resulting classes would not show clear differences in their physical characteristics. Hence, it is not possible to achieve a split in the biplot of the unrotated PCA which is reasonable from a physical point of view. The varimax rotation is chosen to find axes along which the physical characteristics vary strongly, in order to facilitate the interpretation from a physical point of view. Again theory supports this choice (Jolliffe, 2002).
The selection of the principal components to be rotated is again arbitrary to a certain extent. The first 4 principal components represent a large amount of the variance within the data set, and each subsequent principal component adds a small amount of information. Basing the classification on the first two rotated axes is sensible from a statistical perspective as they represent more than

40% of the variance, in spite of the covariance introduced by the rotation. The representation of the data set in a biplot with the first two rotated axes is used for two reasons: One being the reduction to 2-dimensions to facilitate the interpretation, and second, 5 classes are an arbitrary number which is neither too large or too small for a clear differentiation. Using the biplot of the rotated PCA further allows the 5 classes to be determined with clear differences in their physical characteristics.
The introduction of a certain degree of subjectivity aside, the analysis of the implemented objective classification method of ETCs results in a reasonable attempt at addressing the research questions of this thesis. As explained in the introduction, currently, established classification methods for ECTs are largely based on subjective analysis of a limited number of case studies (c.f. Petterssen and Smebye (1971), Shapiro and Keyser (1990), and Devenson et al. (2002)), which greatly limits their applicability. The method applied in this thesis, on the contrary, is based on a large number of parameters, which aim to capture the physical conditions of the troposphere in the cyclone's vicinity. The analysis of the parameter values of over 8000 ETC events offers a robust foundation for an objective choice of classes. The objective classification of ETCs, at the point during which the ETCs underwent their maximum intensification, can be applied to a different data set of ETCs, with a focus on a different time period or region of the world.

6.2 Conclusion

6.2.1 Summary

A Principal Component Analysis (PCA) and varimax rotation was used as an objective approach for a classification of ETCs in their phase of maximum intensification. It was demonstrated that the method, originally developed to classify ETCs at their genesis (Graf, 2014), is also applicable to ETCs at PMI. The parameters used for objective classification at cyclogenesis are also relevant at PMI.
The biplot resulting from the PCA is rotated based on the varimax method. The rotation enables a physical-based interpration of the horizonal and vertical axes of the rotated biplot. Note, a rotation was not used or required in the method by Graf (2014). The parameters $EADY$, $|\Delta\theta_{850}|$, $VELJET$, $|\Delta\theta_{e850}|$, and $EADY_{up}$ vary strongly along the horizontal axis and can be summarized as representing "low- to mid-level baroclinicity". The vertical axis is characterized by strong variations in the parameters PV_{up}, Z_{ANOM}, Z_{500}, $CAPE$, and $\Delta\theta_{SKT700}$, which can be summarized as representing "upper-level forcing and tropospheric instability" (for a short description of these parameters cf. Tab: 2.1). It is thus possible to distinguish an appropriate number of classes in the parameter space, which differ based on their physical characteristics.
The different ETC events (> 8000) are distributed over 5 different classes. Each class has its own characteristics concerning the tropospheric conditions at PMI. Cyclones in class 1 (16%) are related to an upper-level PV cutoff and have curled up frontal systems. Cyclones in class 2 (22%) are characterized by an upper-level trough and strong mid- and low-level baroclinicity. Cyclones in class 3 (25%) stand out as ETCs, which occur north of a baroclinic zone in regions with low surface temperatures, the gradients of most parameters are weak. Cyclones in class 4 (17%) are related to an upper-level wave in PV and very strong mid- and low-level baroclinicity. Cyclones in class 5 (20%) are an averaged combination of the 4 other classes.
ETCs of the same class intensified based on a similar combination of parameters. The amplitude of intensification varies within each class. A gradient of intensification along the horizontal axis of the biplot differentiates the classes. Hence, the classes differ with respect to the contained number of ETCs events with strong/weak intensification.

6.2.2 Outlook

The understanding of the maximum intensification phase of ETC and the different processes which play a role in it, can be improved further. An analysis of multiple individual time points during the intensification phase could be used to calculate multiple classifications. The characteristics of

the troposphere in the vicinity of an ETC event varies over time. Classifying an ETC at different time points (e.g. in 6 hour intervals), during its maximum intensification phase, could result in an allocation into different classes. Each ETC could be analyzed based on an average or combination of the different classes, which it is part of over the phase of maximum intensification. The successive change in class allocation could also be analyzed in more detail, to determine the sensitivity of the classification method to the time point. An analysis in-line with this type of investigation can be found in App: E.

In future work, objective classification could be applied to a different data set. The analysis conducted in this thesis was limited to ETC events in the Northern Hemisphere during the winter season of the years 2000-2011. The data set of further studies could differ in terms of the season or the hemisphere. Analyzing and comparing the patterns in the biplot and the composites could highlight similarities and differences between ETCs in different areas and seasons. The analysis could be conducted on a global scale, or regional scale such as a comparison between the Atlantic and the Pacific oceans, or between ETCs which intensify over land versus those which intensify over oceans.

Case studies such as the ones described in Chap: 3 are commonly categorized by, and compared to established classification methods such as the ones developed by Shapiro and Keyser (1990), or Petterssen and Smebye (1971) and Devenson et al. (2002). The limitations of these subjective methods were highlighted in the introduction. An objective classification of ETCs like the one discussed in this thesis can be applied to any ETC event and result in an objective allocation to one of the 5 classes. Supplementing case studies with such a classification will increase their comparability.

For further analysis, a direct connection between the classes defined based on the classification at the point of genesis, and the classification at PMI, could offer new possibilities for forecasts. If for example, a classification into class 3 at the point of genesis, would, with a defined certainty, exclude the possibility of the ETC to develop into a class 2 cyclone at PMI, this knowledge could be incorporated into weather models. Thus, the objective method could improve the available resources for forecasts. Weak or no correlations between the classification at these two time points would stress the great variety in ETC development. Finding the time point at which the classification at PMI can be predicted with reasonable probability would certainly extend the understanding we have of ETCs today.

Appendices

Appendix A

Potential Vorticity

The concept of potential vorticity (PV) is a tool which allows a simplified perspective on the dynamic processes related to cyclogegesis and intensification. Potential vorticity (PV) is a measure for shear in a fluid as it also occurs in atmospheric air flow. It is calculated as follows:

$$PV = -g\boldsymbol{\eta}\boldsymbol{\nabla}\theta \ , \tag{A.1}$$

where $\boldsymbol{\eta}$ is the absolute vorticity which is the sum of the planetary vorticity represented by the coriolis parameter f and the relative vorticity $\boldsymbol{\omega}$. The $\boldsymbol{\omega}$ describes the three-dimensional rotation of the wind field in the troposphere i.e. $\boldsymbol{\omega} = \nabla \times \boldsymbol{v}$. PV is dependent on the absolute vorticity ($\boldsymbol{\eta} = \boldsymbol{\omega} + f\boldsymbol{k}$) and the three-dimensional gradient of the potential temperature ($\boldsymbol{\nabla}\theta$). Under the constraint of friction-less adiabatic flow it is a conserved quantity (Hoskins et al., 1985). From the three-dimensional PV distribution in the atmosphere qualitative estimates of the temperature-, geopotential height-, and wind fields can be inferred. PV is hence a key quantity in dynamic meteorology.
PV can be altered by latent heating in the lower- and mid-troposphere, and friction in the boundary layer. In this context, the most important process for cyclone intensification is condensation. The resulting PV tendencies can be calculated as follows:

$$\frac{D}{Dt} = -g \underbrace{(\boldsymbol{\eta}\boldsymbol{\nabla}\dot{\theta})}_{\text{diabatic heating}} + \underbrace{(\boldsymbol{\nabla} \times \boldsymbol{F}\boldsymbol{\nabla}\theta)}_{\text{frictional processes}} \ , \tag{A.2}$$

where $\dot{\theta}$ represents the diabatic heating (e.g. by condensation) and F the sum of all non-conserved forces.
As PV is conserved under certain conditions the conceptual understanding of cyclones can be enhanced (Gray and Dacre, 2006). The invertibility principle allows to attribute specific wind fields to positive and negative PV anomalies in the troposphere (Lakcmann, 2012). A local positive (negative) PV maximum (i.e. positive (negative) PV anomaly) leads to a cyclonic (anticyclonic) wind field (Davis and Emanuel, 1991).

Appendix B

Case studies - A_{norm} plots

The plots in this section show the normalized parameter values (A_{norm}), corresponding to the time points and parameters described in the case studies in Chap: 3. The case studies Martin (1999), Klaus (2009), and Xynthia (2010) are arranged in the same order as in Chap: 3.

B.1 Martin

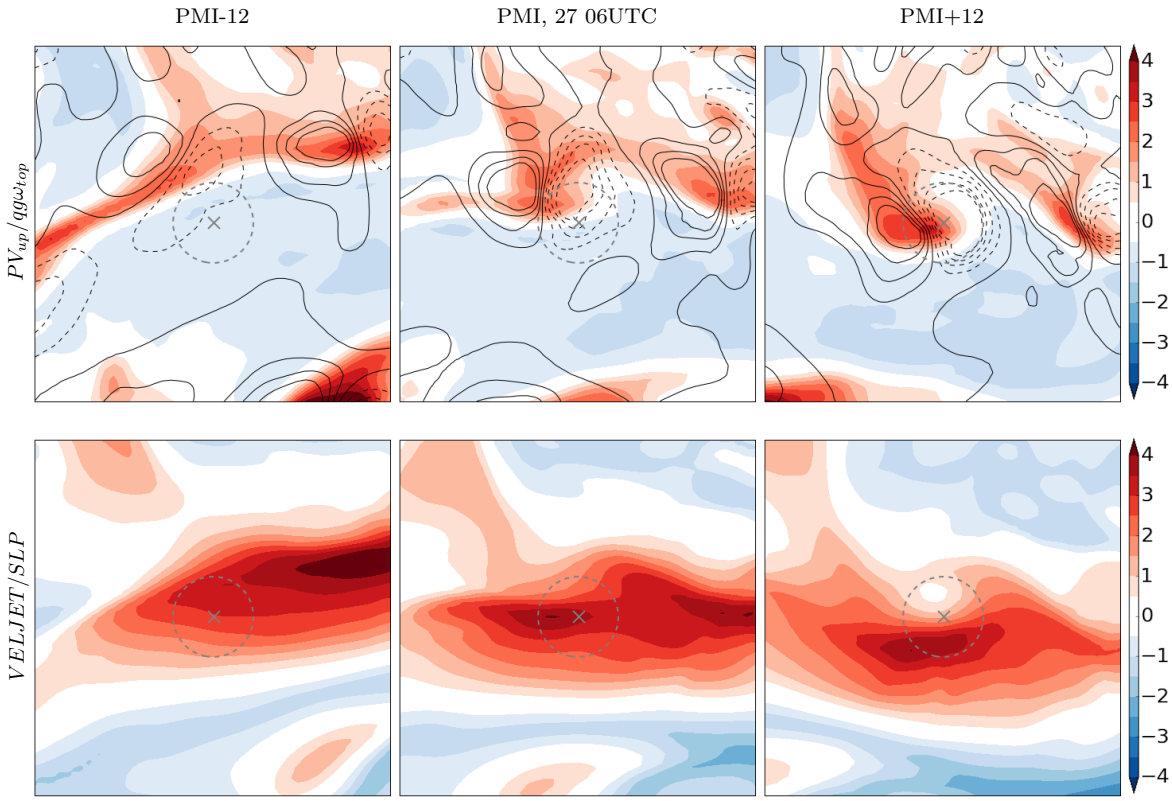

Figure B.1: Martin Dec 1999 27 00UTC - 27 12UTC, 6h time steps

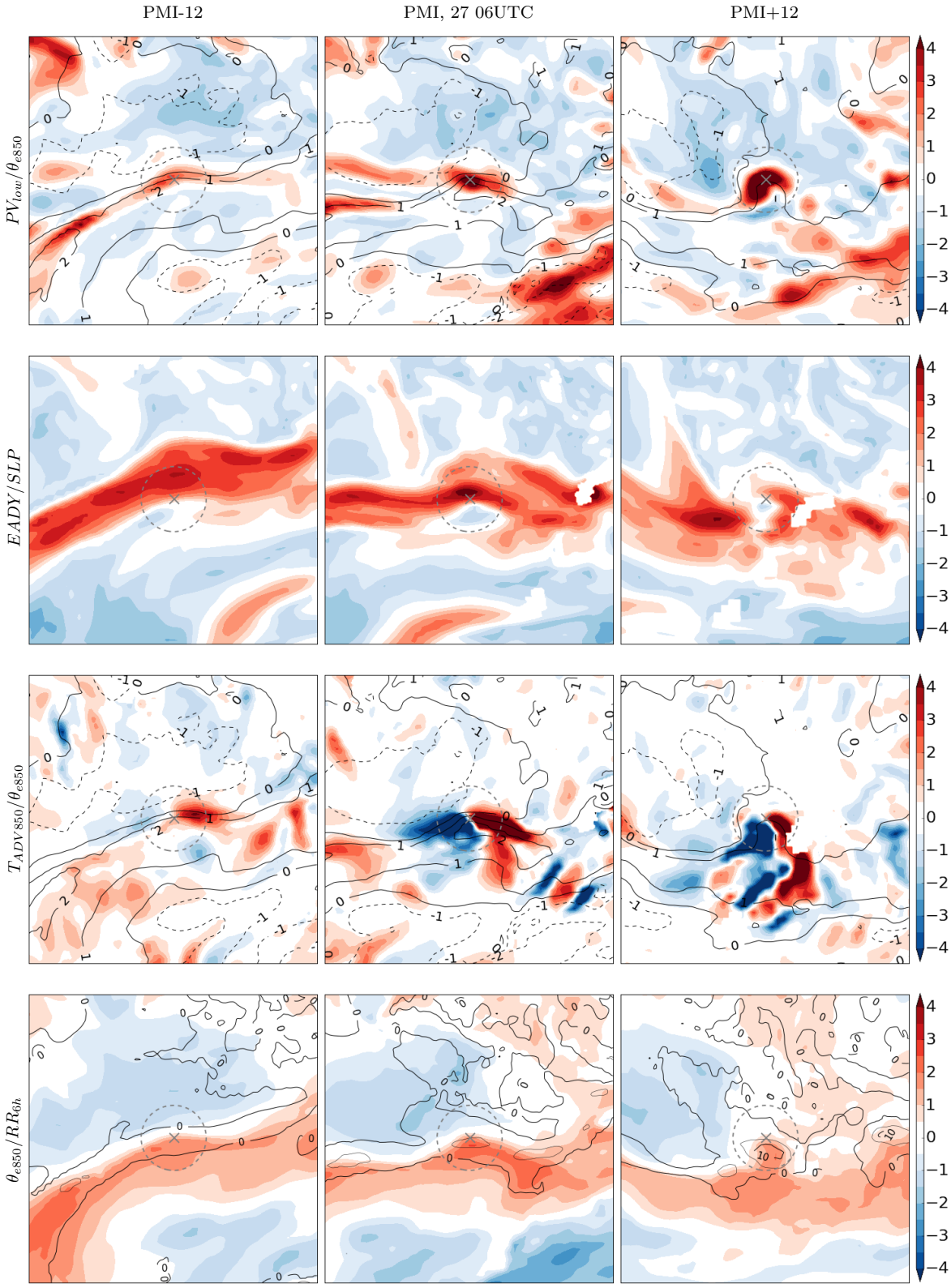

Figure B.1: (continued) Martin Dec 1999 27 00UTC - 27 12UTC, 6h time steps

B.2 Klaus

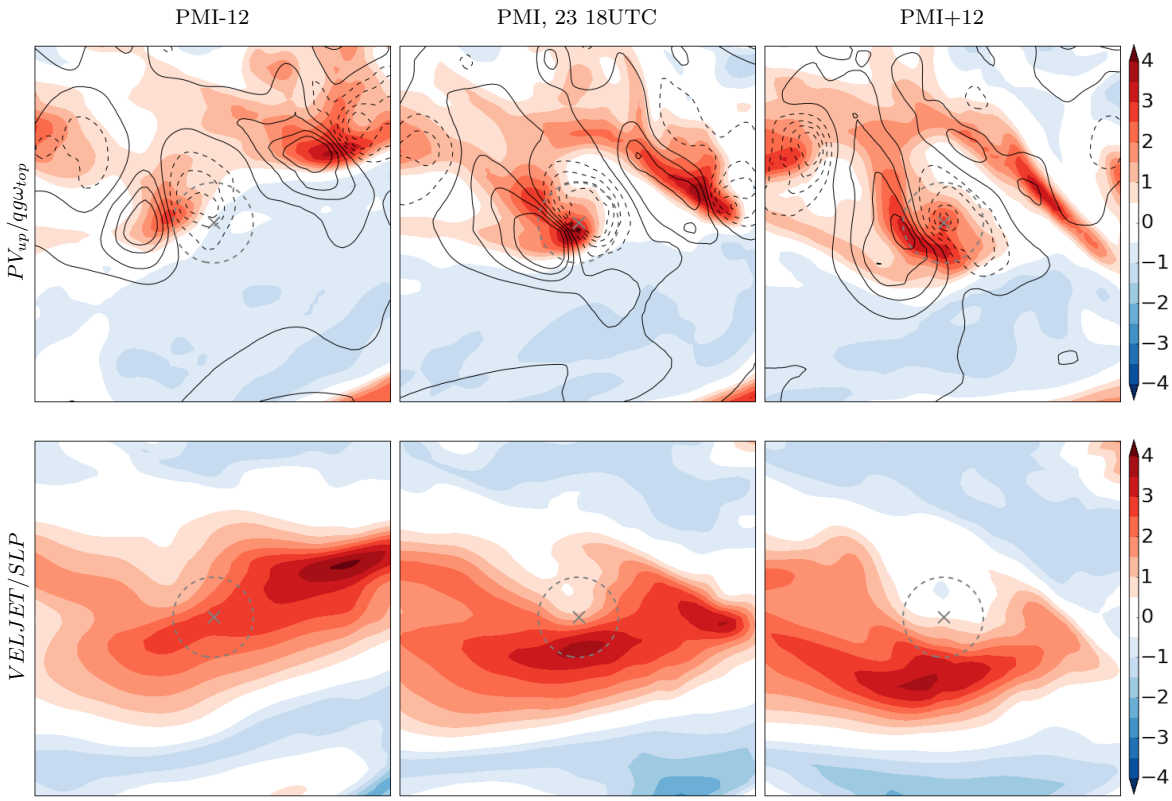

Figure B.2: Klaus Jan 2009 23 12UTC - 24 00UTC

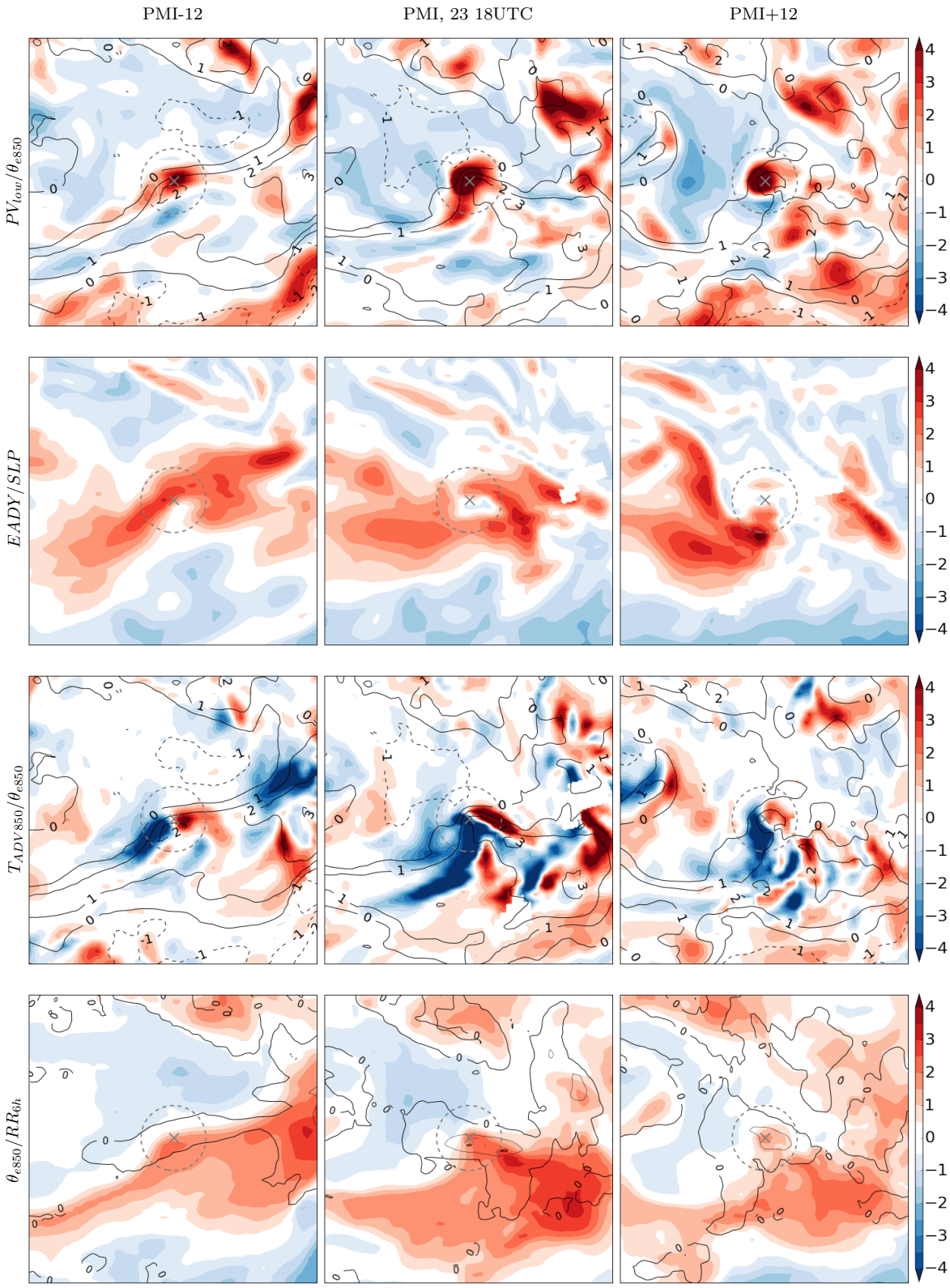

Figure B.2: (continued) Klaus Jan 2009 23 12UTC - 24 00UTC

B.3 Xynthia

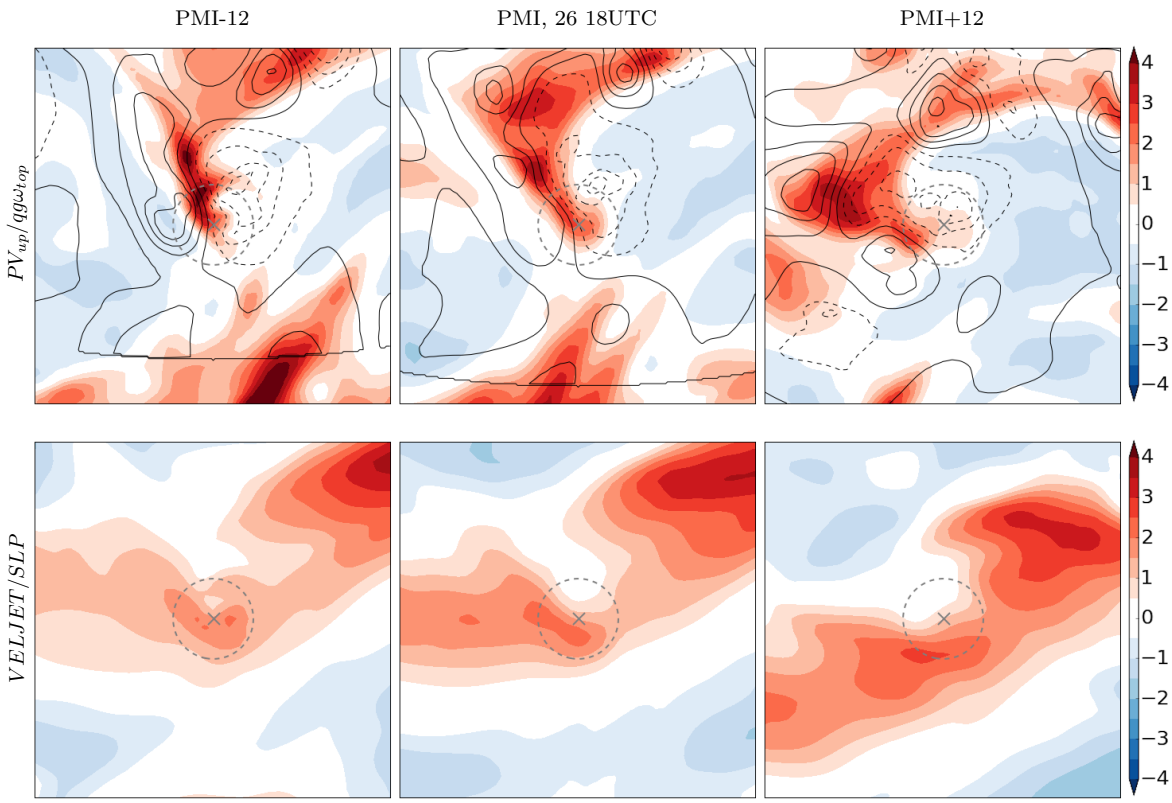

Figure B.3: Xynthia Feb 2010 26 12UTC - 27 00UTC

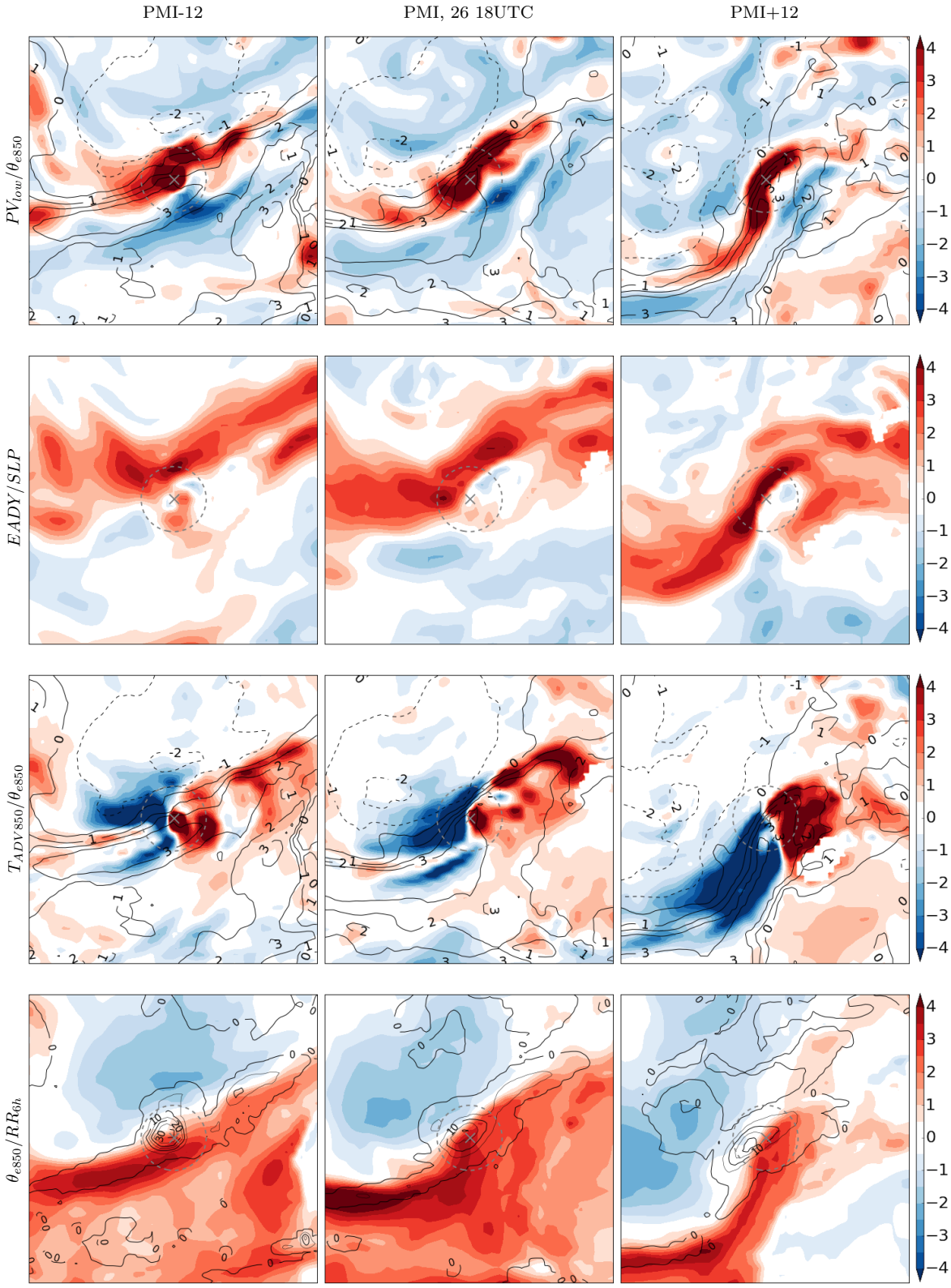

Figure B.3: (continued) Xynthia Feb 2010 26 12UTC - 27 00UTC

Appendix C

Parameter correlation plots

This section shows a collection of scatter plots representing the degree of correlation between parameter pairs, which were discussed in Chap: 4.

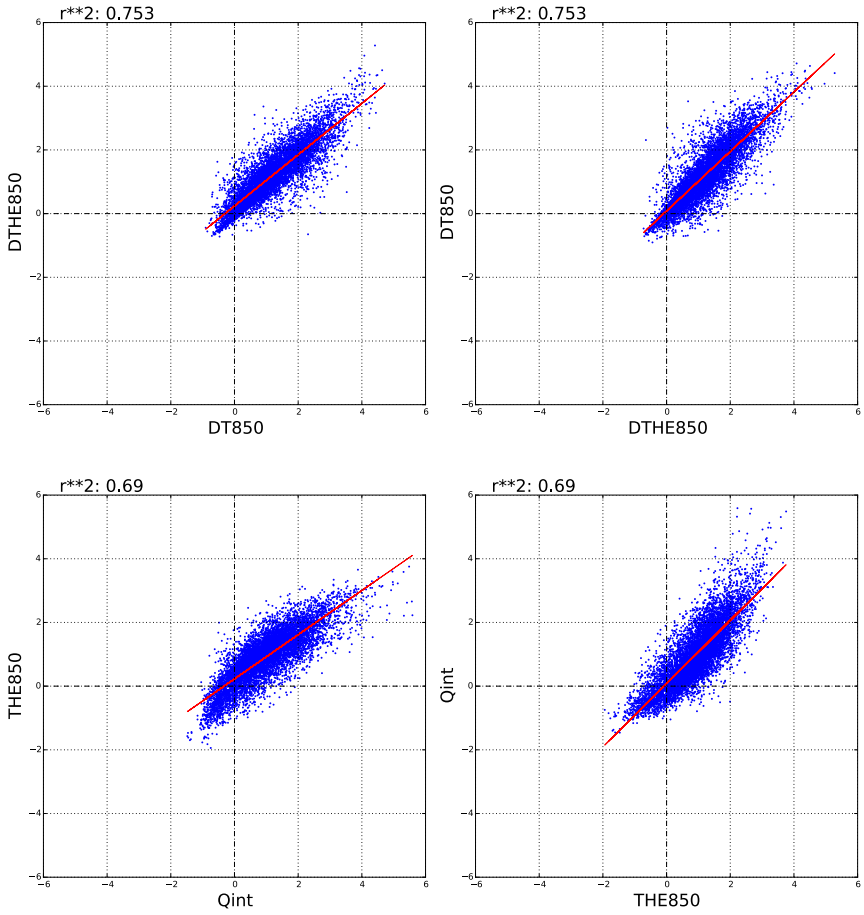

Figure C.1: Parameter combination examlpes with highest R^2 values.

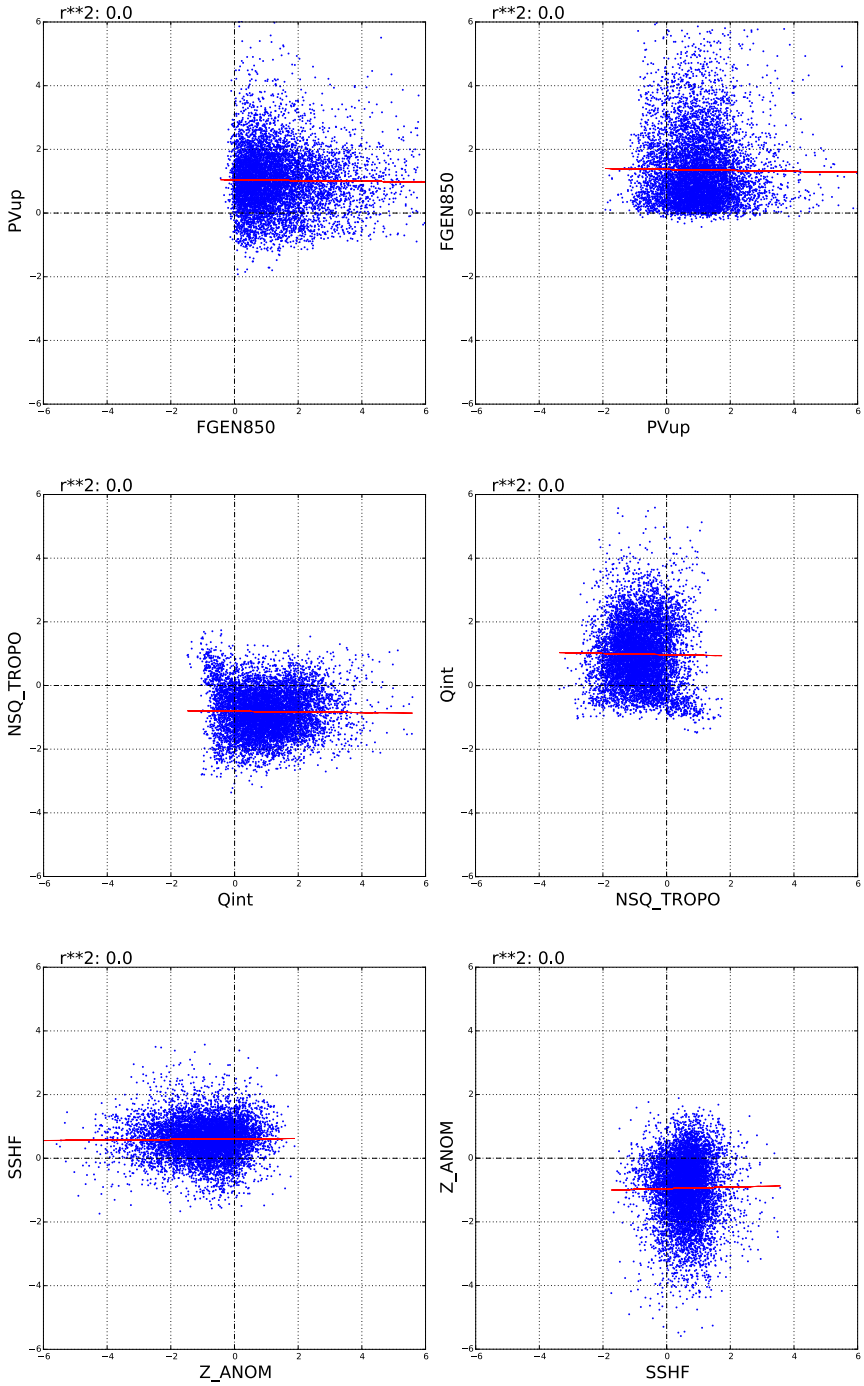

Figure C.2: Parameter combination examples with R^2 values of zero.

Appendix D

Composites - All parameters

As mentioned in Chap: 5, the plots in this section show the composites of all 29 parameters at PMI. The subplots of the classes are oriented based on their location in the biplot (cf. Fig: 4.10).

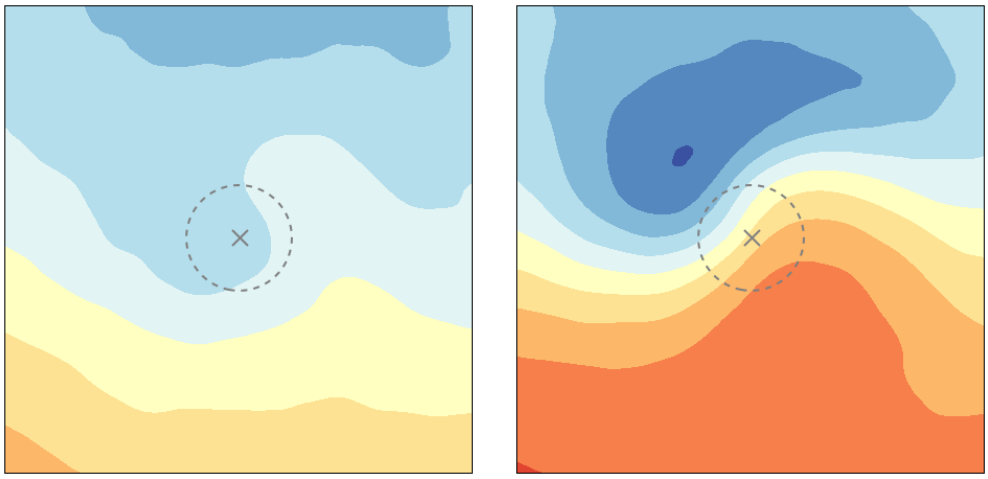

(a) class 3 **(b)** class 4

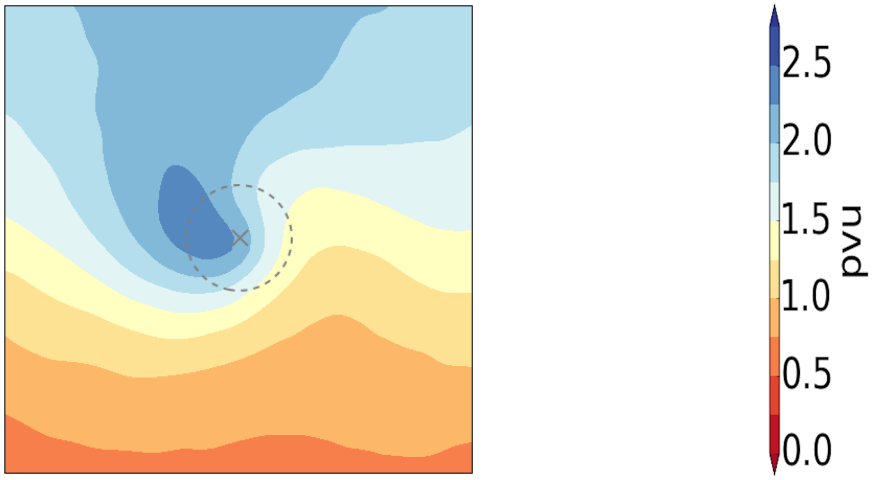

(c) class 5

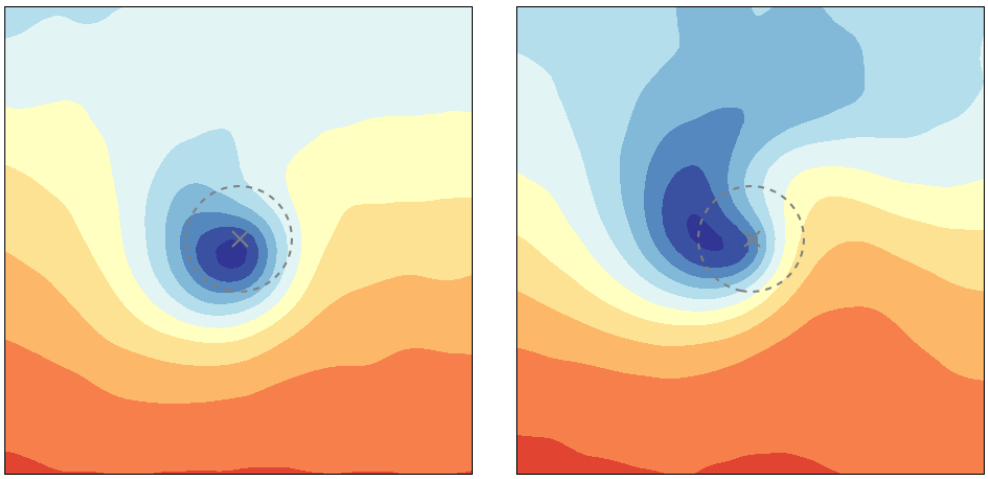

(d) class 1 **(e)** class 2

Figure D.1: PV_{up}

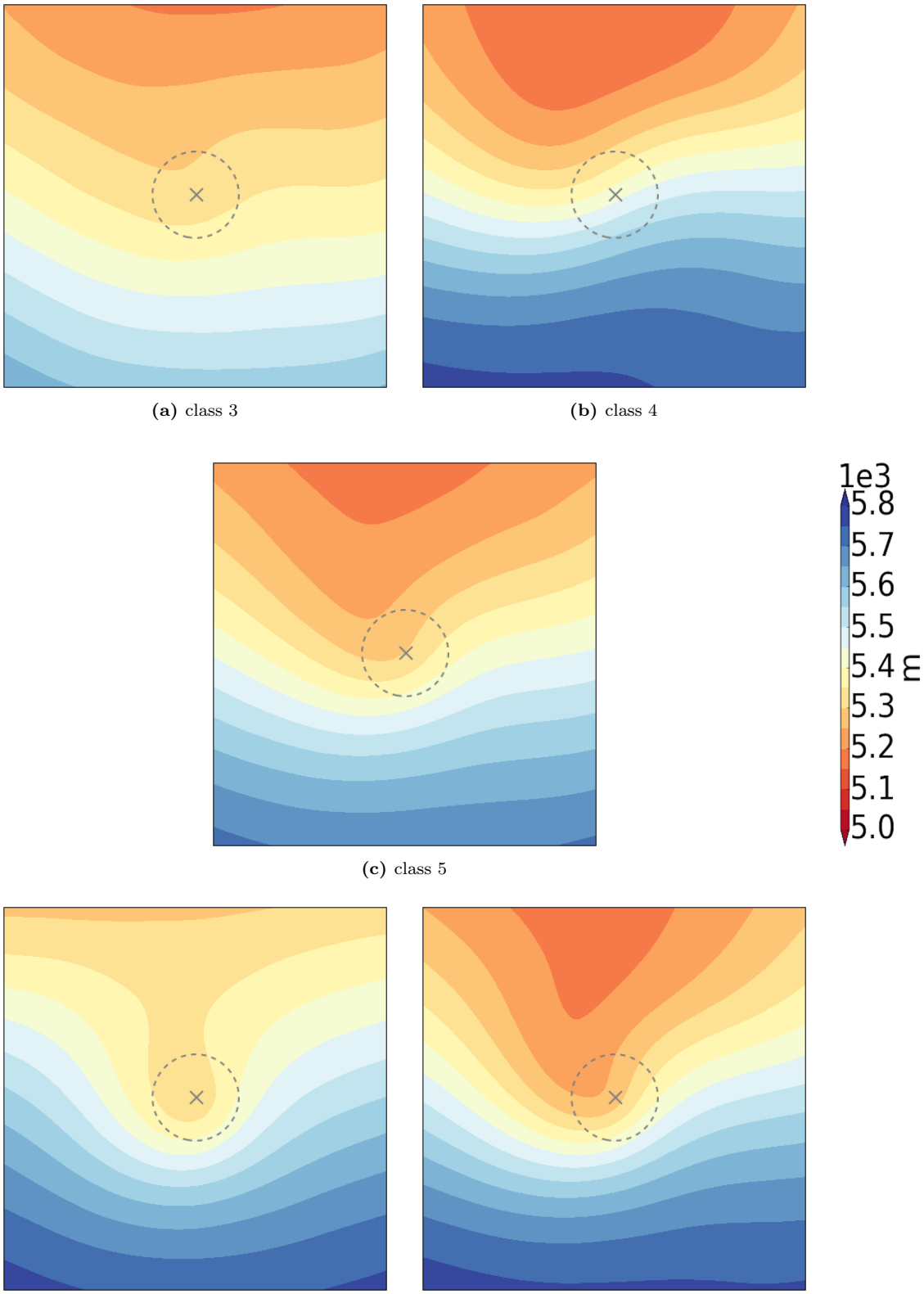

(a) class 3

(b) class 4

(c) class 5

(d) class 1

(e) class 2

Figure D.2: Z_{500}

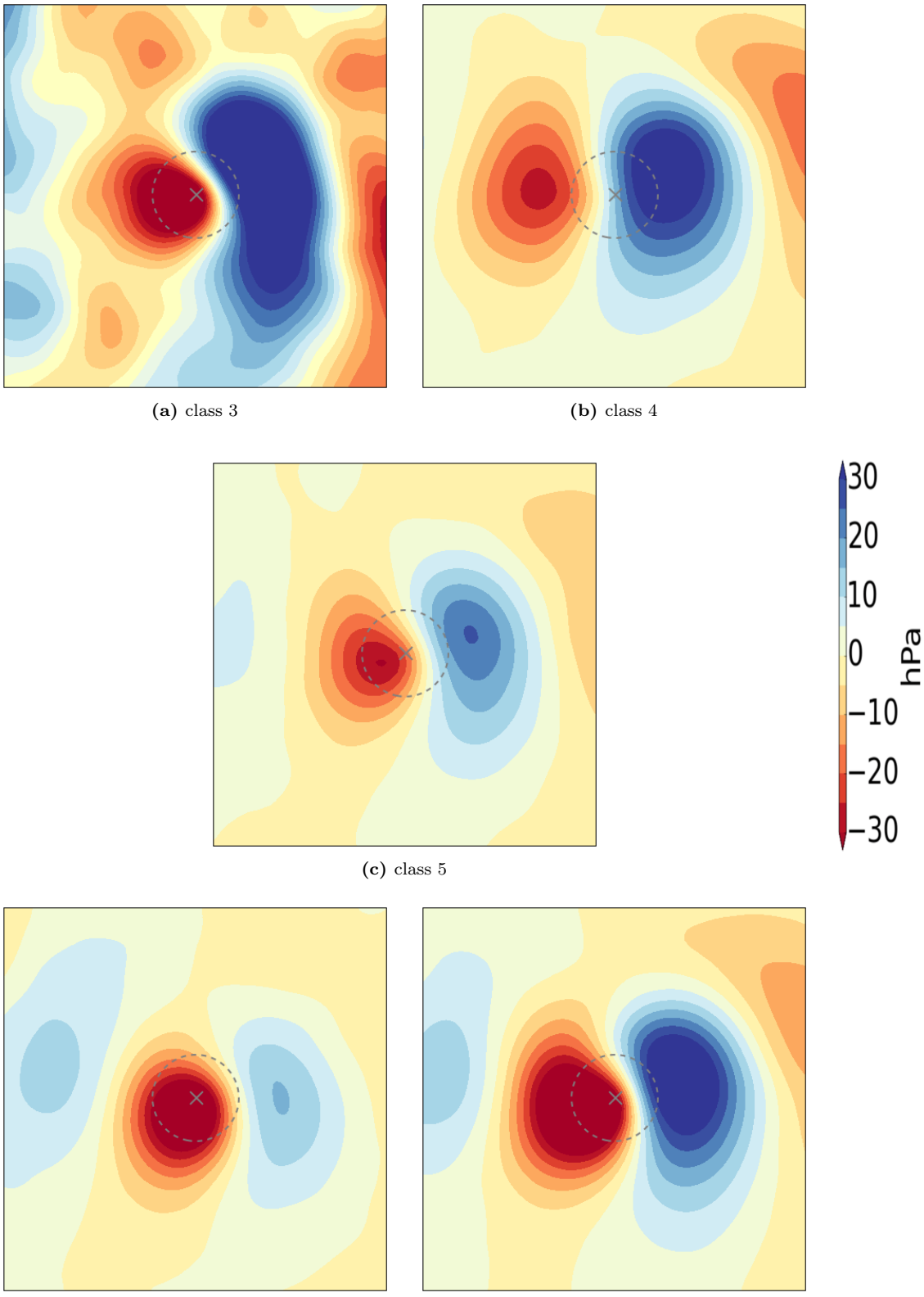

(a) class 3 **(b)** class 4

(c) class 5

(d) class 1 **(e)** class 2

Figure D.3: Z_{ANOM}

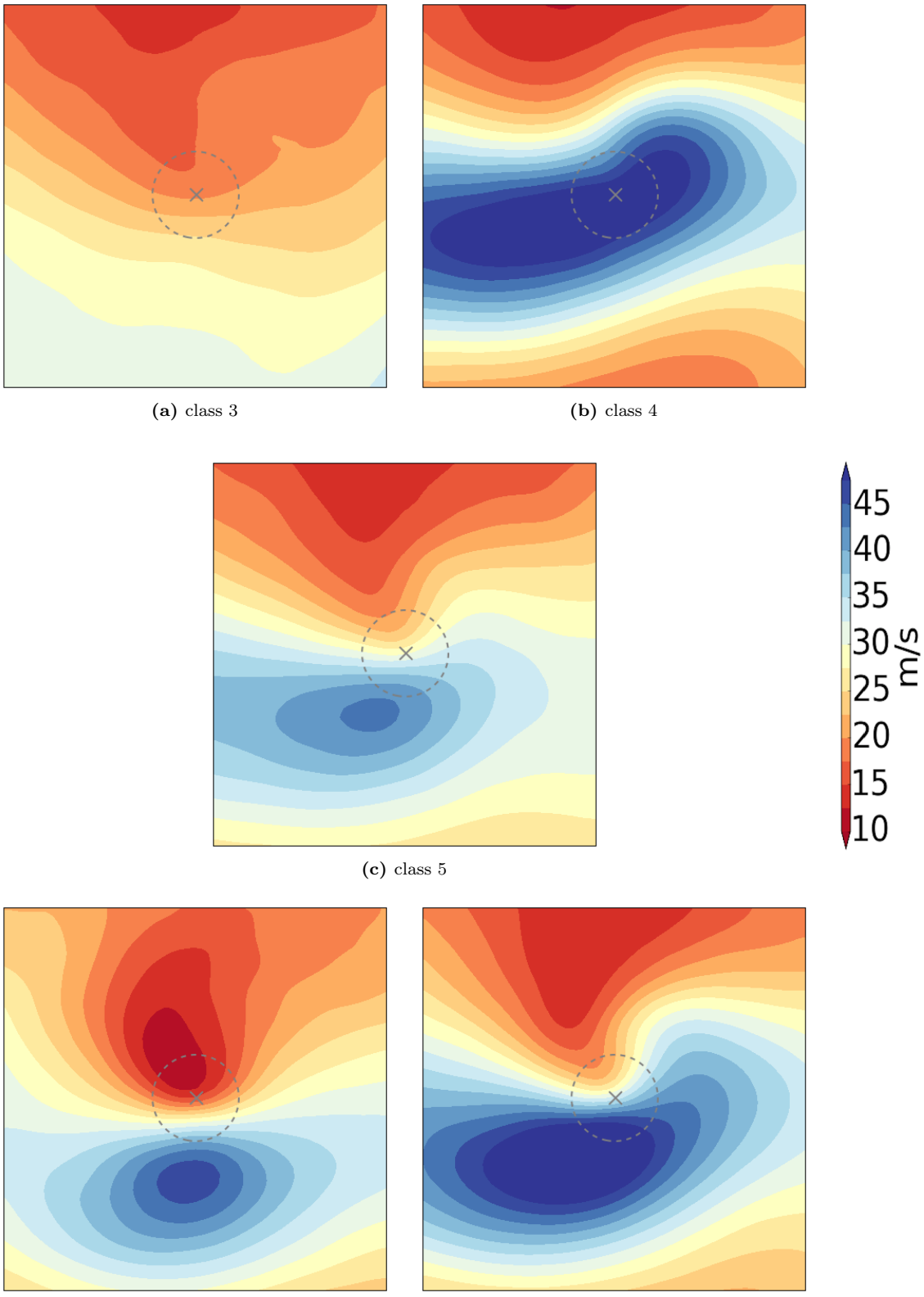

(a) class 3

(b) class 4

(c) class 5

(d) class 1

(e) class 2

Figure D.4: *VELJET*

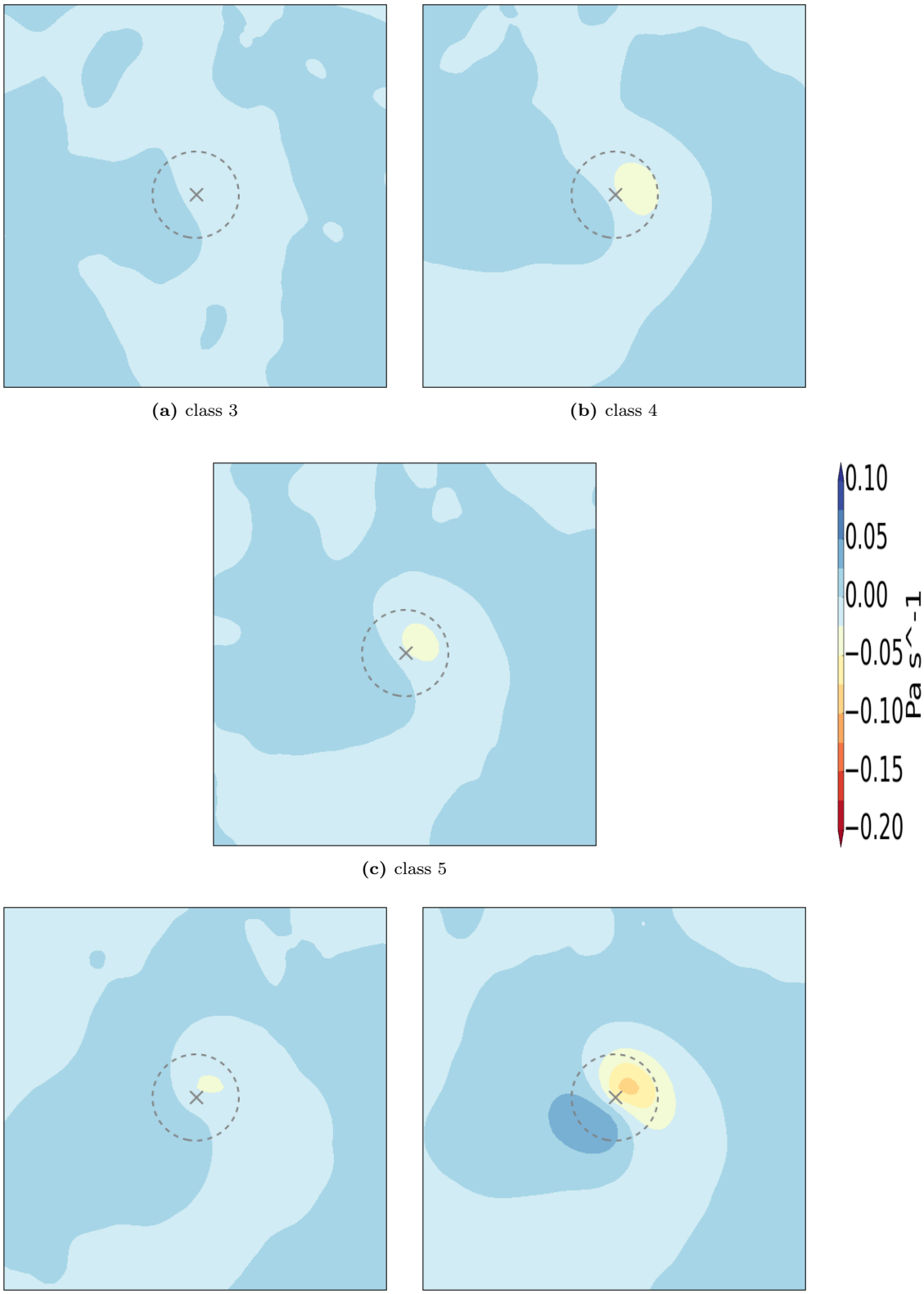

(a) class 3

(b) class 4

(c) class 5

(d) class 1

(e) class 2

Figure D.5: OM_{BOT3}

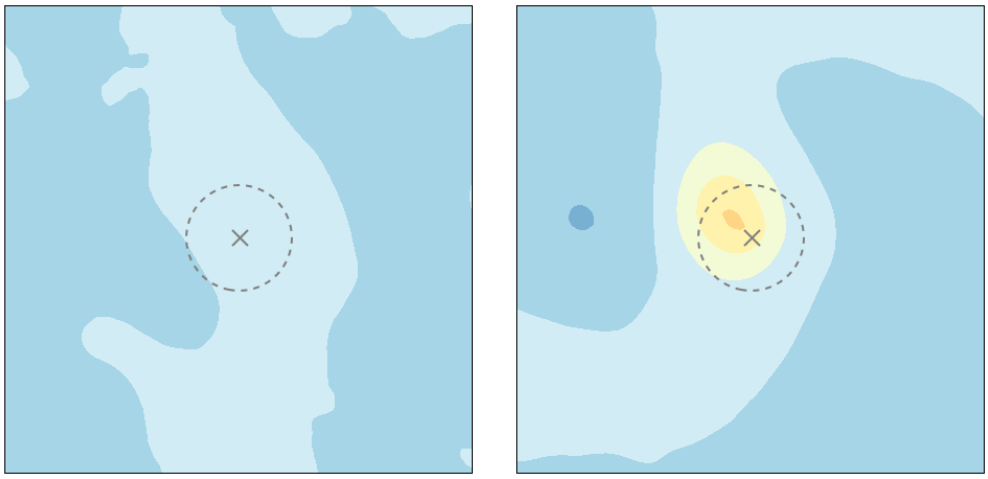

(a) class 3 **(b)** class 4

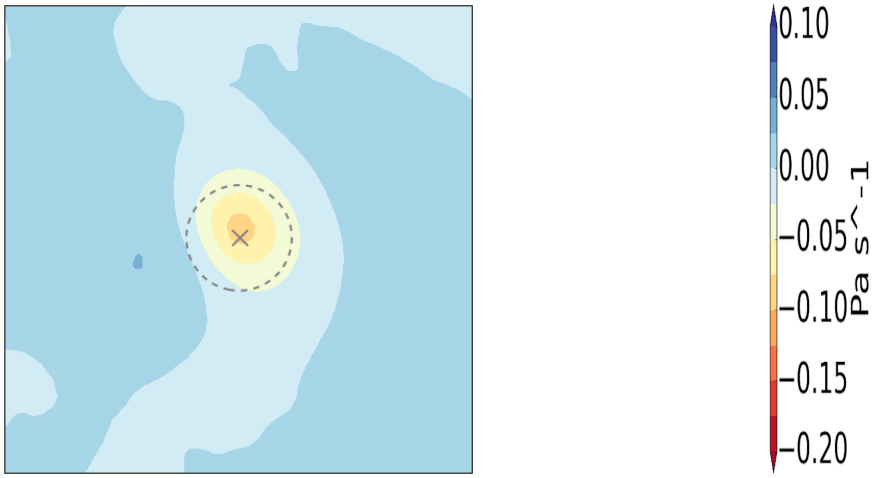

(c) class 5

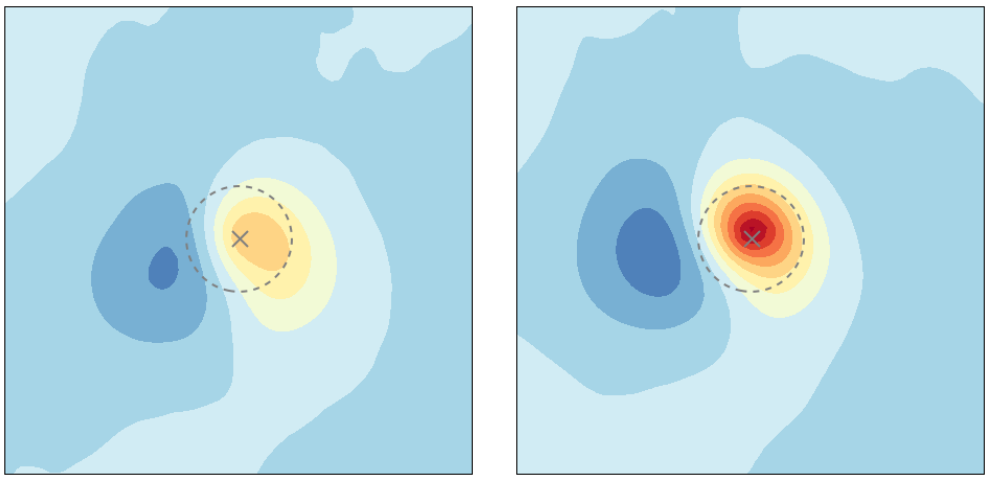

(d) class 1 **(e)** class 2

Figure D.6: $qg\omega_{top}$

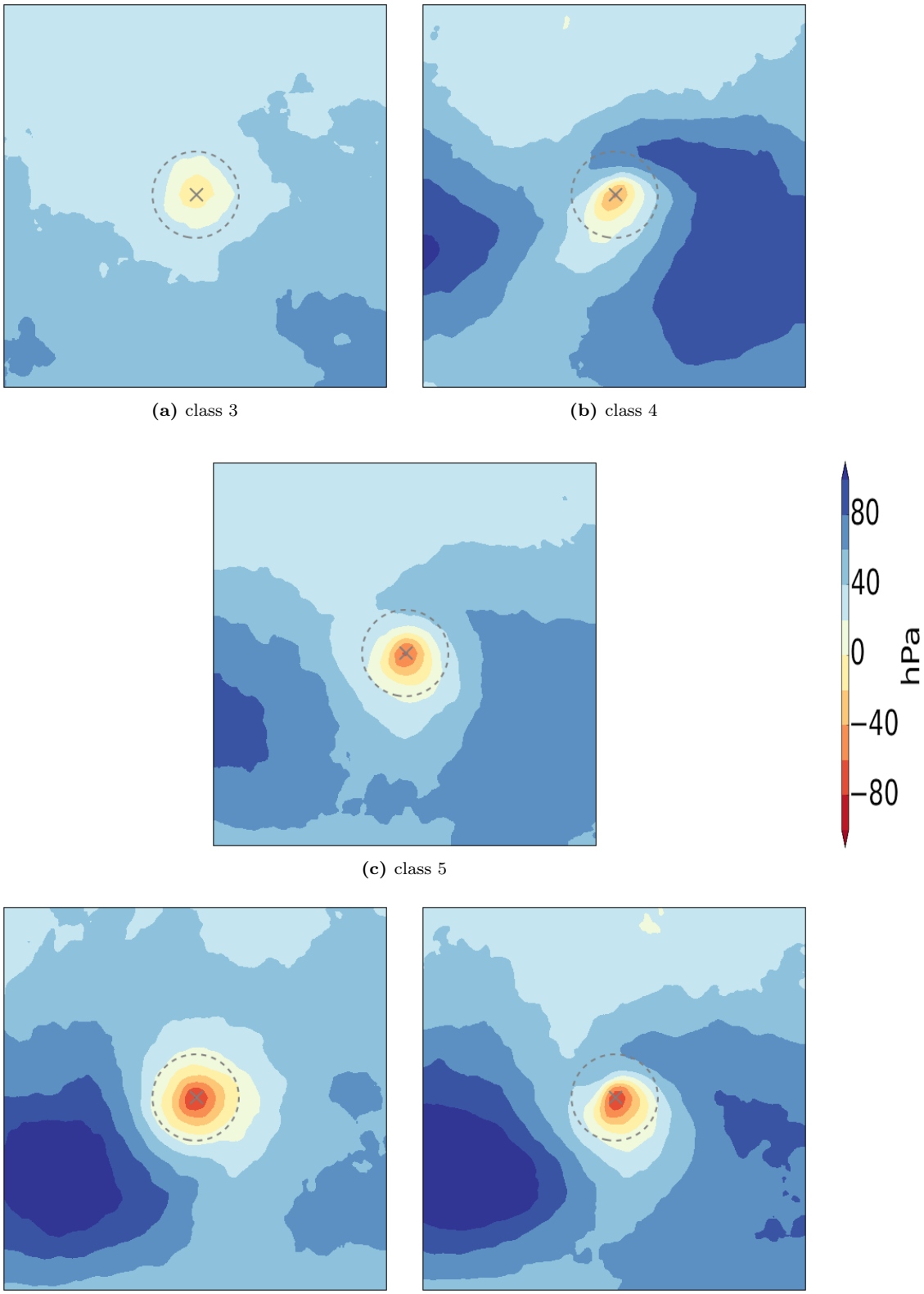

(a) class 3

(b) class 4

(c) class 5

(d) class 1

(e) class 2

Figure D.7: $TRAdP_{48}$

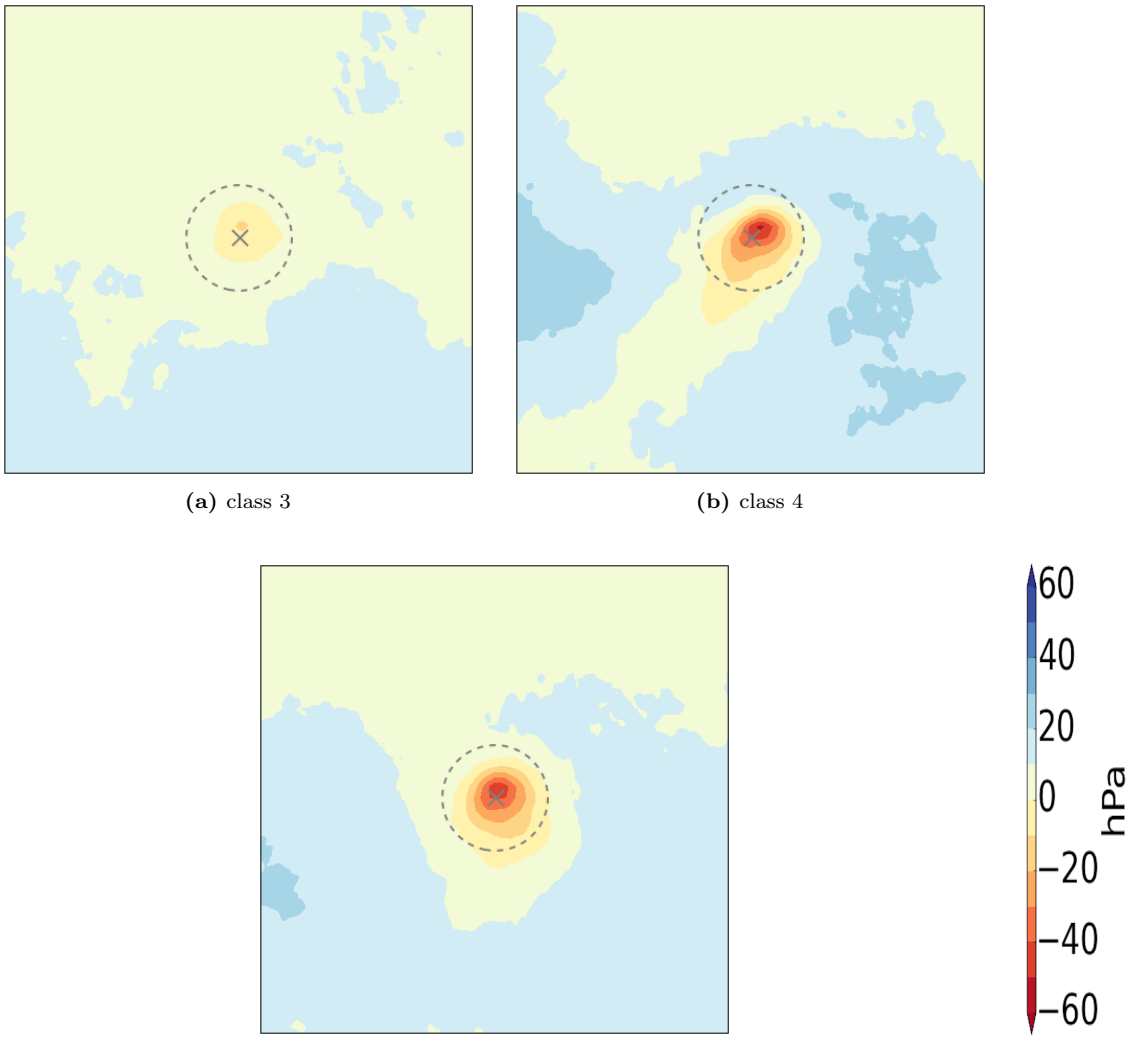

(a) class 3 **(b)** class 4

(c) class 5

(d) class 1 **(e)** class 2

Figure D.8: $TRAdP_{MX}$

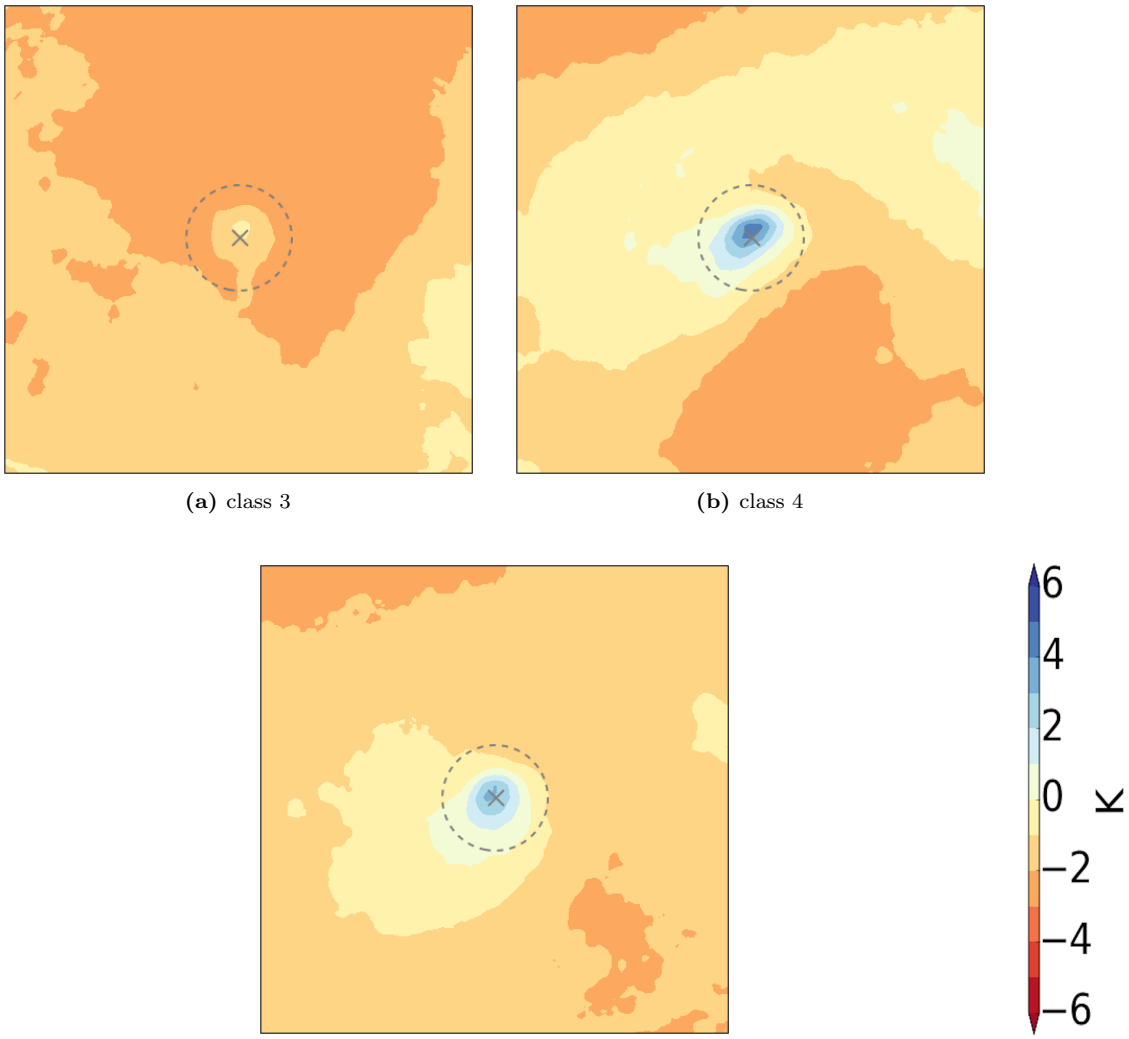

(a) class 3

(b) class 4

(c) class 5

(d) class 1

(e) class 2

Figure D.9: $TRAd\theta_{48}$

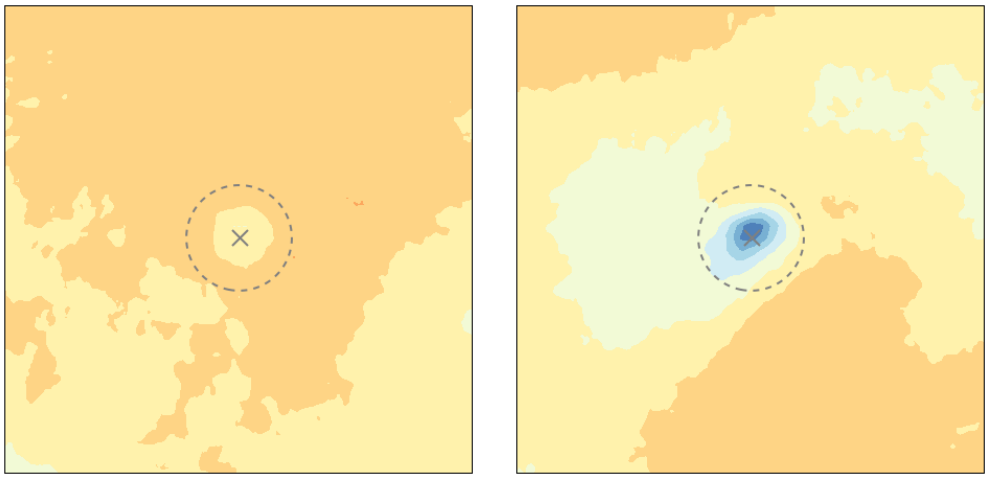

(a) class 3 **(b)** class 4

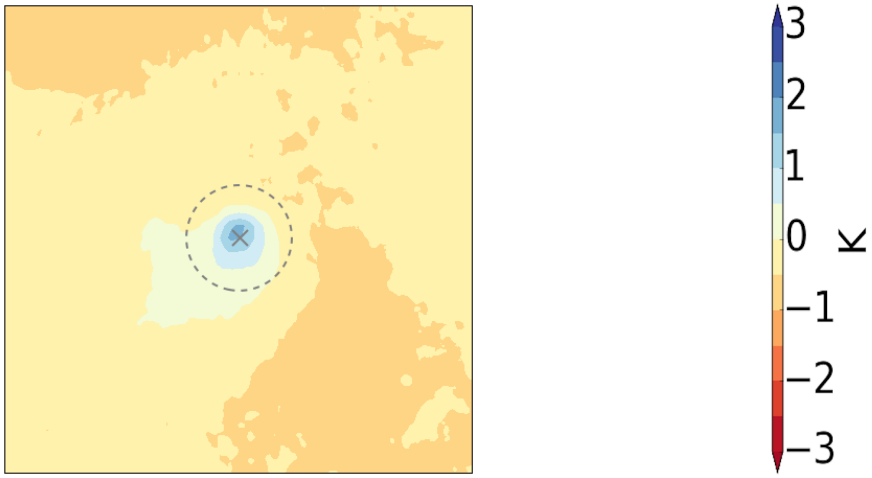

(c) class 5

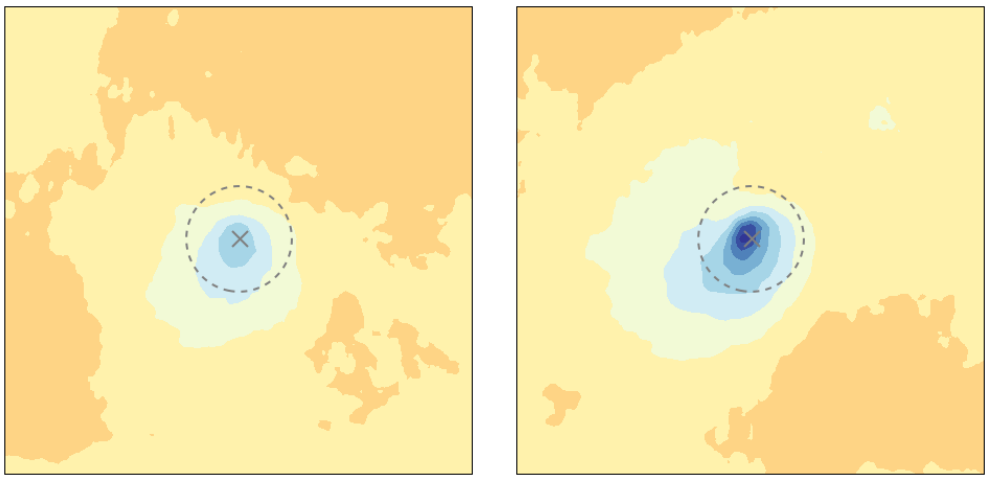

(d) class 1 **(e)** class 2

Figure D.10: $TRAd\theta_{MX}$

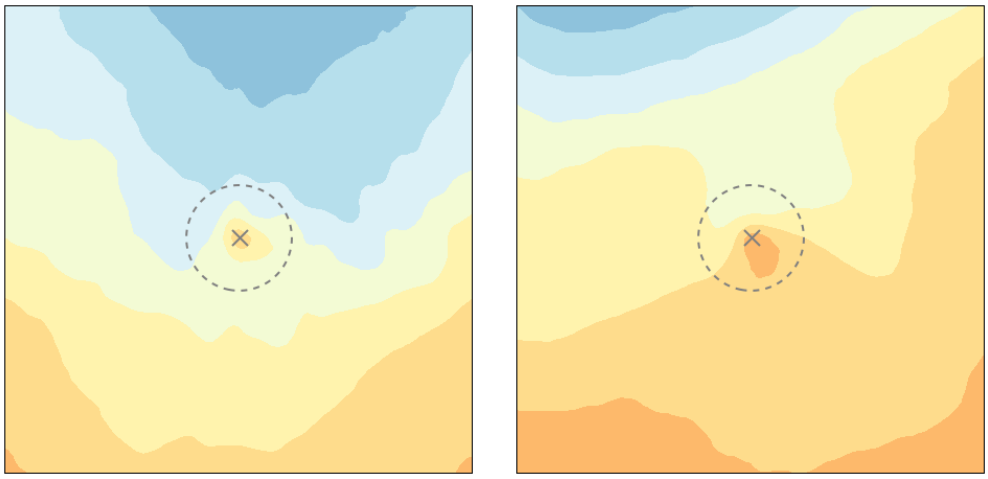

(a) class 3 **(b)** class 4

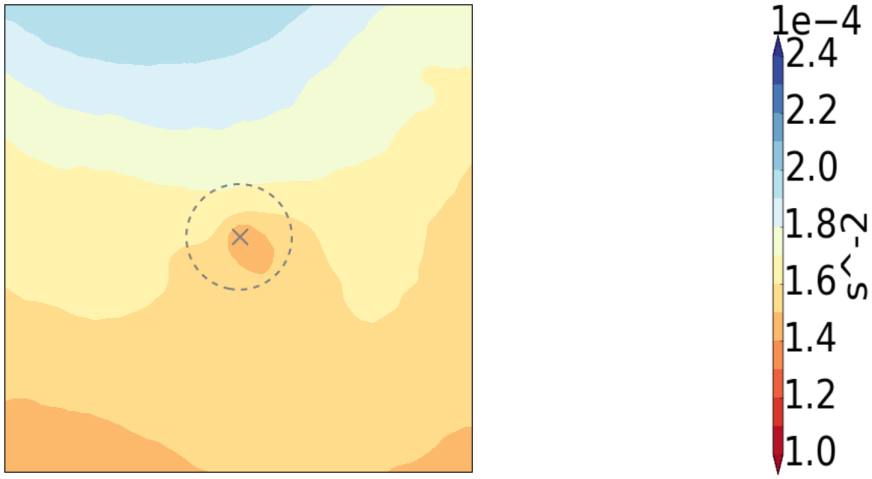

(c) class 5

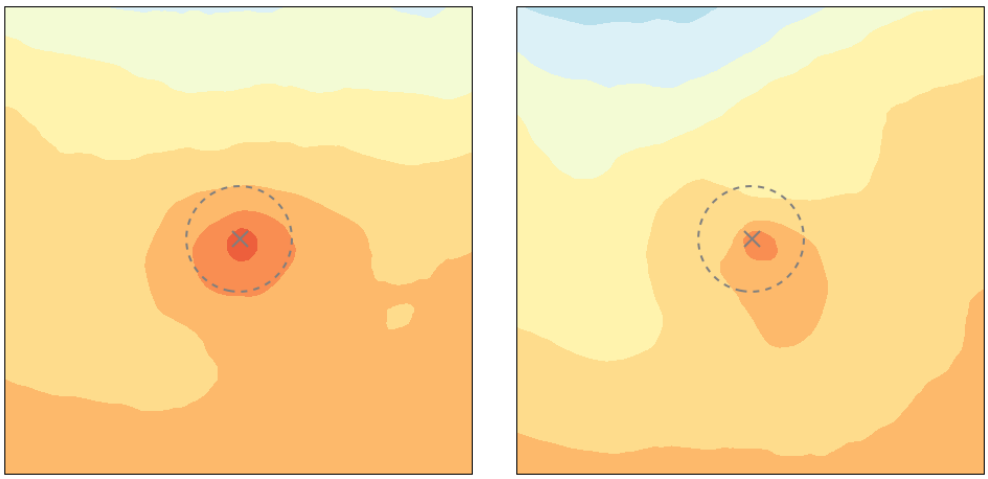

(d) class 1 **(e)** class 2

Figure D.11: N^2_{TROPO}

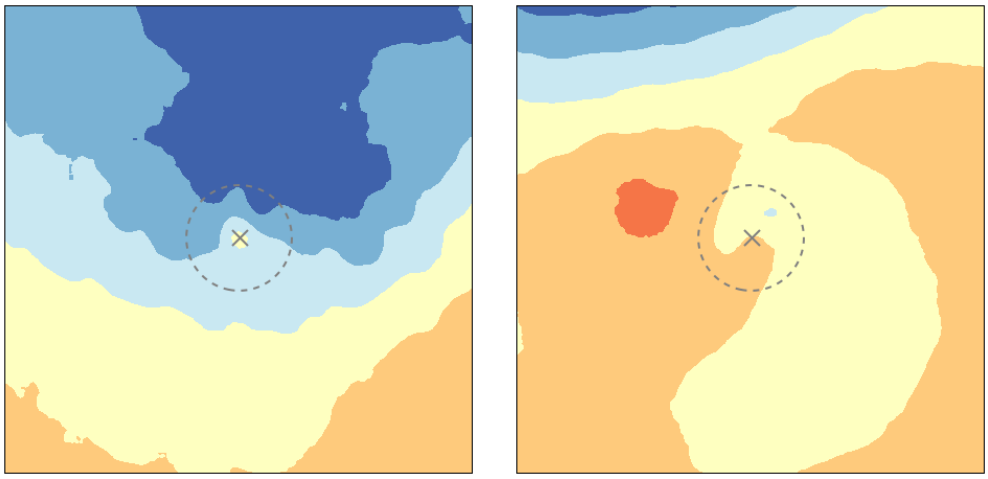

(a) class 3 **(b)** class 4

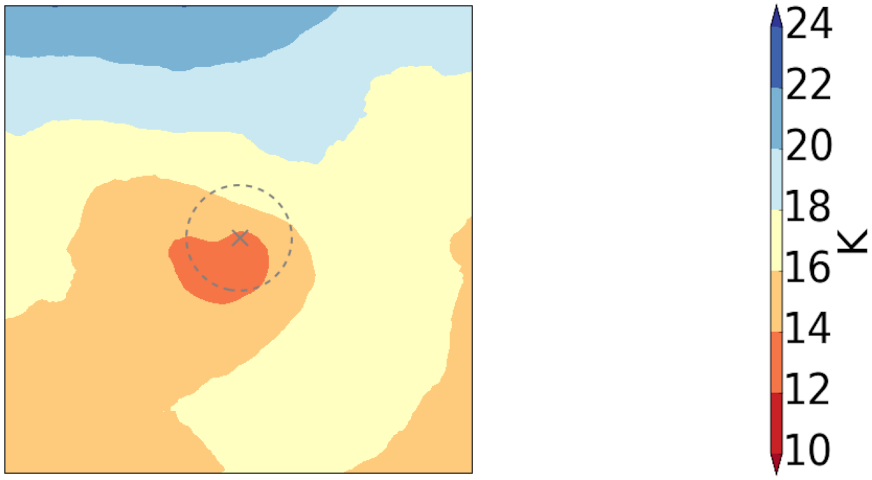

(c) class 5

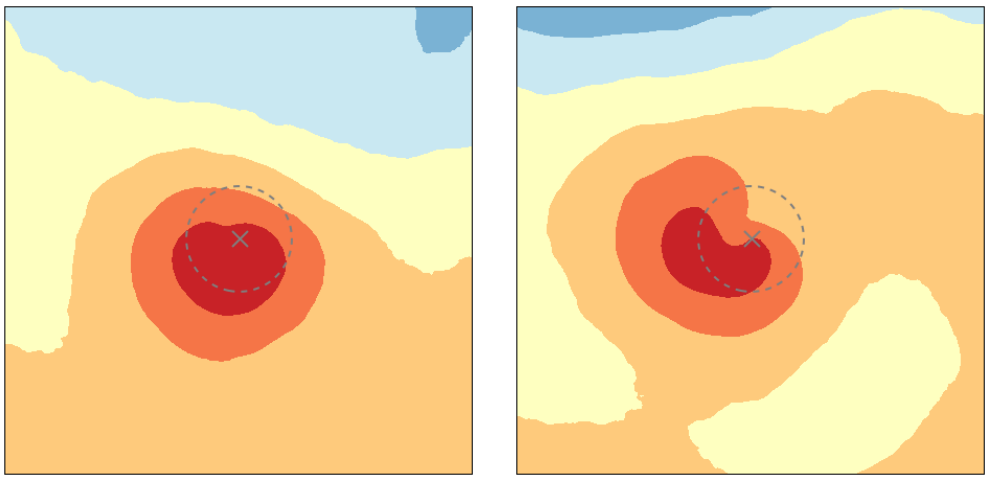

(d) class 1 **(e)** class 2

Figure D.12: *THDIFF*

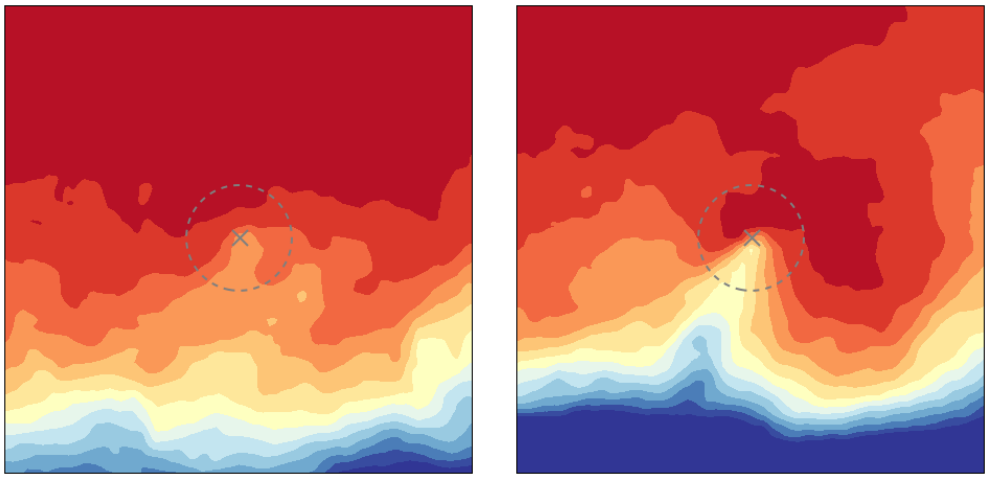

(a) class 3

(b) class 4

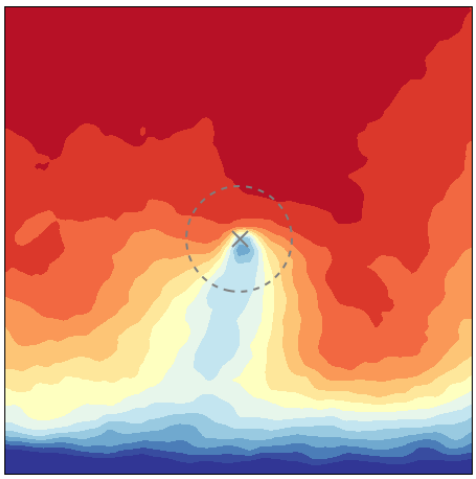

(c) class 5

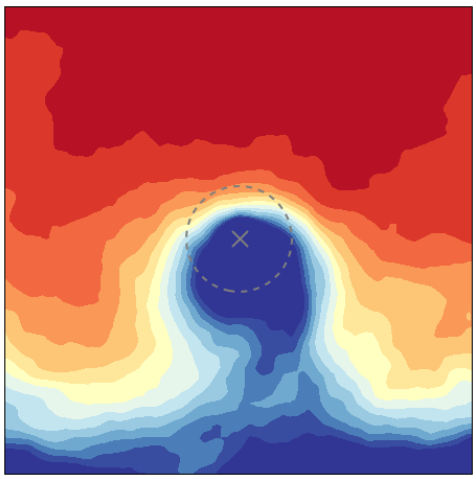

(d) class 1

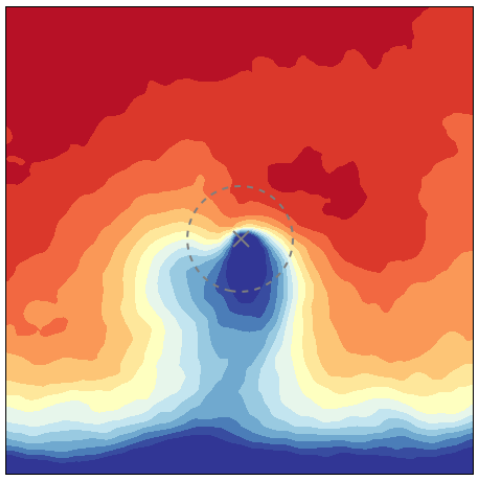

(e) class 2

Figure D.13: *CAPE*

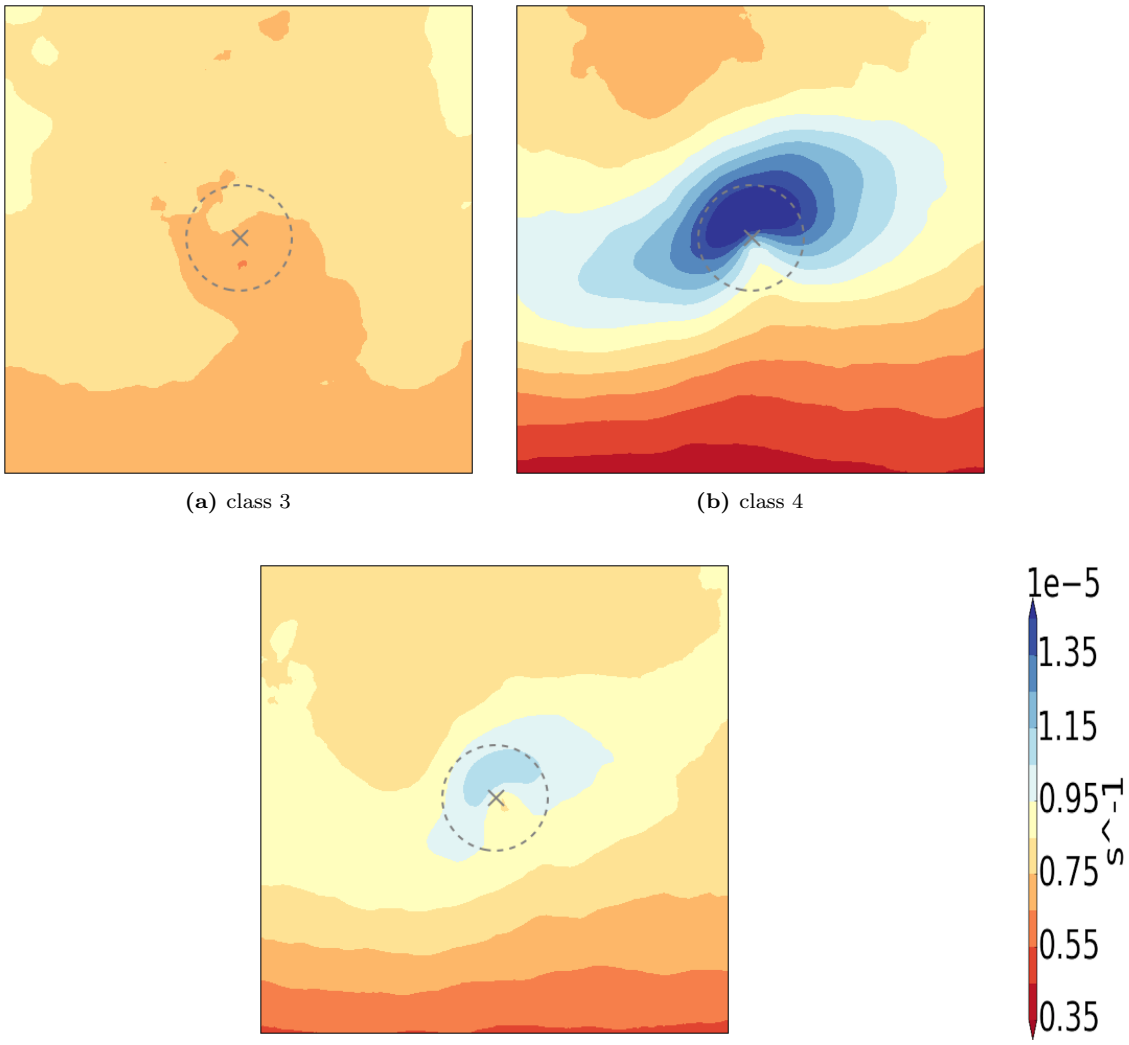

(a) class 3

(b) class 4

(c) class 5

(d) class 1

(e) class 2

Figure D.14: *EADY*

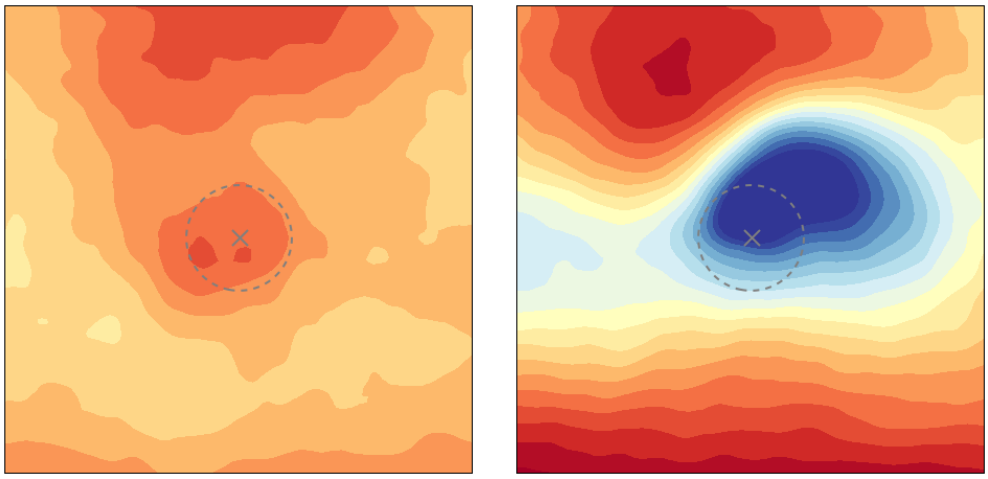

(a) class 3 **(b)** class 4

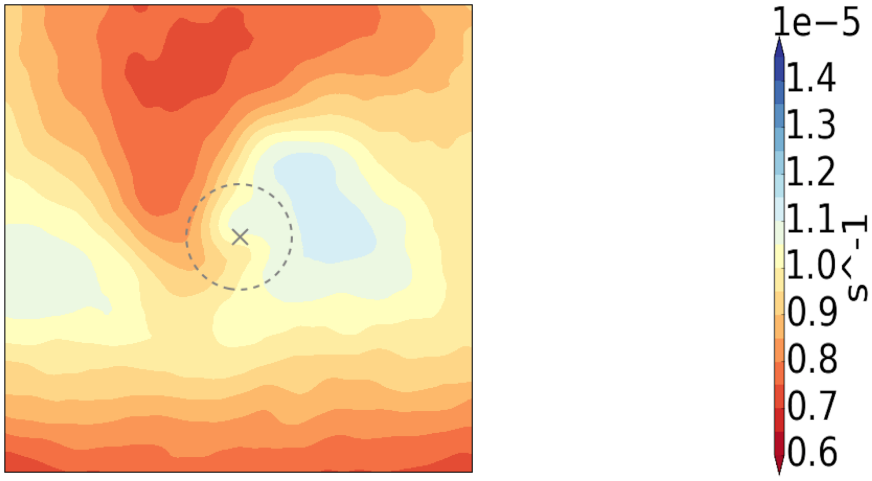

(c) class 5

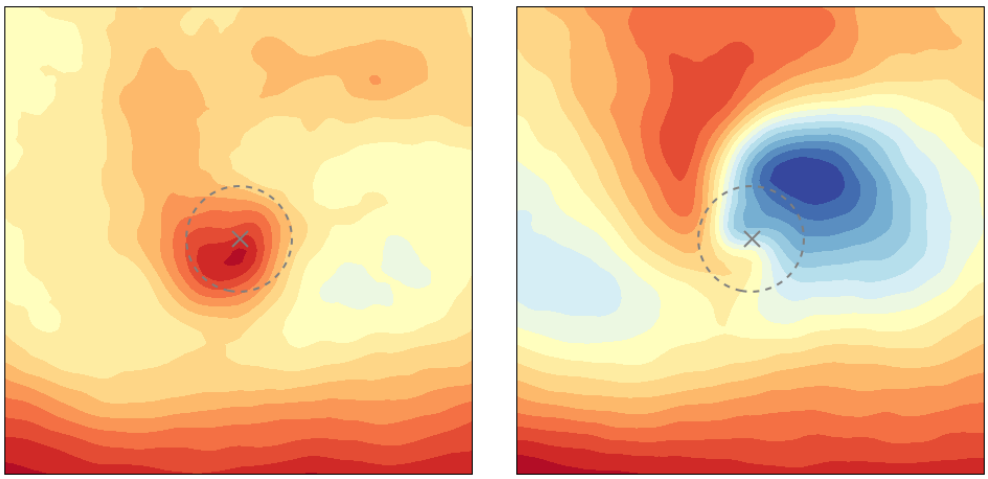

(d) class 1 **(e)** class 2

Figure D.15: $EADY_{up}$

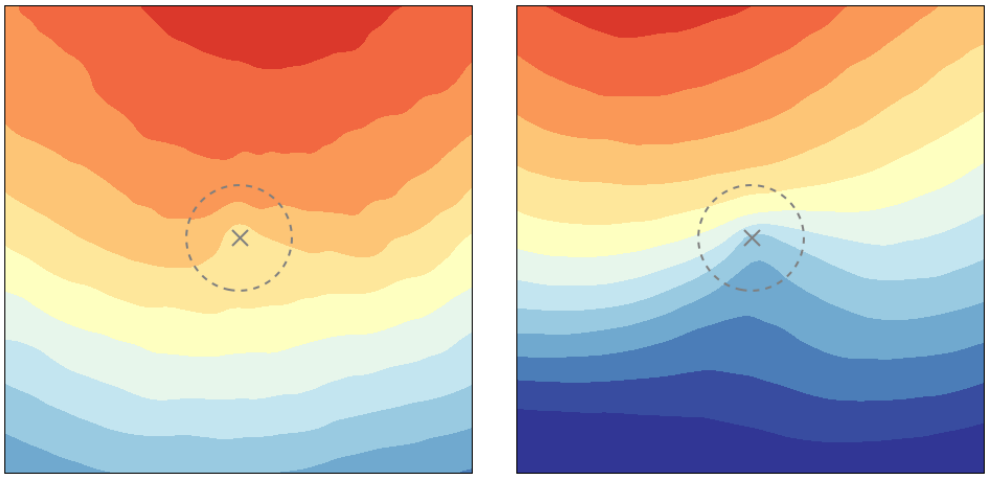

(a) class 3 **(b)** class 4

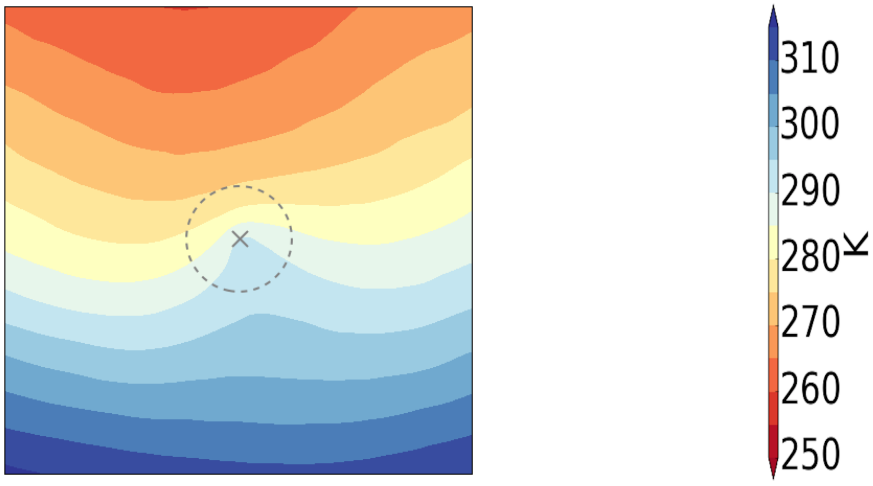

(c) class 5

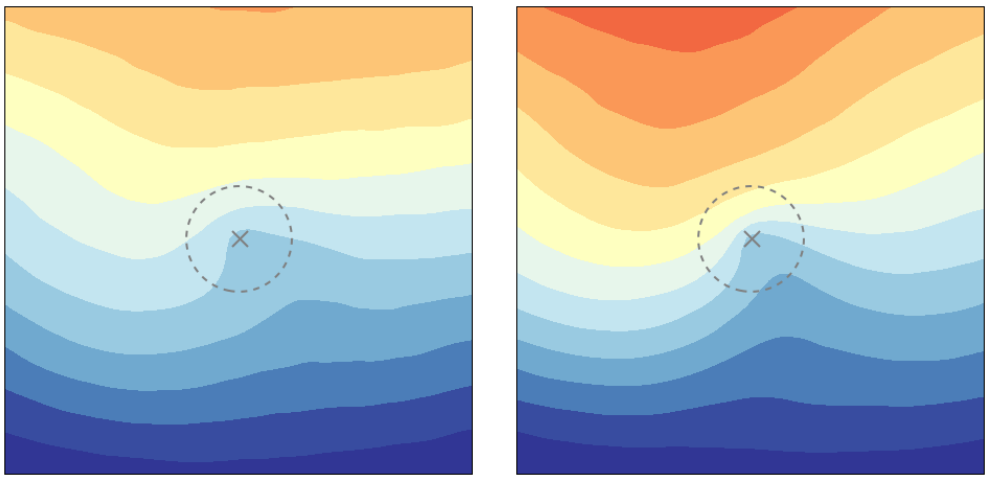

(d) class 1 **(e)** class 2

Figure D.16: θ_{e850}

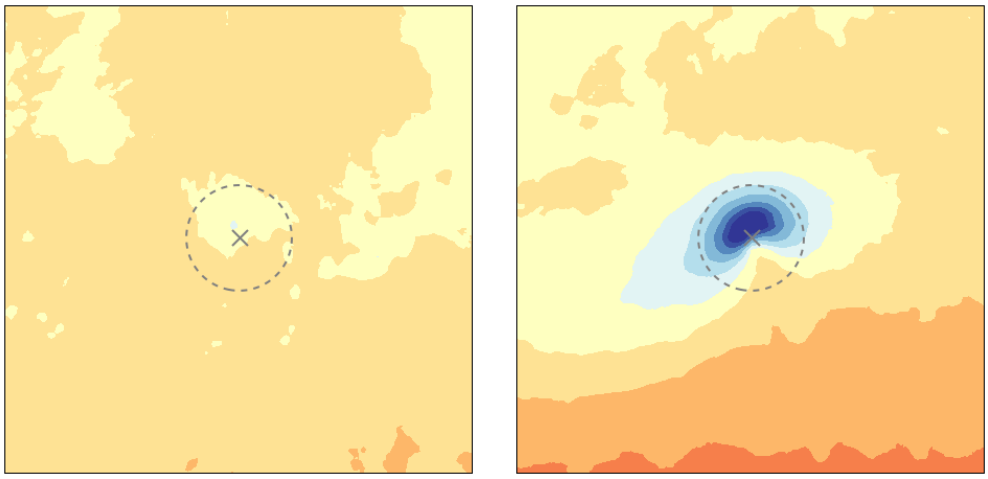

(a) class 3 **(b)** class 4

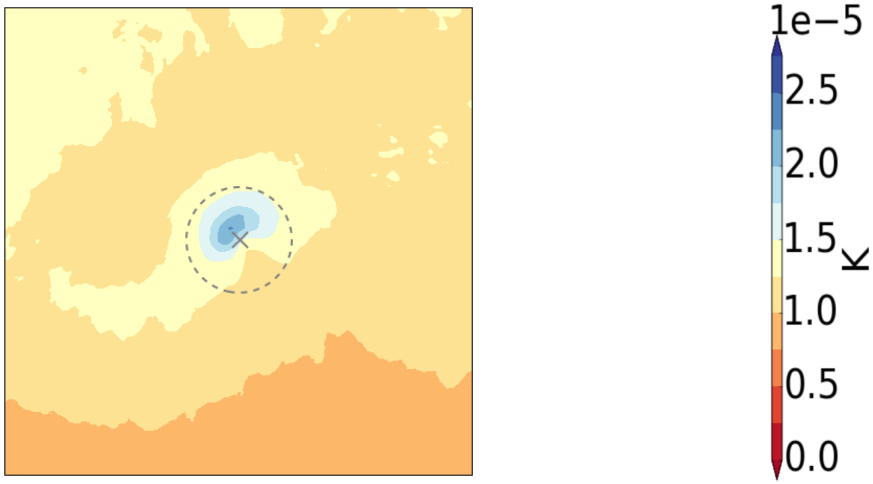

(c) class 5

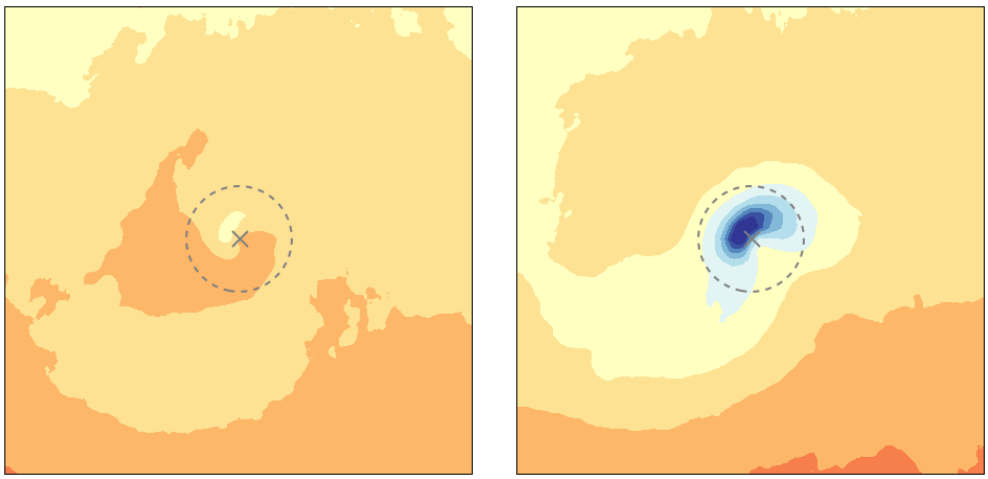

(d) class 1 **(e)** class 2

Figure D.17: $|\Delta\theta_{850}|$

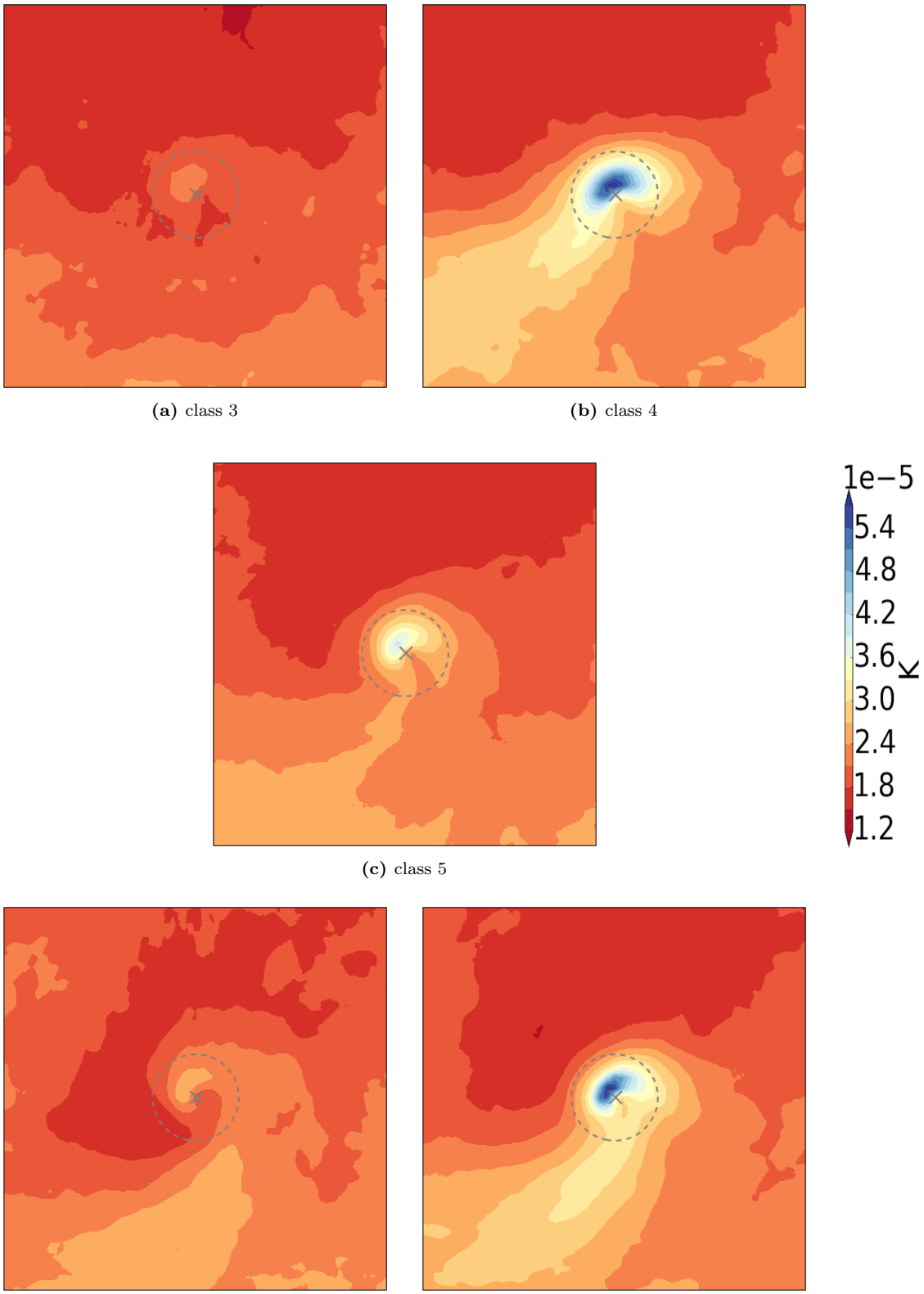

(a) class 3

(b) class 4

(c) class 5

(d) class 1

(e) class 2

Figure D.18: $|\Delta\theta_{e850}|$

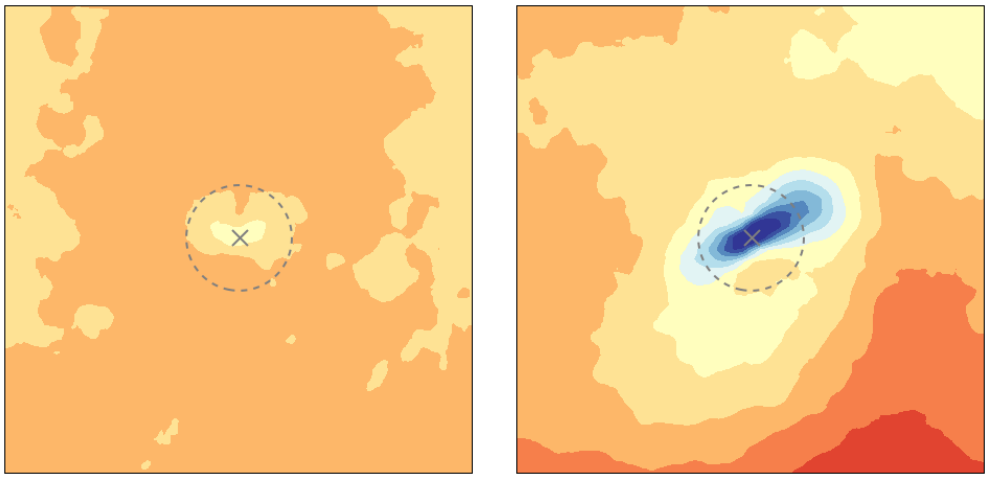

(a) class 3 **(b)** class 4

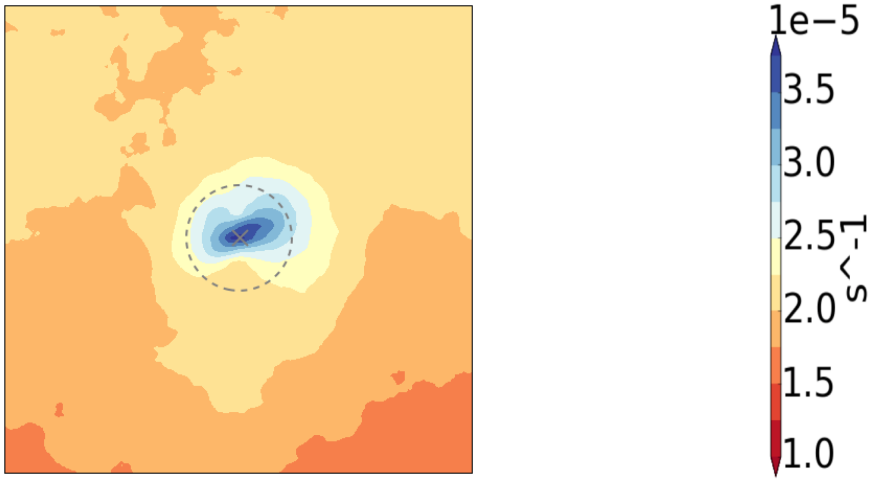

(c) class 5

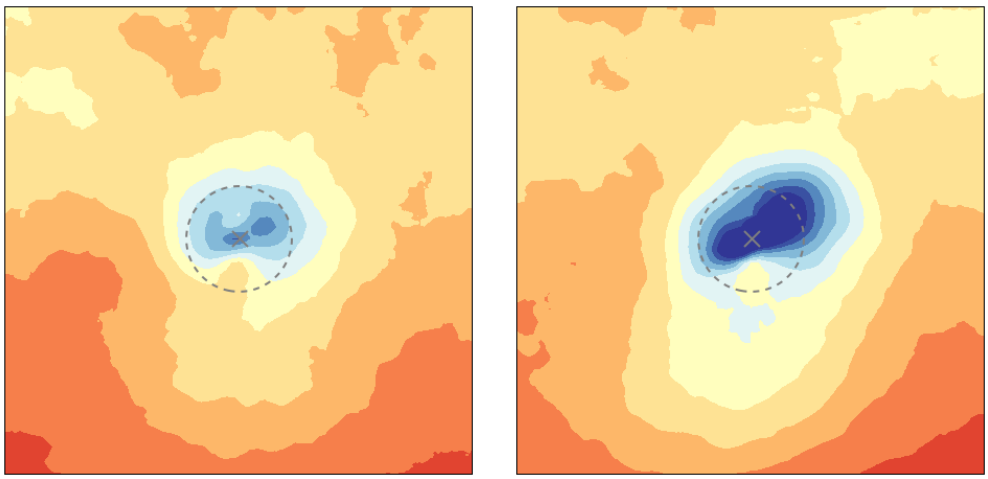

(d) class 1 **(e)** class 2

Figure D.19: *DEF*

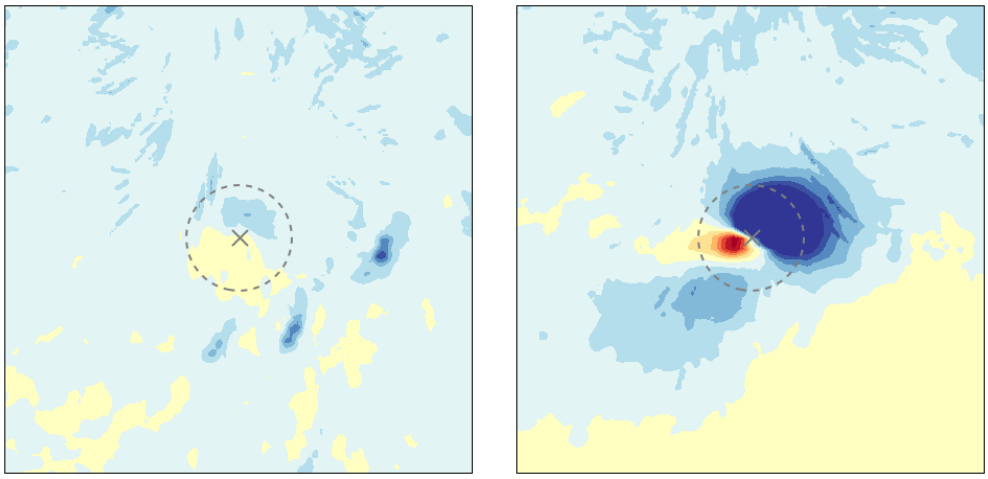

(a) class 3 **(b)** class 4

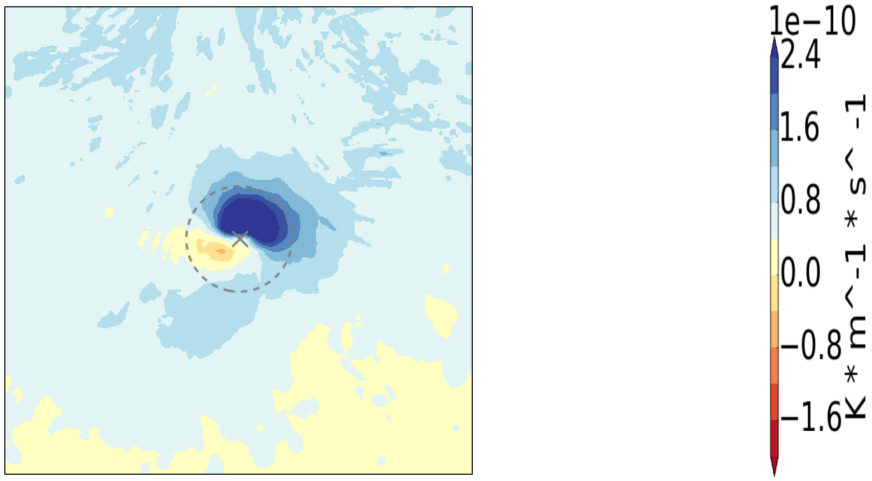

(c) class 5

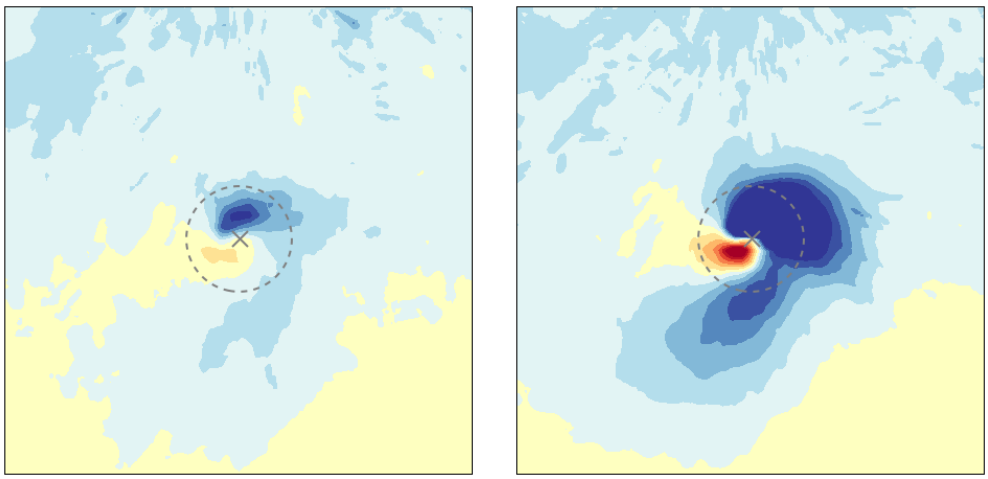

(d) class 1 **(e)** class 2

Figure D.20: $FGEN_{850}$

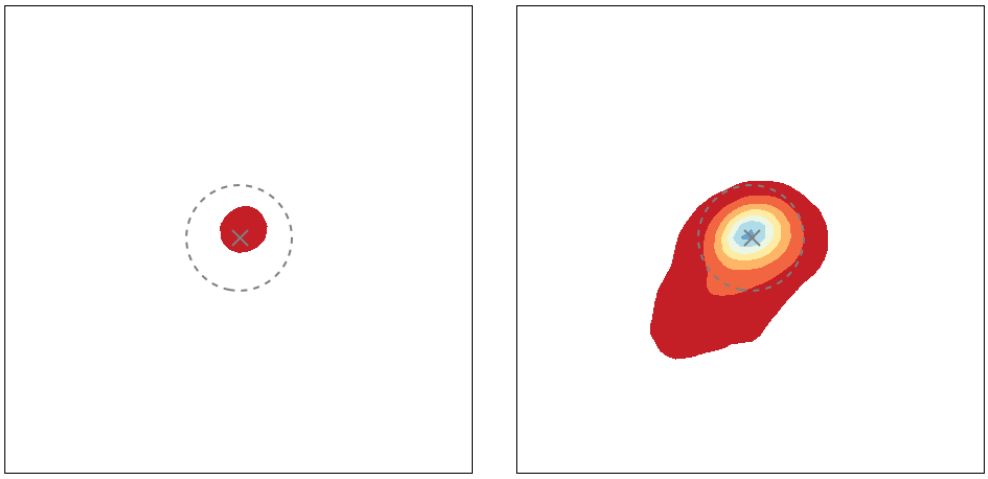

(a) class 3 **(b)** class 4

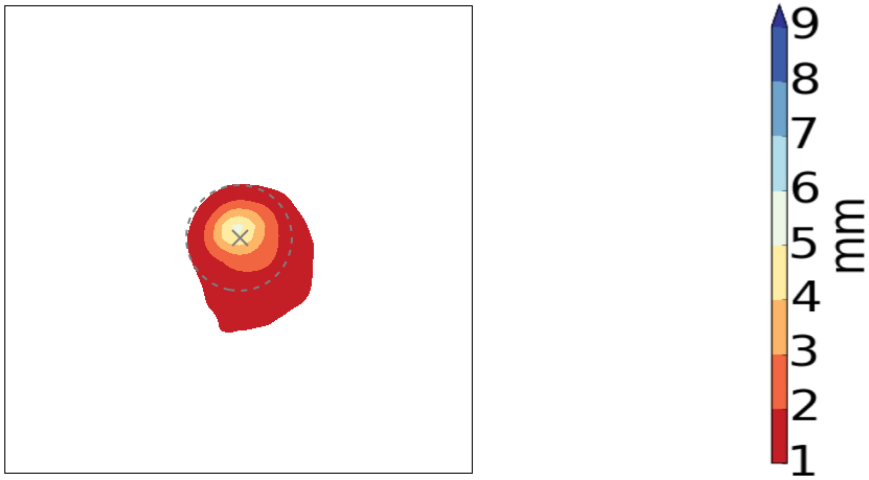

(c) class 5

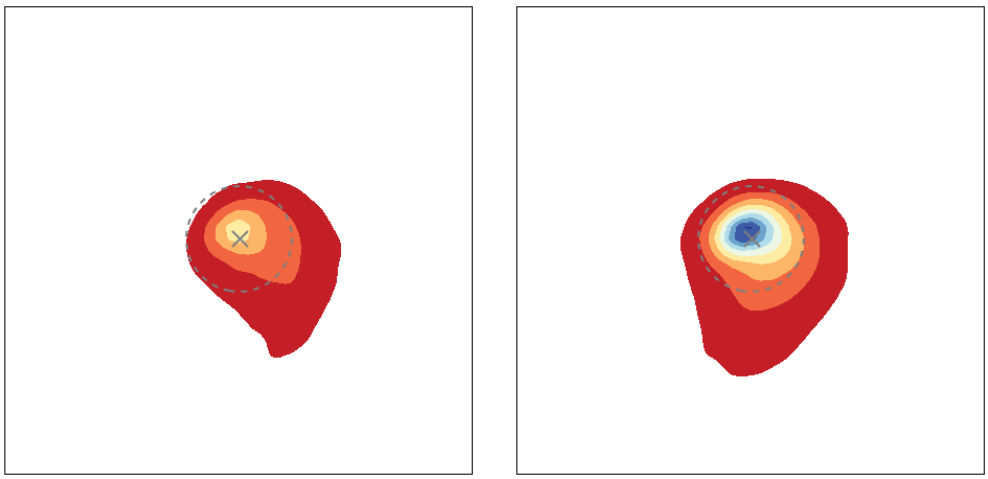

(d) class 1 **(e)** class 2

Figure D.21: RR_{6h}

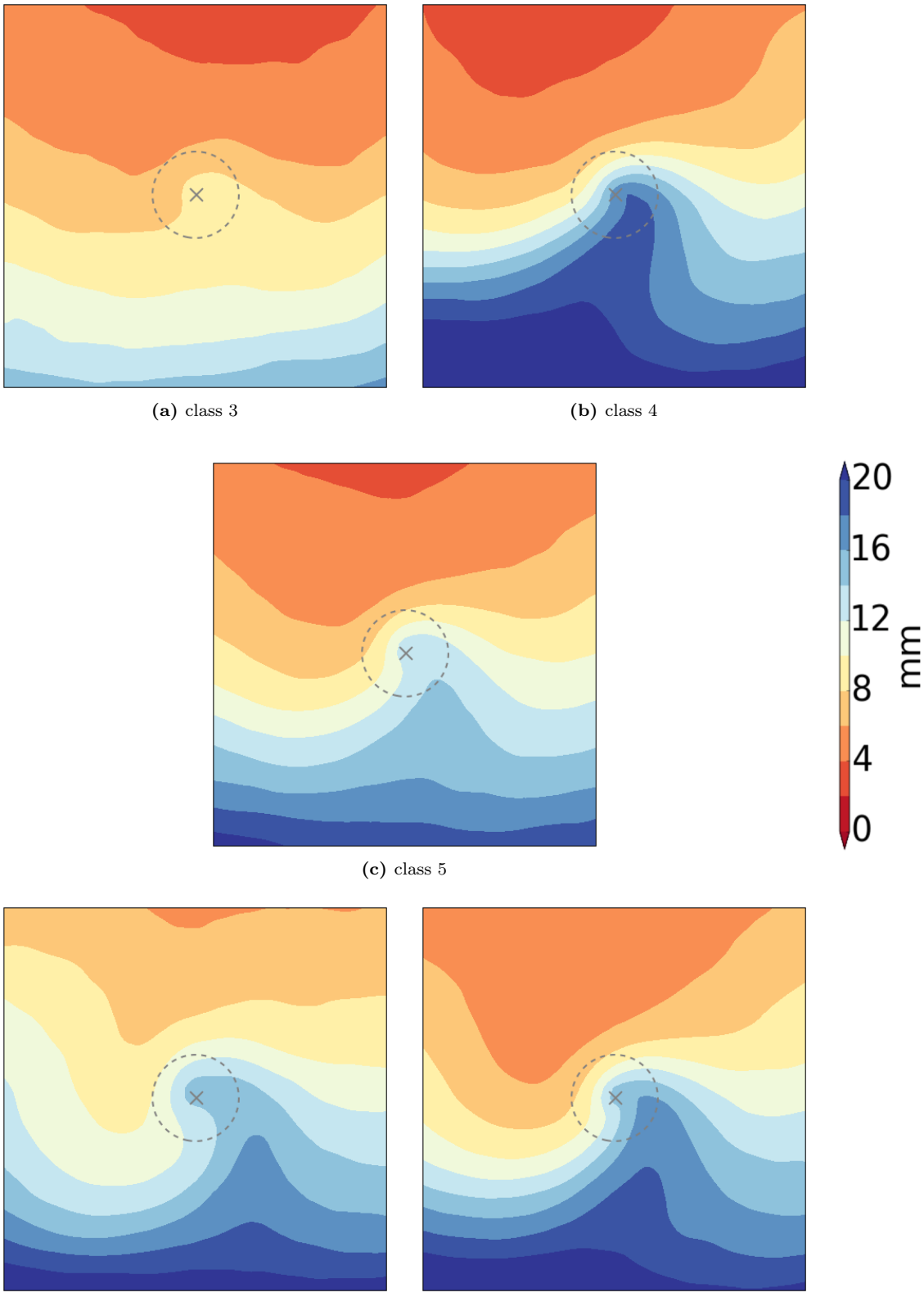

(a) class 3

(b) class 4

(c) class 5

(d) class 1

(e) class 2

Figure D.22: Q_{int}

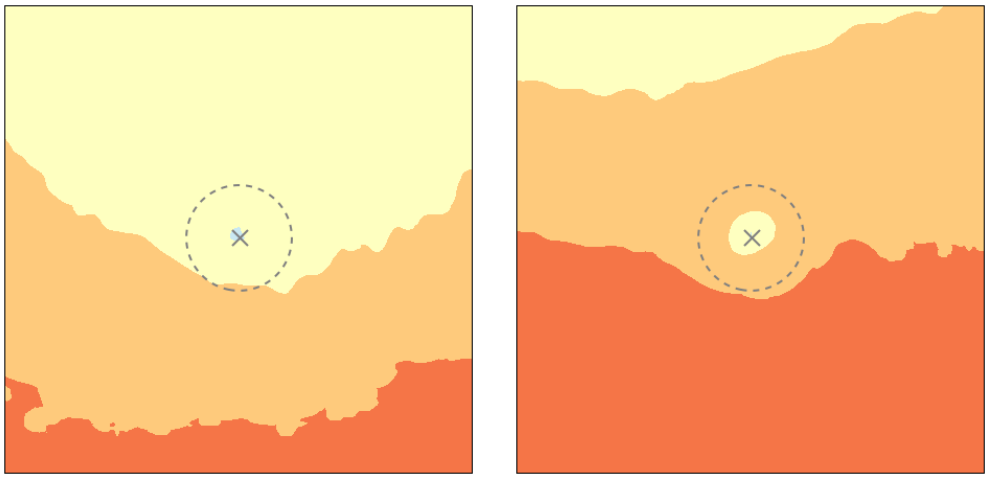

(a) class 3 **(b)** class 4

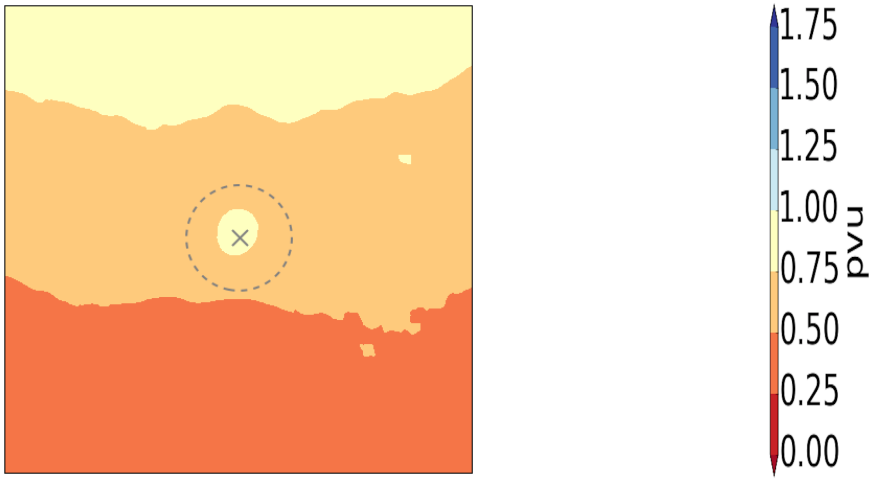

(c) class 5

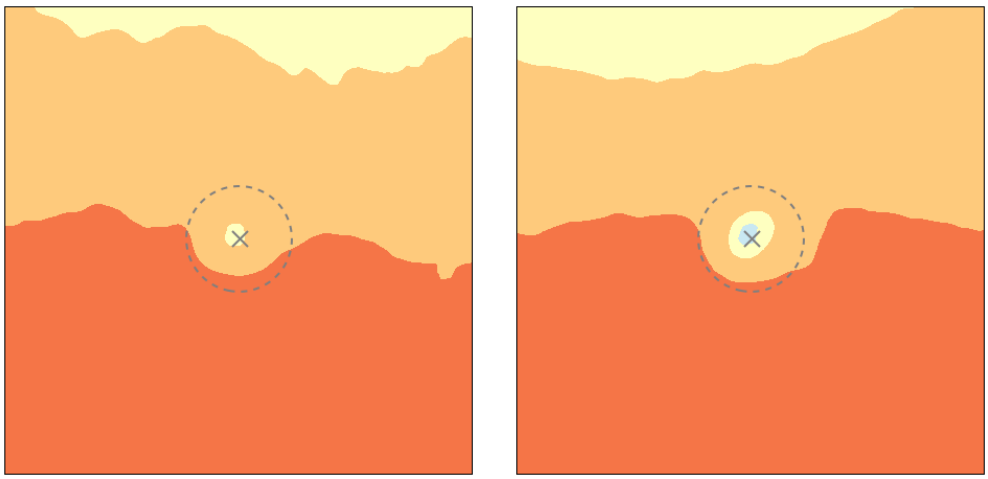

(d) class 1 **(e)** class 2

Figure D.23: PV_{low}

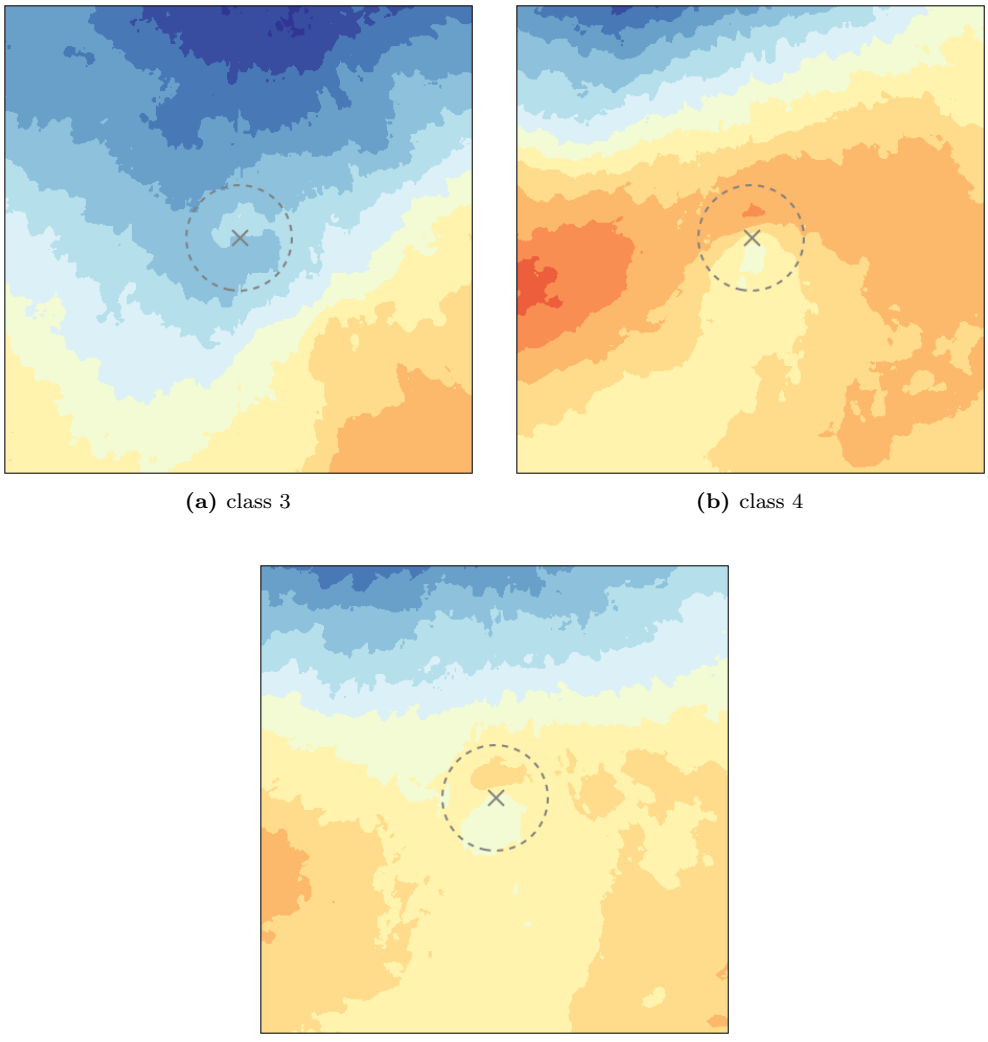

(a) class 3 **(b)** class 4

(c) class 5

(d) class 1 **(e)** class 2

Figure D.24: *UPTTIM*

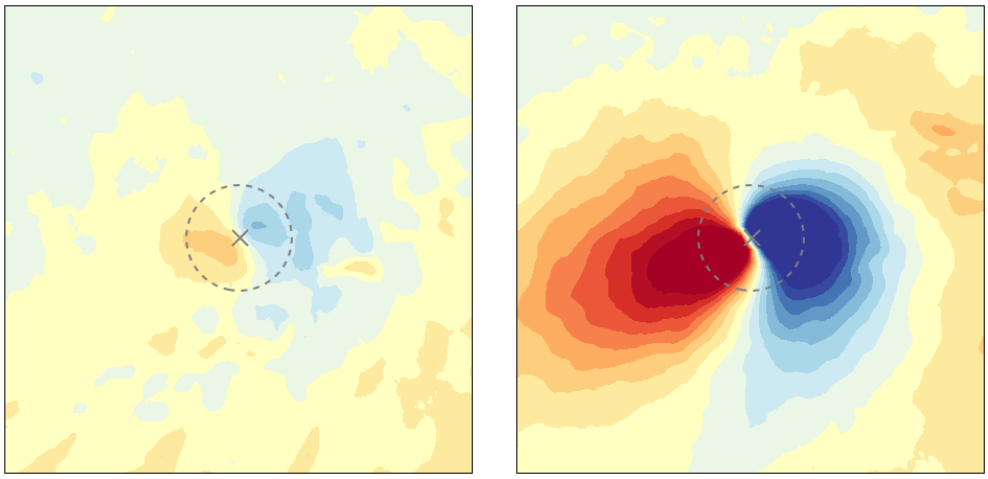

(a) class 3 **(b)** class 4

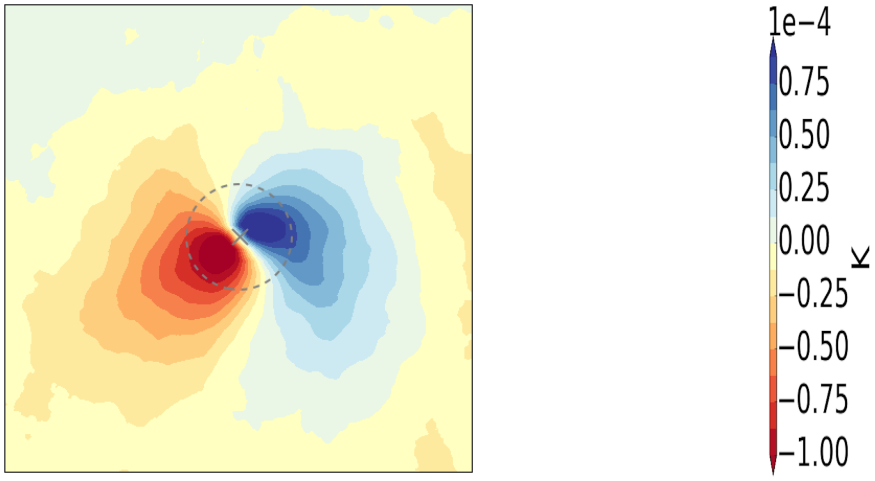

(c) class 5

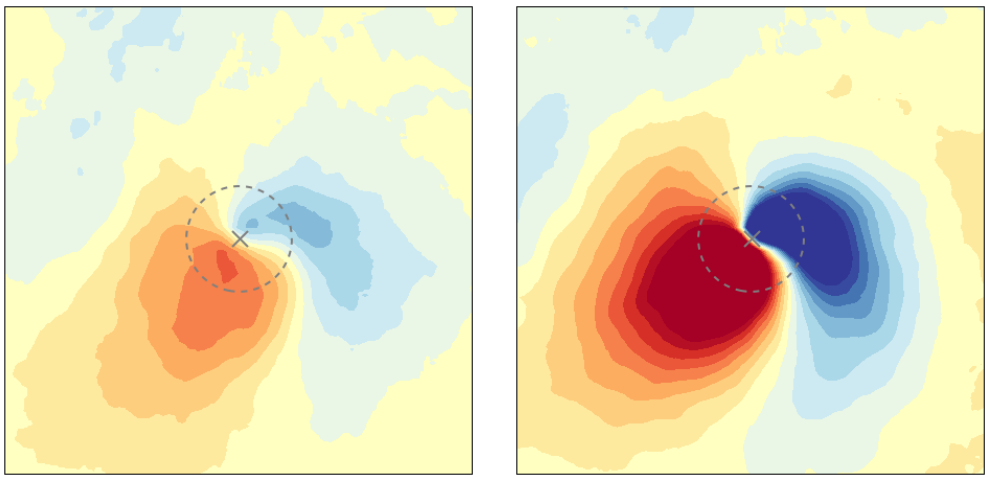

(d) class 1 **(e)** class 2

Figure D.25: T_{ADV850}

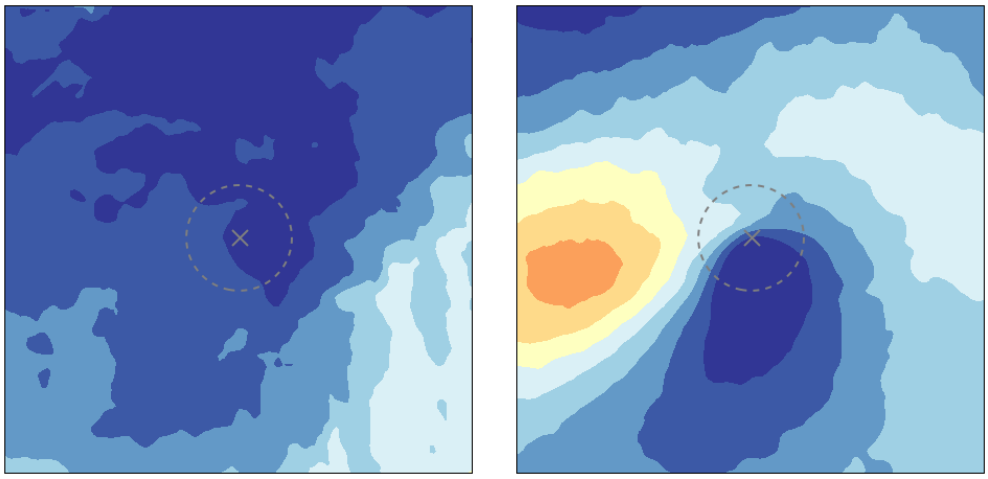

(a) class 3 **(b)** class 4

(c) class 5

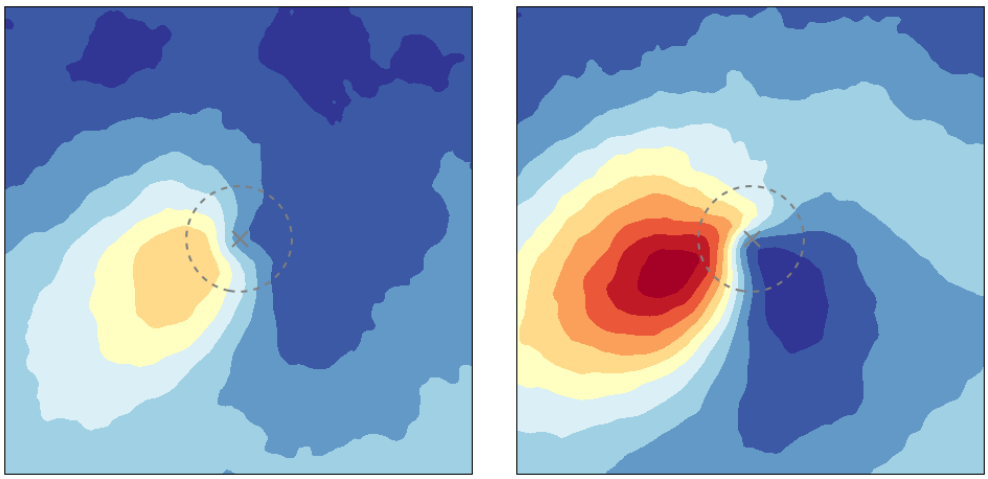

(d) class 1 **(e)** class 2

Figure D.26: *SSHF*

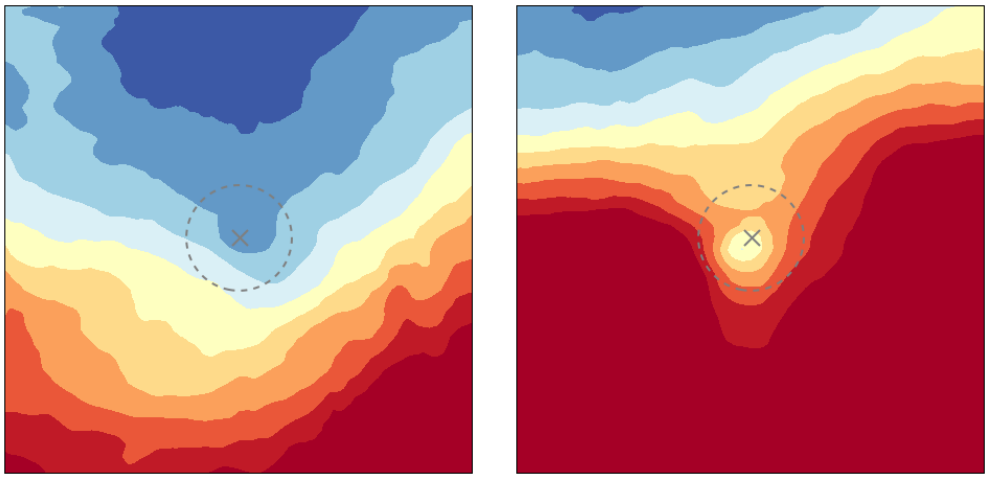

(a) class 3 **(b)** class 4

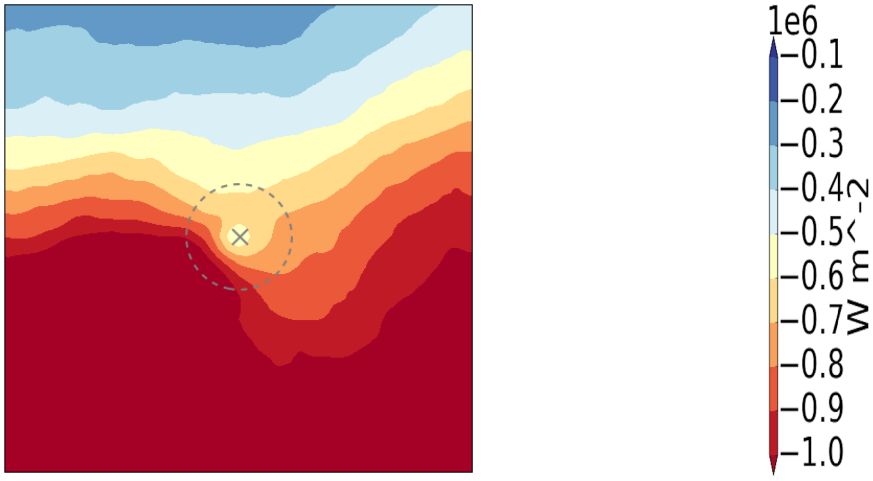

(c) class 5

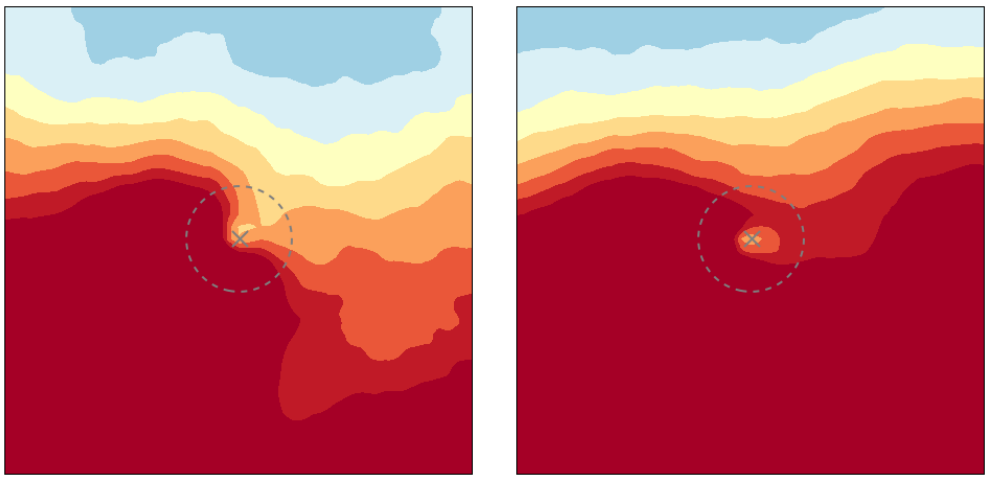

(d) class 1 **(e)** class 2

Figure D.27: *SLHF*

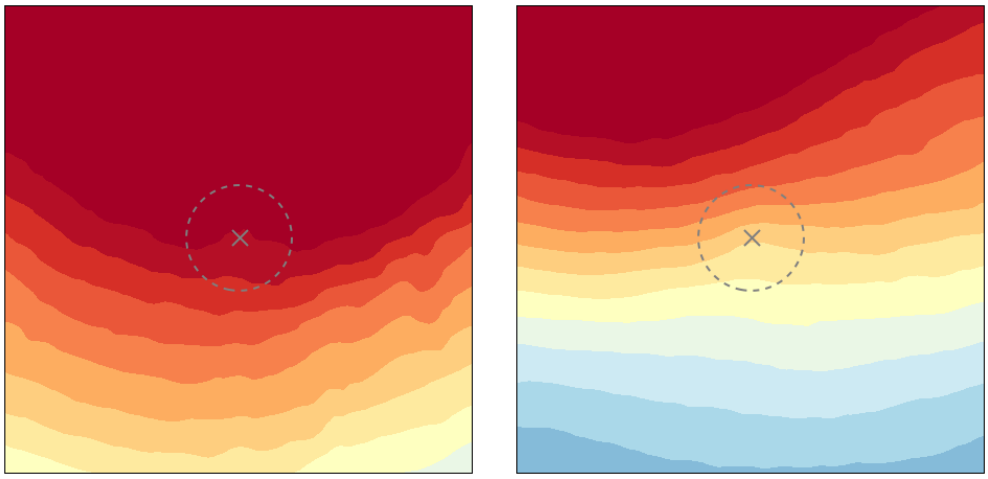

(a) class 3 **(b)** class 4

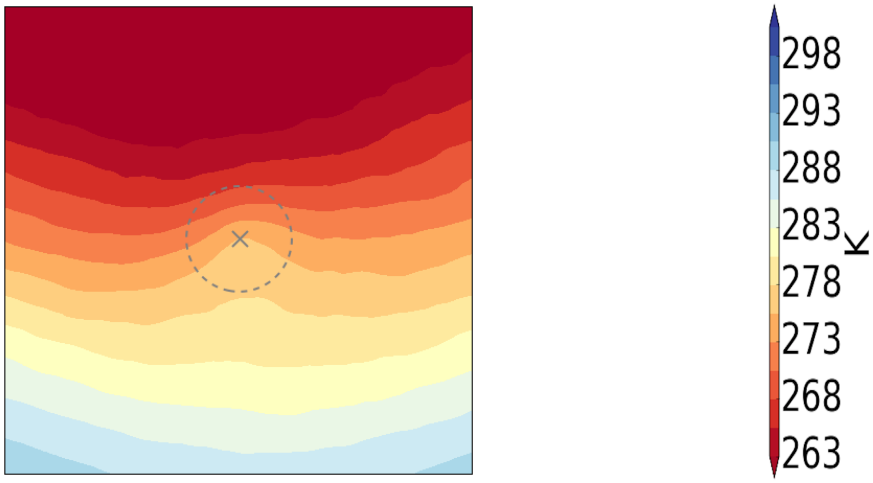

(c) class 5

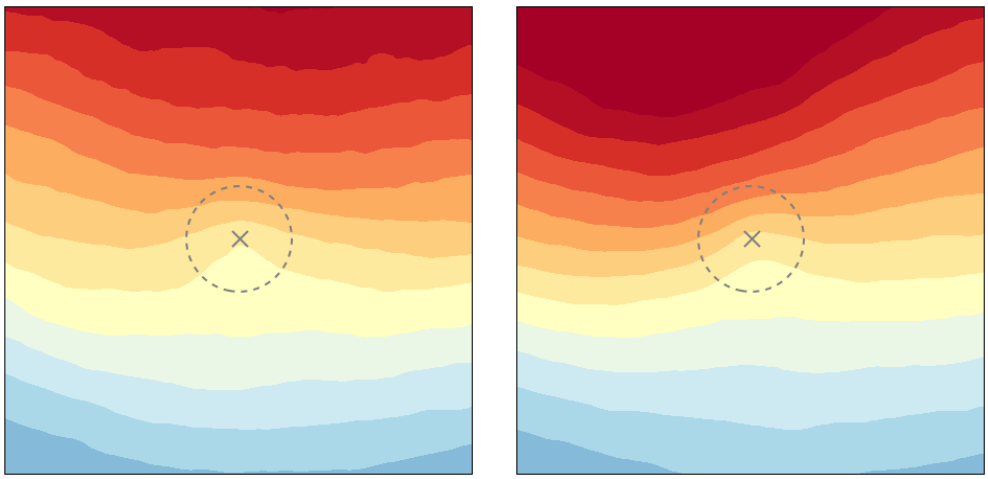

(d) class 1 **(e)** class 2

Figure D.28: *SKT*

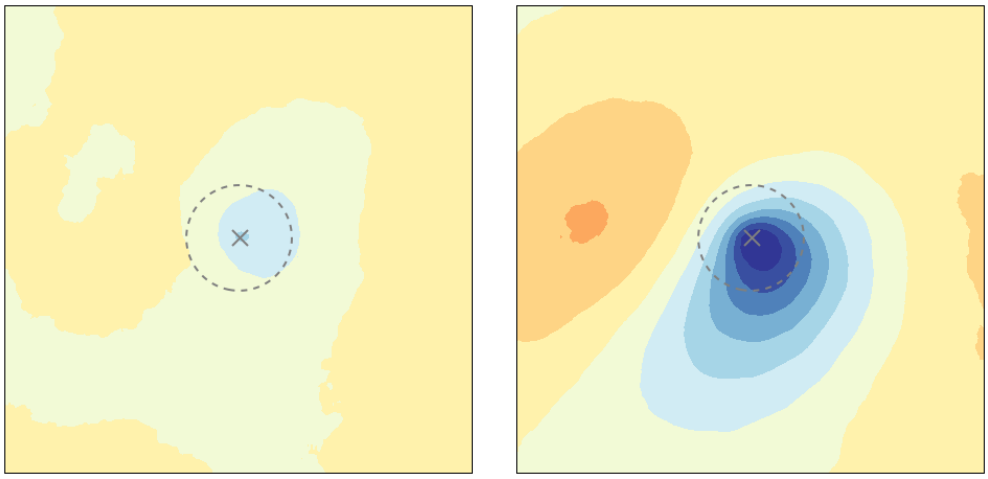

(a) class 3 **(b)** class 4

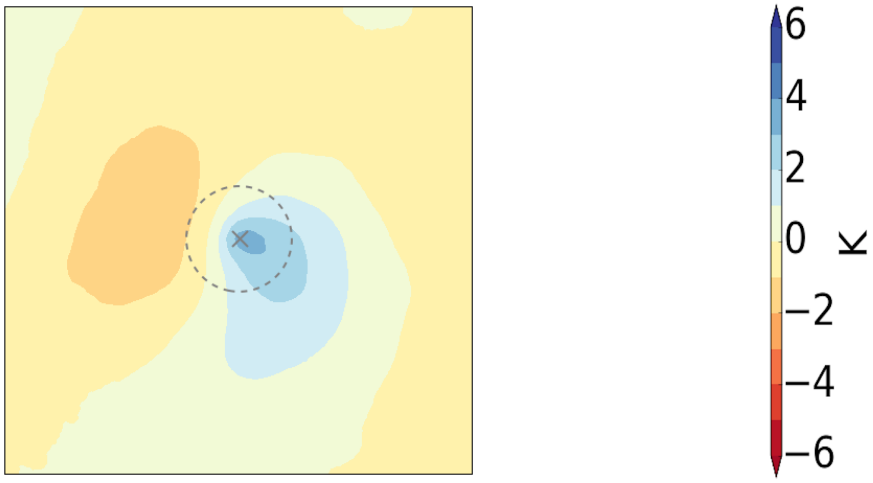

(c) class 5

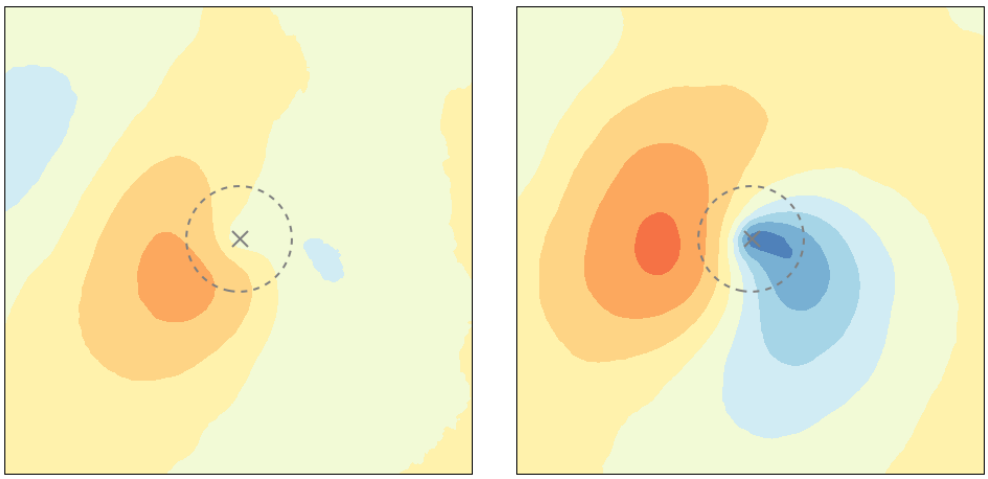

(d) class 1 **(e)** class 2

Figure D.29: T_{PERT}

Appendix E

Sensitivity on time of PMI

In the text, PMI is defined as the point to represent the phase of maximum intensification along a cyclone track. For 1691 ETCs this corresponds to the same number of PMIs. However, the analysis in chapters 4 5 considered not only these time instances, but also the time instances -12 h, -6 h, +6 h, +12 h around the PMI. This results in 8455 time instances and locations considered. Hence, strictly speaking the biplot, the histograms and composites discussed in this thesis do not perfectly match with the PMI. However, including these neighboring times steps allows the statistical analysis to be somewhat more robust.
This appendix investigates further how the results based on the 8455 instances change if only the strictly 1691 PMIs are taken into account. Figure E.1 shows the biplot produced with the same methods described in Chap: 2, but only for the PMIs. The first four principal components explain 64.9 % of the variance in the data set, see Tab: E.1. Again, a varimax rotation was applied to get a more physically meaningful classification. The percentage explained by each of the rotated components is shown in Tab: E.2. The new components 2 and 3 together explain most of the variance 38.5 % and hence are plotted in Fig: E.1.

Table E.1: Explained vatriance for the first 4 principle components [%] of PMI-data points only

prin. comp.	**expl. var. [%]**
pc1	29.47
pc2	18.86
pc3	9.42
pc4	7.16
pc1−c4	64.90

Table E.2: Explained vatriance for the first 4 rotated components [%] of PMI-data points only

rot. comp.	**expl. var. [%]**
c1	14.52
c2	20.83
c3	17.71
c4	11.85
c1−c4	64.90

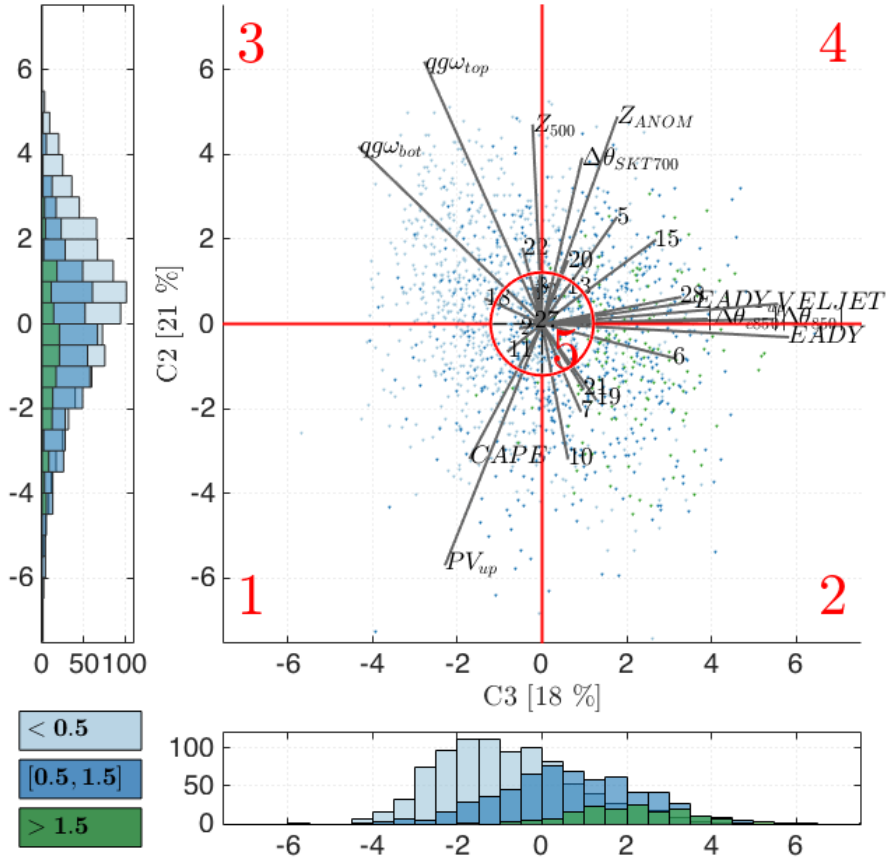

#	parameter
2	PV_{low}
5	N^2_{TROPO}
6	$FGEN_{850}$
7	DEF
8	Q_{int}
10	RR_{6h}
11	SKT
12	$SLHF$
13	$SSHF$
15	T_{PERT}
18	$UPTTIM$
19	$TRAd\theta_{48}$
20	$TRAdP_{48}$
21	$TRAd\theta_{MX}$
22	$TRAdP_{MX}$
27	θ_{e850}
28	T_{ADV850}

Figure E.1: Biplot based on varimax rotation of PMI-data points only: Third (second) new component from varimax rotation (cf. Sec: 2.4) in horizontal (vertical) direction including the explained variance along the axes. The grey vectors represent the coefficients for each parameter of C3 and C2. They show in which direction each parameter varies within the events in this projection. The points represent the scores of the events in the rotated component space, where the colors correspond to the maximum bergeron value of each case. The histograms at the left and bottom show the distributions of the points by color. The red lines mark the class boarders and the red numbers label them 1-5.

The biplot in Fig: E.1, based on 1691 PMI-data points, is very similar to the biplot in Fig: 4.10, based on 8455 data points. Considering the variation in the conditions over time (PMI−12/PMI/PMI+12) observed in the case studies (cf. Chap: 3), the similarity of these two biplots is striking. All 29 parameter vectors point into essentially the same direction with the maximum shift being only a few degrees. Additionally the length of the parameters differs by less than 1%. Therefore the horizontal axis can again be summarized as representing “low- to mid-level baroclinicity”, and the vertical axis can be summarized as representing “upper-level forcing and tropospheric instability”. This means that the 5 classes in Fig: E.1 differ based on distinct physical characteristics of the troposphere at PMI.
The histograms along the horizontal and vertical axis of Fig: E.1 indicate that the distribution of the bergeron values within the biplot has not changed significantly when compared to the biplot in Fig: 4.10. Thus the horizontal gradient of increasing bergeron values which was described for Fig: 4.10, is also represented in Fig: E.1. The ETCs which are categorized into classes 1 and 3 at PMI, generally intensify less than those which are categorized into classes 2 and 4.
Finally, based on this analysis it is expected that if the full set of composites are produced from the classification based on Fig: E.1 the interpretation will be very similar to that discussed in Chap:

5.
In summary, we conclude that the results and the classification found in this thesis are statistically robust. In retrospect, one might however wonder whether the analysis exactly at the PMIs would be preferable to the one based on the 5 time instances used in the present version. For instance, at its present state the classification of a single event might be difficult, because the 5 different time instances associated with a single cyclone can potentially be attributed to different classes. However, we expect only minor changes in the physical interpretation of the results, as motivated by the sensitivity experiment described in this appendix.

Nomenclature

Acronyms and Abbreviations

CCP	Cyclone Core Pressure (used to locate cyclone centre)
CIR	Cyclone Intensification Region
ETC	Extratropical Cyclones
PCA	Principal Component Analysis
PMI	Point Maximum Intensification
PV	Potential Vorticity
SLP	Sea Level Pressure
SST	Sea Surface Temperature
θ	Potential Temperature
θ_e	Potential Equivalent Temperature
TME	Tropical Moisture Exports

Bibliography

Abdi, H. (2003). "Facotr Rotations in Factor Analyses". In: *Encyclopedia for Research Methods for the Social Sciences. Sage: Thousand Oaks, CA*, pp. 792–795.

Ahmadi-Givi, F., G. Graig, and R. Plant (2004). "The dynamics of a midlatitude cyclone with very strong latent-heat release". In: *Q. J. R. Meteorol. Soc.* 130, pp. 295–323.

Baehr, C. et al. (1999). "Dynamical characterization of the FASTEX cyclogenesis cases". In: *Q. J. R. Meteorol. Soc.* 125.561, pp. 3469–3494.

Bishop, C. H. and A. J. Thrope (1994). "Frontal wave stability during moist deformation frontogenesis. Part ll: The suppression of nonlinear wave development." In: *J. Atmos. Sci.* 51, pp. 874–888.

Bjerknes, J. and H. Solberg (1922). *Life cycle of cyclones and the polar front theory of atmospheric circulation*. Grondahl.

Bracegirdle, T. J. and E. W. Kolstad (2010). "Climatology and variability of Southern Hemisphere marine cold air outbreaks". In: *Tellus A* 62.2, pp. 202–208.

Danard, Maurice B (1963). *On the influence of released latent heat on cyclone development*. Tech. rep. DTIC Document.

Davis, C. A. and K. A. Emanuel (1991). "Potential Vorticity Diagnostics of Cyclogenesis". In: *Mon. Wea. Rev.* 119, pp. 1929–1953.

Devenson, A. C. L., K. A. Brownin, and T.D. Hewson (2002). "A classification of FASTEX cyclones using a height-attributable quasi-geostrophic vertical-motion diagnostic". In: *Q. J. R. Meteorol. Soc.* 128.doi: 10.1256/00359000260498806, pp. 93–117.

Dixon, M., A. Thrope, and K. Browning (2003). "Layer-wise attribution of vertical motion and the influence of potential-vorticity anomalies on synoptic development". In: *Q. J. R. Meteorol. Soc.* 129, pp. 1761–1778.

Eady, E.T. (1949). "Long Waves and Cyclone Waves". In: *Tellus* 1.3, pp. 33–52.

Fink, A. H. et al. (2012). "Diagnosing the influence of diabatic processes on the explosive deepening of extratropical cyclones". In: *Geophys. Res. Let.* 39, L07803.doi: 10.1029/2012GL051025.

Gabriel, K. R. (1971). "The biplot graphic display of matrices with application to principal component analysis". In: *Biometrika* 58, pp. 453–467.

Gilet, J. B., M. Plu, and G. Rivière (2009). "Nonlinear Baroclinic Dynamics of Surface Cyclones Crossing a Zonal Jet". In: *J. Atmos. Sci.* 66, pp. 3021–3041.

Graf, M. A. (2014). "Objektive Klassifikation von Zyklogenese in den Aussertropen". PhD thesis. ETH Zürich.

Graf, M. A., H. Wernli, and M. Sprenger (2016). "Objective classification of extratropical cyclogegesis". In: *Q. J. R. Meteorol. Soc.* [in preparation].

Gray, S. L. and H. F. Dacre (2006). "Classifying dynamical forcing mechanisms using a height-attributable climatology". In: *Q. J. R. Meteorol. Soc.* 132, pp. 1119–1137.

Gulev, S. K., O. Zolina, and S. Grigoriev (2001). "Extratropical cyclone variability in the Northern Hemisphere winter from the NCEP/NCAR reanalysis data". In: *Climate Dynamics* 17.10, pp. 795–809.

Holton, J. R. (1979). *An Introduction to Dynamic Meteorology*. Academic Press.

Hoskins, B. J., M. E. Mc Intyre, and A. W. Robertson (1985). "On the use and significance of isentropic potential vorticity maps". In: *Q. J. R. Meteorol. Soc.* 111.470, pp. 877–946.

Hotelling, H. (1933). “Analysis of a complex of statistical variables into principal components”. In: *J. Educ. Psychol.* 24, p. 417.

Huo, Z., D. Zhang, and J. R. Gyakum (1999). “Interaction of Potential Vorticity Anomalies in Extratropical Cyclogenesis. Part l: Static Piecewise Inversion”. In: *Mon. Wea. Rev.* 127, pp. 2546–2561.

Jolliffe, I. T. (2002). *Principal component analysis*. Springer, p. 488.

Knippertz, P. and H. Wernli (2010). “A Lagrangian Climatology of Tropical Moisture Exports to the Northern Hemispheric Extratropics”. In: *J. Climate* 23.doi: 10.1175/2009JCLI3333.1, pp. 987–1003.

Lakcmann, G. (2012). *Midlatitude Synoptic Meteorology: Dynamics Analysis and Forecasting*. Reprinted with corrections August 2012. American Meteorological Society.

Liberato, M. L. R. et al. (2011). “Klaus - and exceptional winterstorm over northern Iberia and southern France”. In: *Weather* 66.12, pp. 330–334.

Liberato, M. L. R. et al. (2013). “Explosive development of winter storm Xynthia over the subtropical North Atlantic Ocean”. In: *Nat. Hazards Earth Syst. Sci.* 13, pp. 2239–2251.

Ludwig, P. et al. (2014). “The role of anomalous SST and surface fluxes over the southeastern North Atlantic in the explosive development of windstorm Xynthia”. In: *Q. J. R. Meteorol. Soc.* 140, pp. 1729–1741.

N.N. (2000). *Windstorms Lothar and Martin*. [Menlo Park, CA]: Risk Management Solutions.

Pearson, K. (1901). “On lines and planes of closest fit to systems of points in space”. In: *The London, Edinburgh, and Dublin Philosophical Magazine and journal of Science* 2.11, pp. 559–572.

Petterssen, S. (1936). “Contribution to the theory of frontogenesis”. In: *Geophys. Publ.* 11, pp. 1–27.

Petterssen, S. and S. J. Smebye (1971). “On the development of extratropical cyclones”. In: *Q. J. R. Meteorol. Soc.* 97.doi: 10.1002/qj.49709741407, pp. 457–482.

Pfahl, S., P. O’Gorman, and M. Singh (2015). “Extratropical cyclones in idealized simulations of changed climates”. In: *J. Climate* doi: 10.1175/JCLI-D-14-00816.1, in press.

Powell, V. and L. Lehe (14.03.2016). *Principal Component Analysis: Explained Visually*. URL: `http://setosa.io/ev/principal-component-analysis/`.

Roebber, P. J. (1984). “Statistical Analysis and Updated Climatology of Explosive Cyclones”. In: *Mon. Wea. Rev.* 112, pp. 1577–1589.

Sanders, F. and J. R. Gyakum (1980). “Synoptic-dynamic Climatology of the ”Bomb””. In: *Mon. Wea. Rev.* 108, pp. 1589–1606.

Schultz, D. M., D. Keyser, and L. F. Bosart (1998). “The Effect of Large-Scale Flow on Low-Level Frontal Structure and Evolution in Midlatitude Cyclones”. In: *Mon. Wea. Rev.* 126.7, pp. 1767–1791.

Shapiro, M. A. and D. A. Keyser (1990). “Fronts, jet streams, and the tropopause”. In: *Extratropical Cyclones: The Erik Palmen Memorial Volume*, pp. 167–191.

Trenberth, Kevin E (1978). “On the interpretation of the diagnostic quasi-geostrophic omega equation”. In: *Monthly Weather Review* 106.1, pp. 131–137.

Uccellini, L. W. and D. R. Johnson (1979). “The coupling of Upper and Lower Tropospheric Jet Streaks and Implications for the Development of Severe Convective Storms”. In: *Mon. Wea. Rev.* 107, pp. 682–703.

Ulbrich, U. et al. (2001). “Three extreme storms over Europe in December 1999”. In: *Weather* 56, pp. 70–80.

Wernli, H. and C. Schwierz (2006). “Surface cyclones in the ERA-40 data set (1958-2001). Part l: Novel identification method and global climatology”. In: *J. Atmos. Sci.* 63, pp. 2486–2507.

University of Zurich[UZH]
Department of Geography GIUZ

Eidgenössische Technische Hochschule Zürich
Swiss Federal Institute of Technology Zurich
Institute of Atmospheric and Climate Science IAC

Title of work:

Objective Classification of Extratropical Cyclones During Their Phase of Maximum Intensification

Thesis type and date:

Master Thesis, 22 April 2016

Supervision:

Prof. Dr. Heini Wernli
Dr. Michael Sprenger
Dominik Büeler
Institute of Atmospheric and Climate Science
Universitätstrasse 16, 8092 Zürich

Responsible Faculty Member

Prof. Dr. Jan Seibert

Student:

Name: Luise Fischer
E-mail: lufisc@geo.uzh.ch
Student Id.: 09-720-632

Personal declaration:

I, Luise Fischer, hereby declare that the submitted thesis is the result of my own, independent work. All external sources are explicitly acknowledged in the thesis.

Zurich, 21. 4. 2016: _____